UNIVERSITY OF ILLINOIS
URBANA

PROGRESS REPORT NO. 81-1

RESEARCH IN AERONOMY

OCTOBER 1, 1980 - MARCH 31, 1981

Edited by
Delva Edwards

Supported by
National Aeronautics and Space Administration
National Oceanic and Atmospheric Administration
National Science Foundation

Aeronomy Laboratory
Department of Electrical Engineering
University of Illinois
Urbana, Illinois

PROGRESS REPORT

NO. 81-1

RESEARCH IN AERONOMY

October 1, 1980 - March 31, 1981

Edited by

Belva Edwards

Supported by
National Aeronautics and
Space Administration
National Science Foundation

Aeronomy Laboratory
Department of Electrical Engineering
University of Illinois
Urbana, Illinois

FOREWORD

The Aeronomy Laboratory is organized into working groups according to the various areas of research being carried out. This arrangement is intended to encourage better communication among graduate students and staff members, and to stimulate ideas for new lines of scientific inquiry. Individuals may participate in as many groups as their interests dictate.

This Progress Report for the period October 1, 1980 - March 31, 1981 contains summaries of work performed by each working group. These summaries have been written as a part of the groups' activities.

On the following page the various groups and members are listed in the order that their reports appear in this volume. Support for the research of each group is given in parentheses following the name.

AERONOMY LABORATORY WORKING GROUPS

October 1, 1980 - March 31, 1981

IONOSPHERIC THEORY
(NSF: ATM 79-09982;
NASA: NGR 14-005-181; NSG 5213)

S. K. Avery (Chairman)
S. A. Bowhill
K. P. Gibbs
G. A. Jones
O. Røyrvik
C. F. Sechrist, Jr.
L. G. Smith

METEOR RADAR
(NSF: ATM 79-09982;
NASA: NGR 14-005-181)

S. K. Avery (Chairman)
S. A. Bowhill
J. D. Gooch
S. W. Henson
J. Peterson
O. Røyrvik
D. Tetenbaum

ROCKET EXPERIMENTS
(NASA: NGR 14-005-181)

L. G. Smith (Chairman)
S. A. Bowhill
F. M. Braswell
L. Dean
R. W. Fillinger, Jr.
L. J. Johnson
M. K. McInereny

COHERENT AND INCOHERENT SCATTER
(NSF: ATM 78-15224; ATM 78-21765;
ATM 80-02049
NASA: NGR 14-005-181; NSG 7506)

O. Røyrvik (Chairman)
S. A. Bowhill
R. O. Colbert
P. M. Dolas
K. P. Gibbs
J. D. Gooch
S. W. Henson
J. Loane
G. Metze
D. R. Tanner
F. Zendt

PARTIAL REFLECTION
(NASA: NGR 14-005-181)

R. M. Weiland (Chairman)
S. A. Bowhill
O. Røyrvik
R. Ruggerio

LASER RADAR
(NSF: ATM 78-12308; ATM 79-20726;
NASA: NGR 14-005-181)

C. F. Sechrist, Jr. (Chairman)
D. J. Burlet
C. S. Gardner
H. Merkelo (Quantum Electronic Laboratory)
R. Nilssen
J. D. Shelton
F. M. Vogel

TABLE OF CONTENTS

1. IONOSPHERIC THEORY

This project involves theoretical and experimental studies of the effects of atmospheric dynamics on the ionosphere and neutral chemistry of the stratosphere, mesosphere and thermosphere. The research is supported in part by the National Aeronautics and Space Administration under grants 14-005-181 and NSG 5213, and in part by the National Science Foundation under grant ATM 79-09982.

1.1 *Planetary-Wave Dynamics*

An investigation is continuing into the effects of vertically propagating planetary waves on NO densities in the 70 to 120 km altitude region. A time-dependent model has been developed to calculate the transport of NO due to planetary-wave-induced winds. These transports seem to be sensitive to the planetary-wave forcing used at the lower boundary, as well as to the structure of the zonal mean basic state.

The results shown are from a calculation of steady-state NO transport by stationary planetary waves. Fluxes and transports of NO are calculated for the months of January and February, 1974, using a separate basic state and boundary forcing for each month. The boundary forcings were obtained by performing a spatial Fourier decomposition on .4 mb NMC geopotential height data for the weeks of January 2 through February 27, 1974. The zonal mean wind profile for the months of January and February were also inferred from NMC data. The month of February was interesting in that a major stratospheric warming occurred near the end of that month. The large planetary wave amplitude and reduction in zonal mean wind velocities due to this warming are reflected in the February average boundary forcing and zonal mean state.

Figure 1.1 shows the results of a calculation of zonally averaged horizontal ($\overline{v'[NO]'}$) and vertical ($\overline{w'[NO]'}$) NO flux at 105 km. An upward arrow represents a northward upward motion. These fluxes are due to planetary wave number 1 for the month of January and February. It can be seen that while the horizontal flux is to the south in January, the direction reverses and the flow is to the north in February. The vertical flux also undergoes this same reversal, with upward flux in January and downward flux in February.

By calculating vertical and horizontal transports, the effect of these fluxes on the zonally averaged NO concentration at 105 km can be determined. The zonally averaged continuity equation for NO in the absence of a mean meridional flow can be expressed as:

$$\frac{\partial[\overline{NO}]}{\partial t} - \frac{1}{a\cos\theta}\frac{\partial}{\partial\theta}\left[\overline{v'[NO]'}\cos\theta\right] - \left(\frac{\partial}{\partial z} - 1\right)\overline{w'[NO]'}$$

The first and second terms on the right hand side represent the change in the zonally averaged nitric oxide concentration due to north-south and vertical transport of nitric oxide by planetary waves.

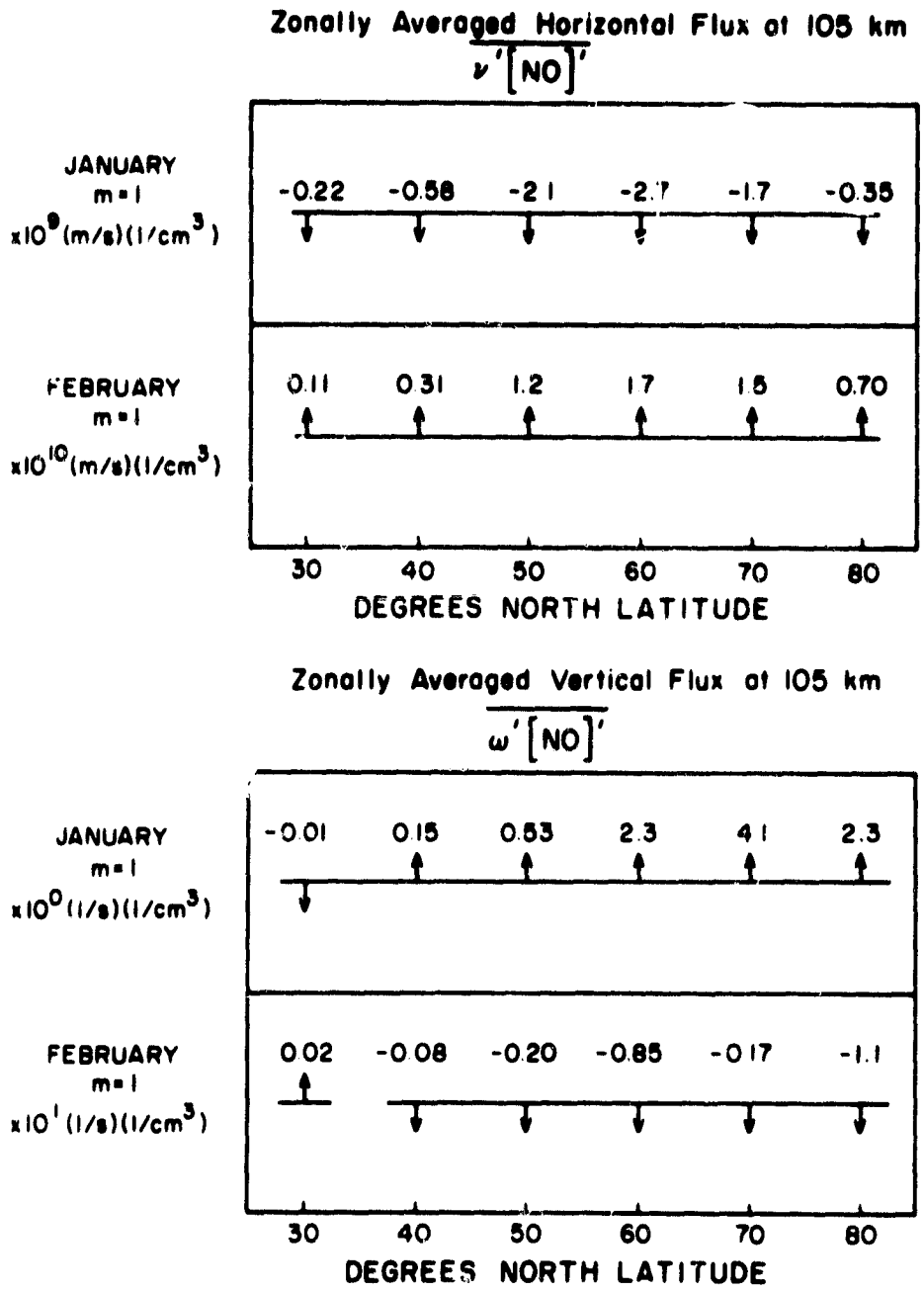

Figure 1.1 Zonally averaged horizontal and vertical NO flux for wave number 1 at 105 km.

Figure 1.2 shows the change in $[\overline{NO}]$ due to north-south transport by wave number 1 for the months of January and February. In January, the concentration is decreasing in the polar region and increasing in midlatitudes, due to a southward flux of NO. In February, however, the situation is reversed, with the zonally averaged concentration increasing in the polar regions and decreasing in midlatitudes due to a northward flux of NO.

Figure 1.3 shows the change in $\overline{NO}$ due to vertical transport by wave number 1. Note that the changes in Figure 1.3 are an order of magnitude smaller than those in Figure 1.2. The reversal from month to month seen in Figure 1.2 is also apparent in Figure 1.3. In January, the concentration of NO at 105 km is increasing due to a flux of nitric oxide from below. In February, however, the concentration at 105 is decreasing, due to a flux of NO downward out of the region.

A more detailed investigation into the area of NO transport is currently underway. A time-dependent model will be used to calculate the transport of NO by both planetary waves and the mean meridional circulation. The effects of changes in zonally averaged production and loss rates of NO will also be considered.

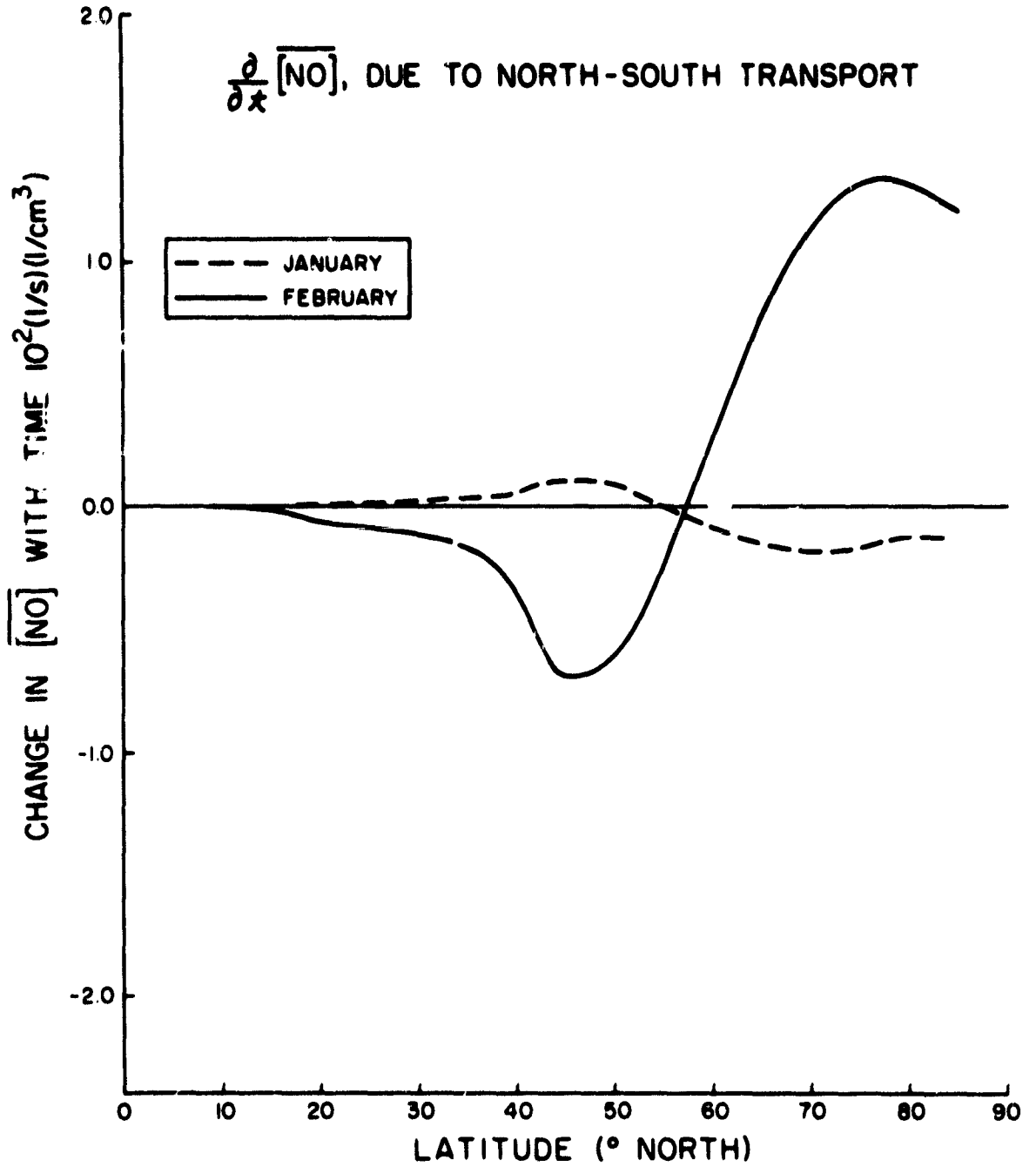

Figure 1.2 Change in $\overline{NO}$ due to meridional transport by wave number 1.

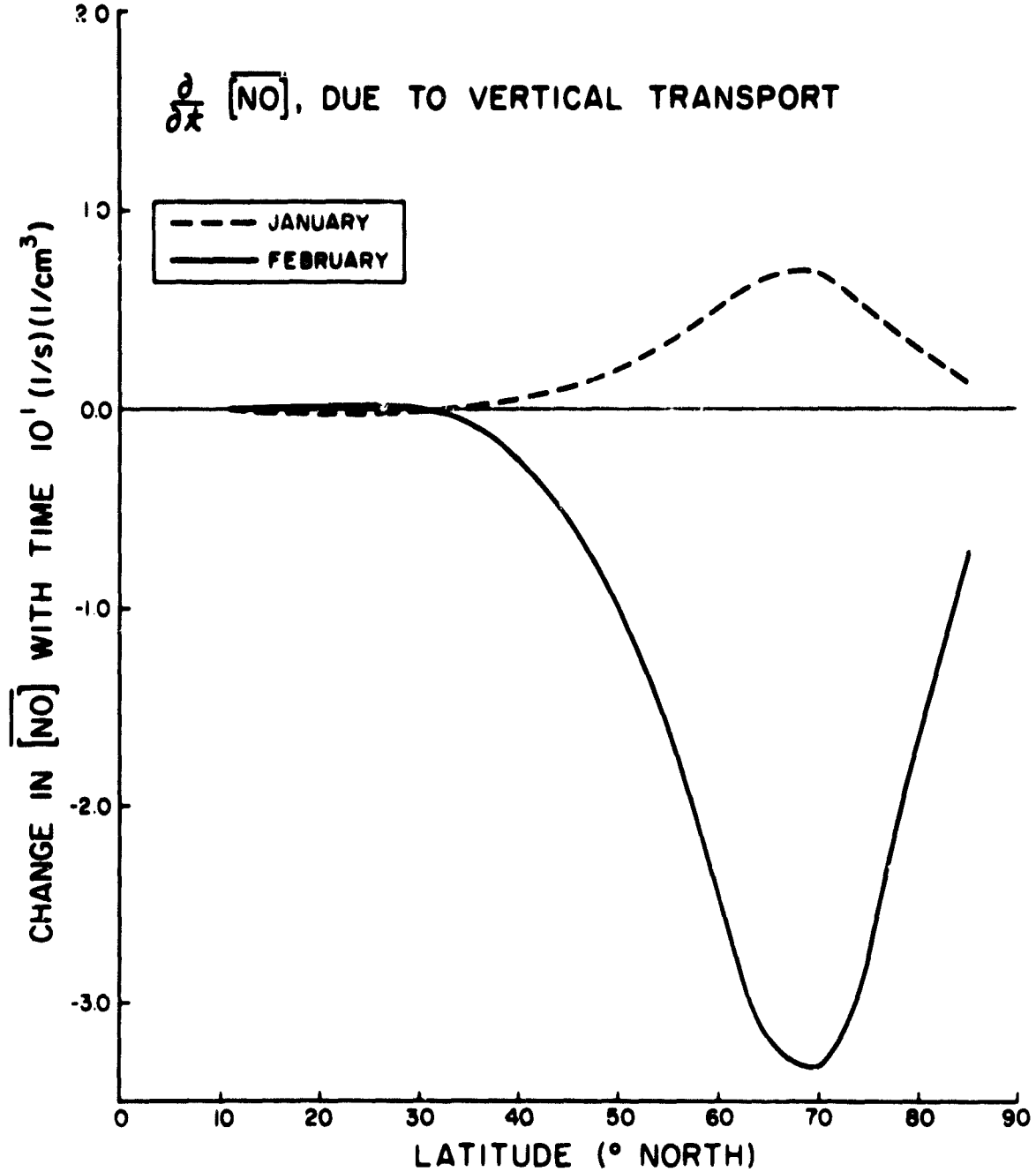

Figure 1.3 Change in $\overline{NO}$ due to vertical transport by wave number 1.

D2

2. ROCKET EXPERIMENTS

The tasks of this group, under the direction of L. G. Smith, relate to the definition of the scientific objectives of the Aeronomy Laboratory's rocket program; to the development and fabrication of instrumentation; to the scheduling and launch operations associated with individual and coordinated rocket experiments. This research is supported by the National Aeronautics and Space Administration under Grant NGR 14-005-181.

2.1 *Introduction*

The Aeronomy Laboratory participated in the Energy Budget Campaign with three payloads (designated E11) on Taurus Orion rockets. The rockets were launched, as part of two salvoes, on 16 and 30 November 1980, at ESRANGE near Kiruna, Sweden. The launch times and apogee altitudes are indicated in Table 2.1. The three payloads were identical except for the mass spectrometer, provided by the University of Bern, which measured positive ions in two flights and negative ions in the other, as indicated in Table 2.1 by P and N, respectively.

The principal objective of these flights is the study of the ionization and the ionizing sources (energetic particles) during periods of auroral activity. This is accomplished by measuring the concentration and temperature of the ionospheric (thermal) electrons, the ion composition, and the flux of energetic particles (discriminated by type of particle, spectrum and pitch-angle distribution). The payloads also included an experiment, provided by the University of Sussex, to study the high-speed fluctuations (bunching) in the energetic particle flux. We now give a general description of the payloads and the supporting systems followed by an account of the University of Illinois experiments and some preliminary results.

The Energy Budget Campaign included other rocket launches, using the range at Andoya, Norway as well as that at ESRANGE; ground-based experiments; and some balloon-borne experiments. Also one pass of satellite S78-1 occurred within 3 minutes of the launch of Taurus Orion 33.009 on 30 November 1980. This will allow some interesting comparisons of energetic particle data from the rocket and the satellite.

2.2 *General Description*

The general arrangement of the Taurus Orion payloads is indicated in Figure 2.1. The diameter of the instrumentation section is 30 cm. At the front is an ejectable nose cone, protecting the input section of the mass spectrometer. Ejection takes place at an altitude of T + 52 s (57 km, nominal altitude) and the cap of the mass spectrometer is ejected 2 s later (at 60 km).

Doors in the rear experiment section are also ejected at T + 52 s (57 km) and booms deployed at T + 60 s (67 km). The booms carry the electrodes of the probe experiment and the forward-looking energetic-particle detectors. The spin rate at boom deployment (and for the scientifically significant

Table 2.1

Taurus Orion (E11 payloads)

ROCKET	M.S.*	LAUNCH (UT)		SALVO	APOGEE (km)
33.010	P	03:49:40	16 November 1980	B	177.3
33.011	N	04:15:00	16 November 1980	B	179.2
33.009	P	23:44:30	30 November 1980	A-2	171.7

*Mass spectrometer: P, positive ion; N, negative ion.

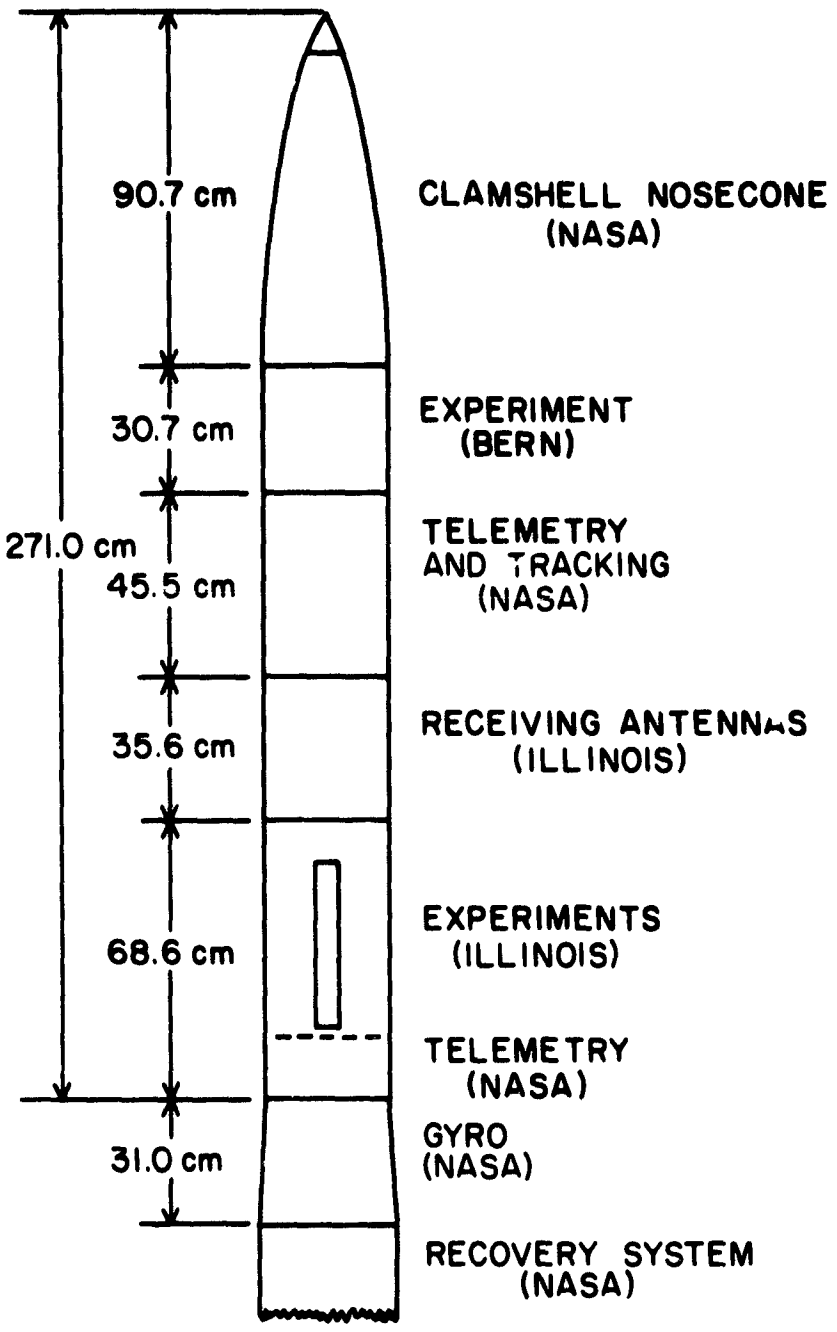

Figure 2.1 The configuration of the Taurus Orion (E11) payloads showing the location of the instrumentation.

part of the flight) was specified to be 5.5 rps. The actual values (at apogee) for the three payloads range from 5.86 and 5.98 rps. The rockets showed very little precessional motion.

The payload includes a transition frustrum to adapt the 30-cm-diameter instrumentation section to the 36-cm-diameter recovery system. The second-stage rocket (Orion) is also 36-cm diameter. The total length of the payload, including the transition frustrum and the recovery system, is 349 cm; the total weight is 181 kg. The nominal (predicted) apogee was 171 km, which was accomplished, and, for two flights, slightly exceeded (see Table 2.1).

The payload includes two independent S-band (about 2.3 GHz) FM/FM telemetry systems. The forward system supports the mass spectrometer experiment, one tracking system (TRADAT) and various monitors (battery voltage, etc). The rear system works with the Illinois/Sussex experiments, the gyroscope and a commutator which carries monitor signals (recovery system, etc).

The three-axis gyroscope is located inside the transition frustrum. The yaw, pitch and roll signals are transmitted on channels 5, 6 and 7, respectively and the commutator on channel 8. The output of a transverse magnetometer (to measure spin rate) is carried on channel 9. The remaining channels (10 to 20, and 1) of the rear telemetry system carry signals from the experiments described below.

Two tracking systems are used. Radar tracking by an MPS-36 is aided by a transponder located in the forward instrumentation section. The primary tracking system (TRADAT) uses a PCM signal transmitted (at 500 MHz) to a receiver in the forward section of the payload. The information (3.9 kHz bit rate) is telemetered to the receiving station on channel 18 of the forward system. Range is obtained from the round-trip time delay. The azimuth and elevation angles are obtained from the S-band receiving antenna position.

The recovery system severs the payload from the rocket motor at T + 318 s (nominally 115 km, on descent). A second severance occurs at a nominal altitude of 6 km, releasing the main parachute. The predicted impact occurs 17.5 minutes after launch.

The arrangement of the rear experiment section containing the experiments of the Universities of Illinois and Sussex is shown in detail in Figure 2.2. The booms are folded with the ejectable doors covering them. The booms are restrained by a cable which is cut after the doors have been ejected. The spin of the rocket causes the booms to deploy. At full extension the center-to-center distance of the probe electrodes is 179 cm.

2.3 *Measurement of Thermal Electrons*

2.3.1 *Introduction.* The probe experiment is used to measure the variation (fine structure) in electron concentration, to measure electron temperature and in the measurement of vehicle potential. The propagation experiment is used to obtain the electron concentration and the electron collision frequency. Both experiments are well established in theory and in instrumentation.

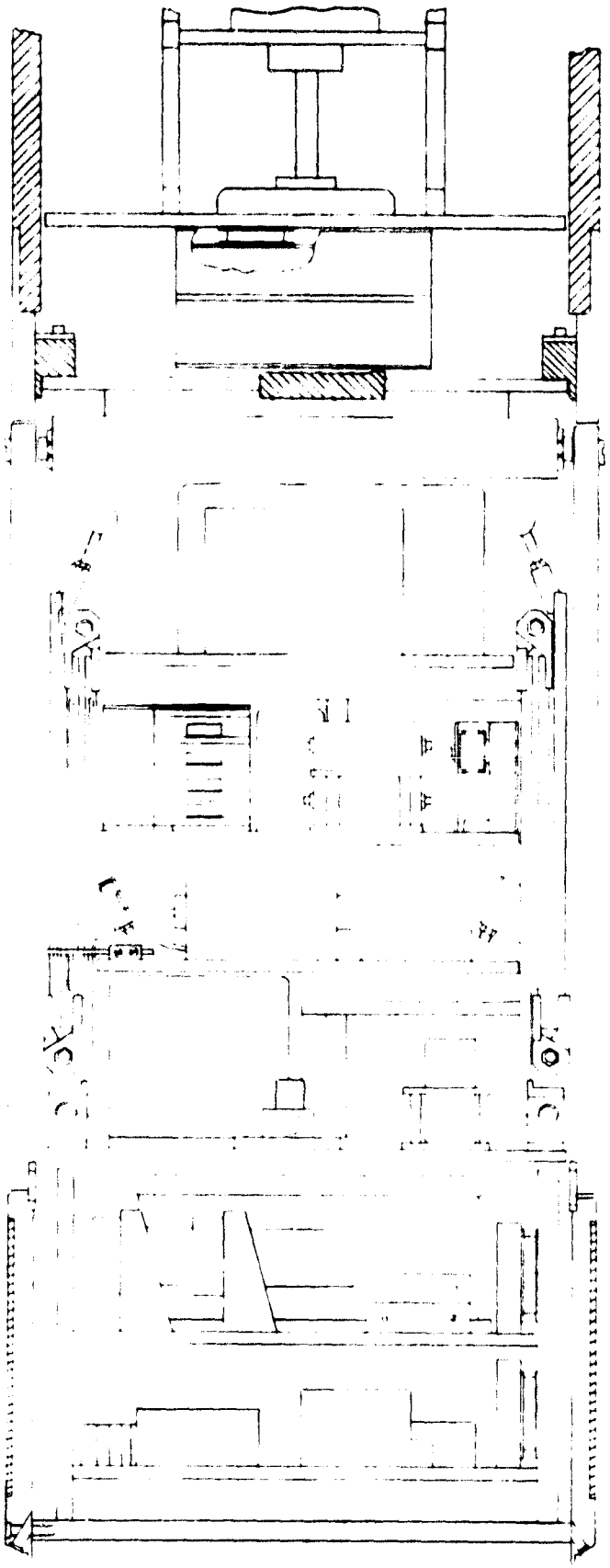

RECEIVING ANTENNAS

RECEIVERS

DOOR RELEASE MECHANISM

BOOM PROBES

PARTICLE BUNCHING EXPERIMENT

PARTICLE DETECTORS
PULSE-HEIGHT ANALYZER
COUNTING CIRCUITS

PARTICLE DETECTORS
MAGNETOMETER

PROBE ELECTRONICS
MICROPROCESSOR

BATTERY
TIMERS
CONVERTERS

FM/FM TELEMETRY
COMMUTATOR
CONTROL RELAYS

Figure 2.2 The rear experiment section of the payloads of the Taurus Orion rockets.

2.3.2 *DC/Langmuir probe experiment.* The electrodes used in these payloads are 0.95 cm diameter and are coated with Aquadag (colliodal graphite) to give a surface of uniform contact potential. The two electrodes are connected in parallel to the electronic circuits: this minimizes the spin modulation which appears in the probe signal. The voltage applied to the electrodes is fixed at 4V except that, at intervals of 2 s it is swept from -1.35V to 4V with a duration of 0.3 s.

The probe current at fixed voltage is measured using a logarithmic electrometer and transmitted on channel 20. During the sweep period the rate-of-change of probe current is measured on the same electrometer. This allows the electron temperature to be obtained directly [*Smith et al.*, 1968; *Zimmerman and Smith*, 1980]. This mode also allows vehicle potential to be obtained.

The electrometer output is amplified during the period of fixed voltage, and transmitted on channel 18. The amplifier has a frequency range of 90 to 2000 Hz [*Klaus and Smith*, 1978]. This is the fine-structure experiment.

2.3.3 *Radiowave propagation experiment.* The radiowave propagation experiments used with rockets are based on the techniques of dispersive Doppler and of differential absorption. The most successful techniques use the two characteristic modes of the wave which, in the ionosphere, have different refractive indices and absorption coefficients. In this context dispersive Doppler and Faraday rotation are identical techniques.

For the Energy Budget Campaign we chose to use a simpler technique than we had previously used. This was done because of the availability of transmitters and antennas at ESRANGE. The type of experiment has been described, for example, by *Prince and Williams* [1976] and *Jacobsen and Friedrich* [1979].

Our payloads each contain two independent propagation experiments: one operates at 3.883 MHz and the other at 7.835 MHz. The modulation outputs of the two receivers are transmitted on channels 14 and 15, and the AGC voltage on channels 10 and 11.

The dispersive Doppler and differential absorption techniques end when the extraordinary mode has been totally absorbed. In the three flights useful data are obtained between altitudes of 70 and 95 km. At greater altitudes some data may be recovered from the AGC signals since this can be related to absorption of the ordinary mode.

2.3.4 *Probe data analysis.* A preliminary analysis has been done on the probe data from the three flights. Before a final analysis can be made, two computer programs used in reducing these data must be rewritten for a CDC Cyber 175. This is due to a change in the computer system used in digitizing the data at NASA (Wallops Flight Center). Also the original programs were written for an IBM machine. The University of Illinois now has a Cyber 175 which can perform the same processing much faster (and cheaper) than the IBM.

Shown in Figures 2.3 and 2.4 are the probe current profiles for the two launches during Salvo B: Taurus Orions 33.010 and 33.011. The altitude is

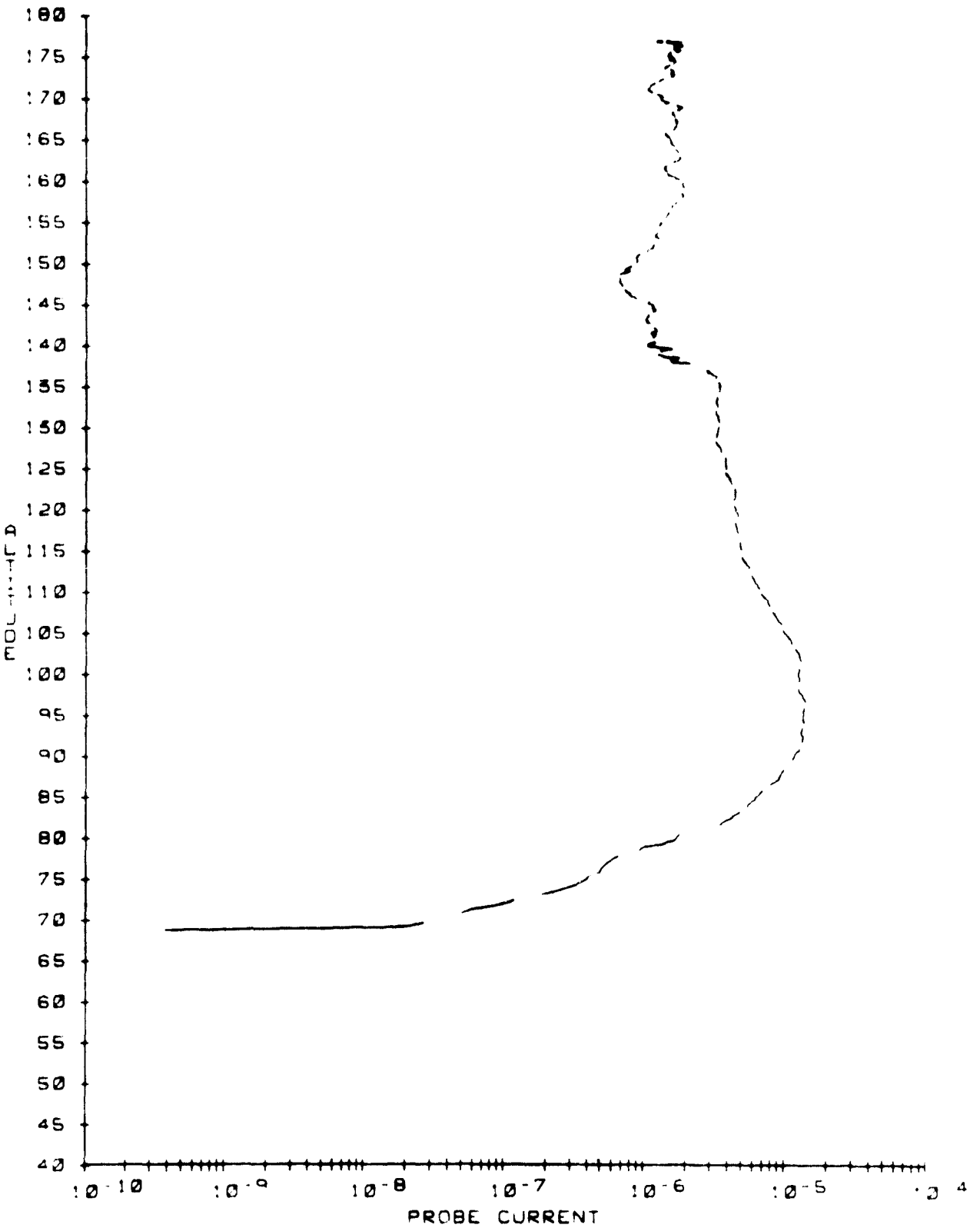

Figure 2.3 Probe current profile of 33.010 launched from ESRANGE 16 November 1980 at 03:49:40 (UT).

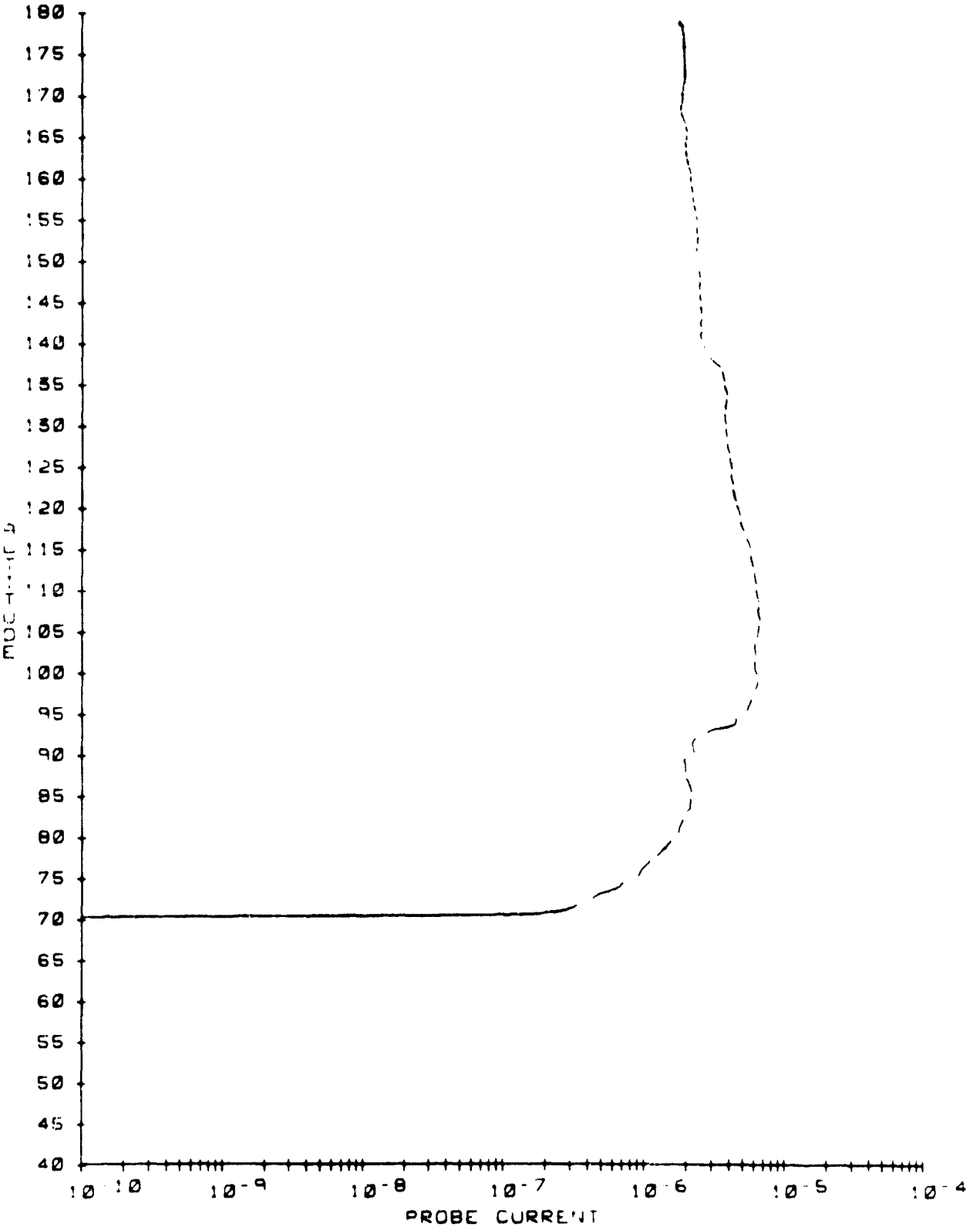

Figure 2.4 Probe current profile of 33.011 launched from ESRANGE 16 November 1980 at 04:15:00 (UT).

in kilometers and the current is in amps. Only the ascent portion of each flight is shown. The interrupted profile occurs because the sweeps (introduced to measure electron temperature and vehicle potential) have been removed.

Very noticeable in Figure 2.4 is the sharp rise in current at 94 km, followed by a sharp decrease at 139 km. It may also be noted that rocket 33.010 (Figure 2.3) also exhibits a sharp decrease in current at 139 km but no sharp rise at the lower altitude.

The probe current profile for the launch in Salvo A-2 is shown in Figure 2.5. Again only the ascent portion is shown and the sweeps have been removed. Again there is a sharp increase in current followed by a sharp decrease. This time at 107 and 125 km, respectively.

2.4 *Energetic Particle Experiment*

2.4.1 *Introduction.* The detectors used in this experiment are silicon surface-barrier devices. Four detectors, Table 2.2, are included in each payload: all have a sensitive area of 50 mm^2, use a reverse bias of about 100V and have a depletion layer thickness of 300 μm.

Two detectors are mounted on the booms (one on each boom; see Figure 2.2) so that, with the booms deployed, the axis of the detector is 25 degrees from the payload spin axis. The geometrical factor (GF) for the forward-looking detectors is 0.45 cm^2ster; the large value was chosen to give a high count rate for the particle bunching experiment. The full width at half maximum (FWHM) is 59 degrees.

The other two detectors are mounted inside the payload behind one of the door openings. These are oriented perpendicular to the spin axis. They have GF = 0.057 cm^2ster and FWHM = 18 degrees. The narrower field of view gives better pitch-angle resolution.

One of each pair of detectors has an increased thickness of aluminum on the front surface The comparison of the flux seen by the pair of detectors allows some discrimination regarding the type of energetic particle (electron, proton, etc). This technique has been described by *Fries et al.* [1979].

The general arrangement of the electronic circuits of this experiment is shown in Figure 2.6. The signal developed in the detector is a very small charge which is proportional to the energy of the particle (excluding the energy lost in traversing the metal layer). This signal is converted to a voltage in the low-noise pre-amplifier which has a capacitor as the feedback element. The pulse is now shaped (and noise is reduced) and further amplified so that a 128 keV particle gives a (negative) 10V-peak pulse. The pulse duration is about 3 μs at this point.

After amplification the pulses are processed in three separate systems. One is the particle-bunching experiment provided by M. P. Gough, University of Sussex. The other two systems are in parallel but are not redundant. The staircase generators indicate particles above a threshold energy at the instant

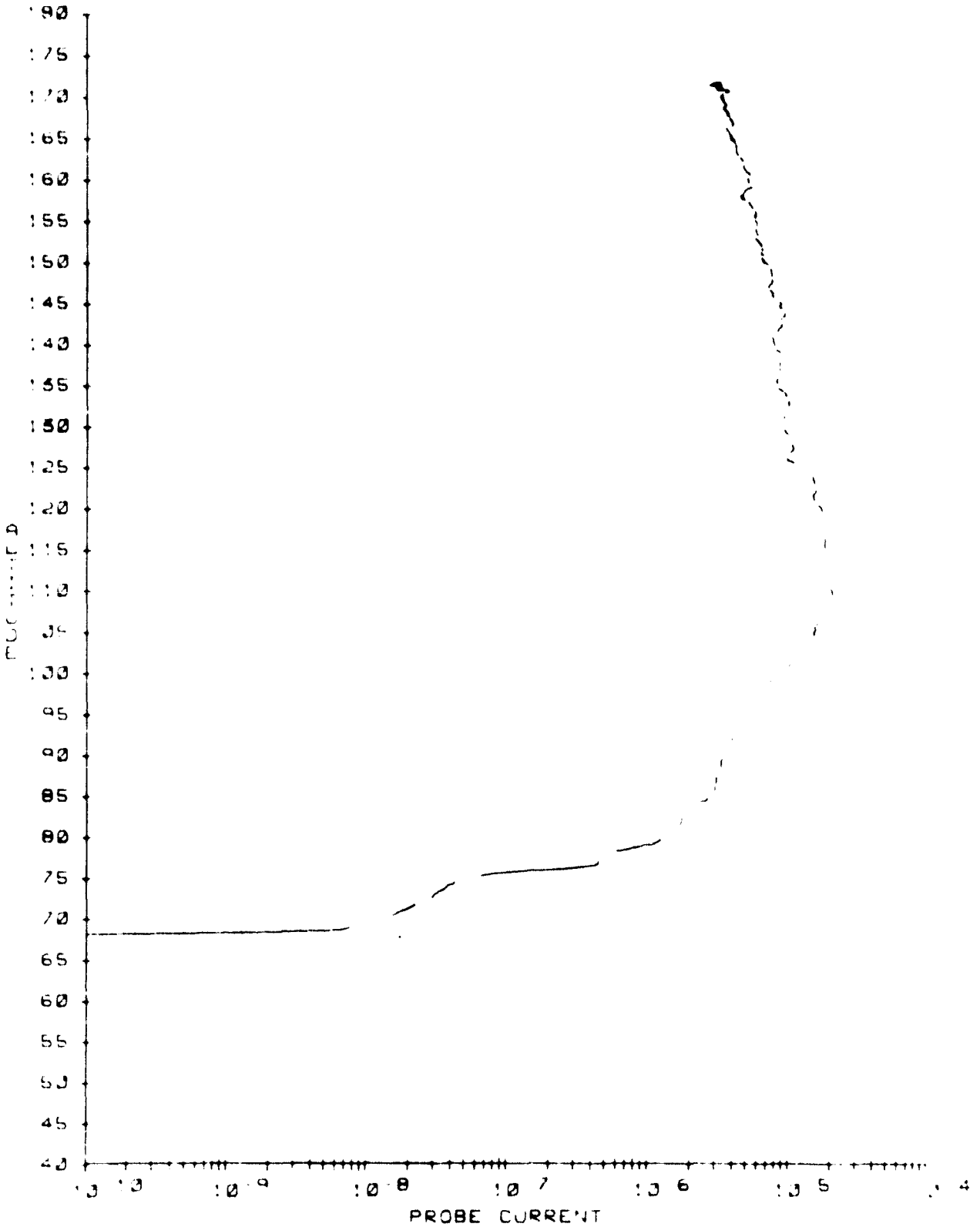

Figure 2.5 Probe current profile of 33.009 launched from ESRANGE 30 November 1980 at 23:44:30 (UT).

Table 2.2

Energetic Particle Detectors

NUMBER	METAL ($\mu g/cm^2$)	ANGLE (deg)	GF ($cm^2 ster$)
1	40 Au + 40 Al	25	0.45
2	40 Au + 150 Al	25	0.45
3	40 Au + 40 Al	90	0.057
4	40 Au + 150 Al	90	0.057

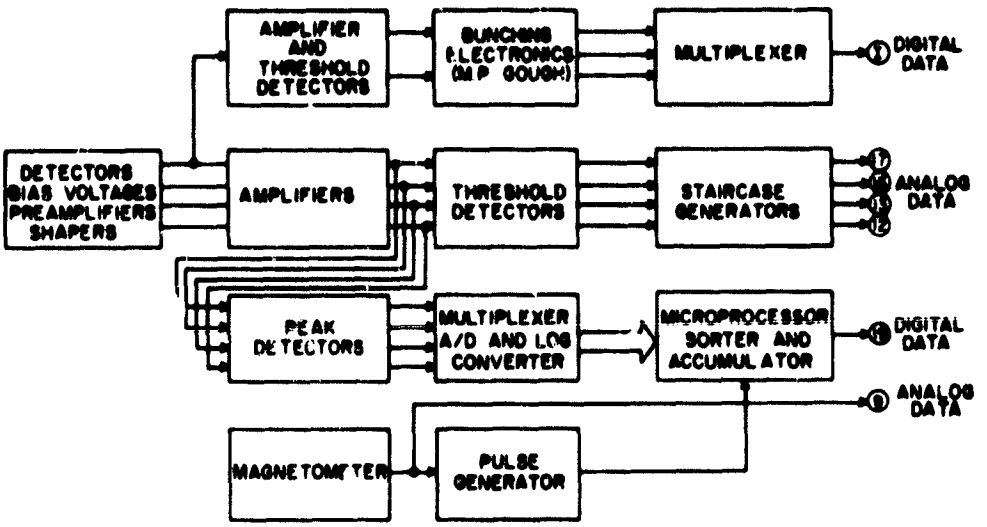

Figure 2.6 The energetic particle experiment.

of occurrence. The microprocessor system, on the other hand, accumulates data over a period of about 5 seconds but sorts the data, before transmission, by energy and pitch angles. Thus the staircase output is useful for studies of pulsations whereas the microprocessor gives the energy spectrum. Both give pitch-angle distributions. The telemetry channels used in this experiment are indicated in Figure 2.6.

The accurate determination of particle flux for the side-looking detectors is difficult: the payload intercepts gyrating particles with pitch angles near 90 degrees [*Voss and Smith*, 1977].

2.4.2 *Staircase system.* The pulses from each amplifier pass to a comparator set for -2V, giving a threshold energy of 25 keV. This is a nominal value, the actual value is established by calibration with a radioactive source. The pulses are lengthened to 50 μs in a one-shot to establish a dead time and limit the maximum counting rate. An 8-bit counter (5 bits are used) and a digital-to-analog converter give the staircase output, one step for each pulse. After 32 counts, which is 5V output, the staircase returns to 0V. Each of the four detectors has a staircase system.

One advantage of this system is the extremely wide range of count rates that can be measured. The upper end of the range is limited only by the information bandwidth of the telemetry channel. Because of the one-shot the maximum count rate that can be transmitted is 2×10^4 s^{-1}. Rates approaching this value must be corrected for the dead time. At this maximum rate the rate for the staircases themselves is less by a factor of 32 i.e. 625 s^{-1}. With the telemetry channels used there is a reduction in amplitude at this maximum rate but no loss of information on count rate. This reduction, and the strong pitch-angle dependence for the side-looking detectors is illustrated in Figure 2.7.

2.4.3 *Microprocessor system.* The Z80 microprocessor is preceded by a pulse-height analyzer. Four peak detectors, Figure 2.6, one for each particle detector, retain the pulse of largest magnitude. The four data channels are sampled sequentially at intervals of 50 μs. Each channel accumulates data for 150 μs. It is then read and, in the remaining 50 μs of the cycle, is cleared. This process is indicated in Figure 2.8(a).

The exponential nature of typical particle energy spectrums make it appropriate to convert from the linear pulse-height measurement to a logarithmic one. This is simply accomplished using an erasable programmable read-only memory (EPROM) in which the inputs (linear data) are the address and the outputs are the log data.

The energy range is divided into 16 bins. The lowest contains only the counts from noise; the highest contains the counts from all energies greater than 128 keV. The remaining bins cover specific ranges of energy on a logarithmic scale.

The energy spectrums obtained in this way are further subdivided by pitch angle. This is accomplished using the spin magnetometer as a reference. The spin period is divided into 32 equal intervals by a counter and the spectrums

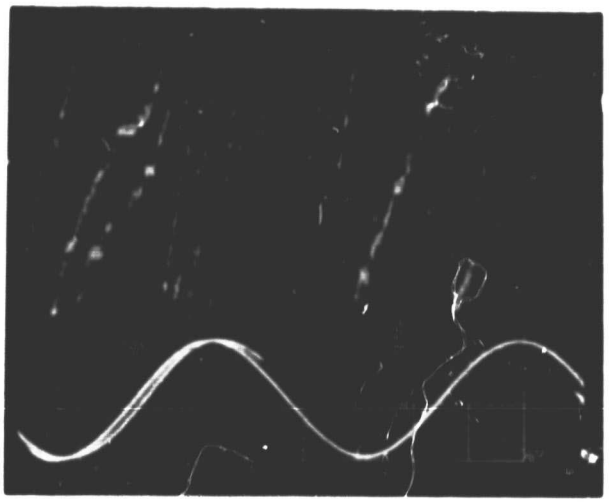

Figure 2.7 The staircase output from a side-looking detector and the magnetometer signal showing strong pitch-angle dependence. The photograph shows a partial overlap of a second scan.

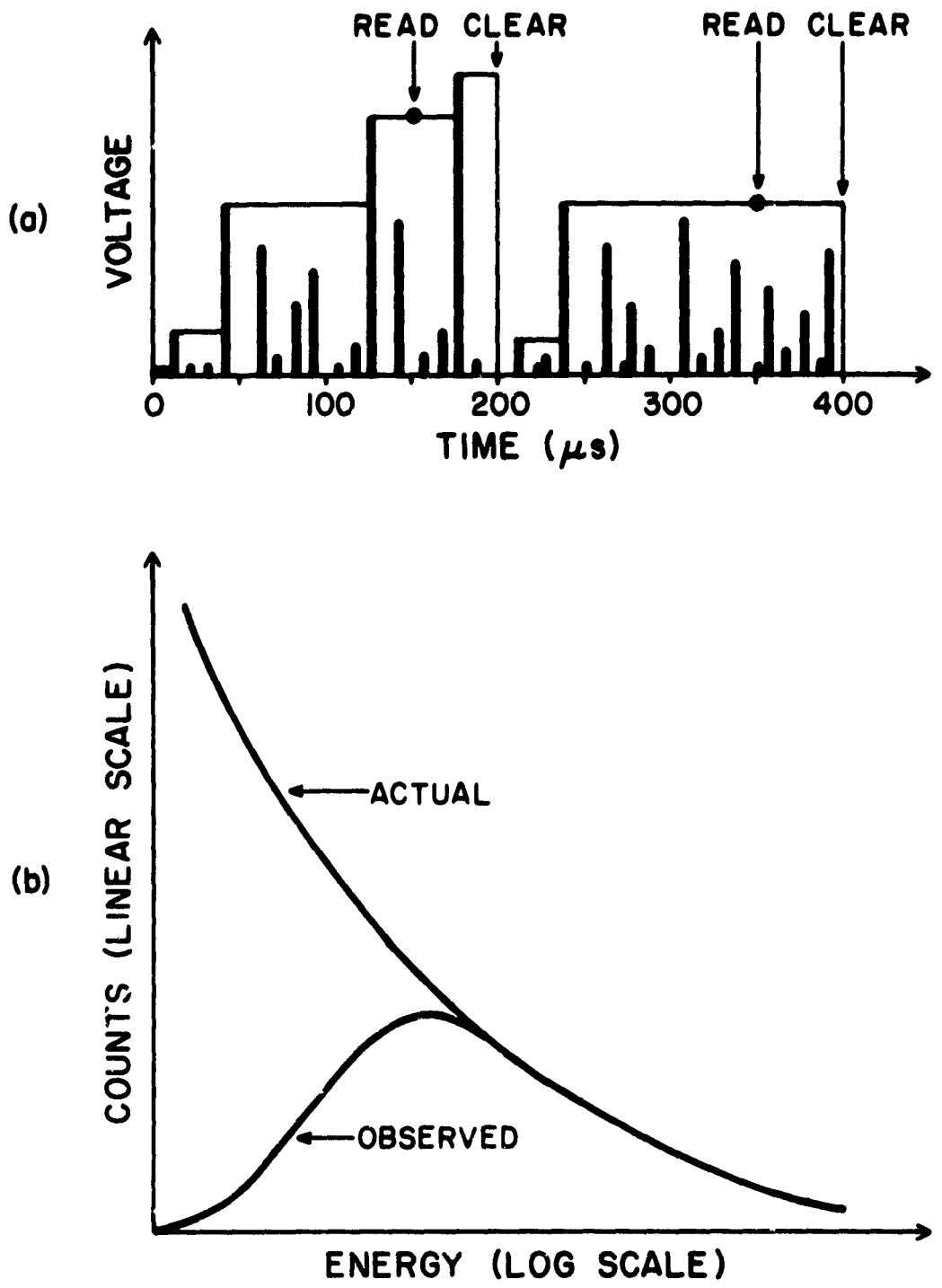

Figure 2.8 Sampling error in the pulse-height analyzer at very high count rates. (a) The peak detector selects the larger pulses. (b) The resulting distortion of the energy spectrum.

accumulated by sector for a total time (about 4.8 s) which is slightly longer than the time needed to transmit the data.

The data are transmitted in serial-digital form. The energy spectrums for the four detectors are transmitted for each sector until all 32 sectors are completed. This system is described in more detail in *Braswell and Smith* [1981].

The flight data from the microprocessor requires special post-processing since it is transmitted as digital information over the FM/FM telemetry system. This is a form of frequency-shift keying (FSK).

Each byte of data was accompanied by stop and start bits so that a standard UART (Universal Asynchronous Receiver/Transmitter), such as the 1013, can decode the serial format off the analog flight tape.

As soon as the UART decodes a byte of data it delivers it as 8 parallel bits as its output port where an LSI/11 microcomputer reads it in and stores the information on floppy disks.

The information on the floppy disks is later transferred to a Cyber 175 disk file for data analysis for FORTRAN programs.

The high count rates encountered in the launches of the Energy Budget Campaign, caused a problem for the pulse-height analyzer. As indicated in Figure 2.8, the smaller pulses are selectively ignored causing the apparent spectrum to be modified. If the pulses are assumed to be randomly occurring then a correction can be made to the data.

Two additional features complicating the analysis of the particle data have been noticed. The first, also a result of high counting rates, is that overflow occurs in the highest energy bin. This is not serious but requires additional effort in the data analysis. The other, apparently unrelated to the high count rate, is that the azimuth reference appears to be displaced by about 60 degrees. Since this effect is also seen in the output of the staircase system (Figure 2.7) it is clearly not attributable to the microprocessor system.

2.5 *Future Plans*

The first post-flight meeting for the Energy Budget Campaign is to be held in Heidelberg, Germany in April 1981.

The analysis of data will continue to be a major effort in the next year. It is hoped to contribute papers to the COSPAR meeting of May/June 1982 in Ottawa. Special sessions related to the Energy Budget Campaign are being organized by Dr. D. Offermann.

Two rocket launches are planned for the summer of 1981. These are Nike Orions 31.014 and 31.015, instrumented to study energetic particle precipitation at middle latitudes and its effect on the nighttime ionosphere. The launches

will take place near midnight from Wallops Island with the magnetic index $K \geq 5$.

The experiments are similar to those used in the Energy Budget Campaign (see above) with the addition of a second probe experiment and a lunar aspect sensor. Both are described in detail in *Durkin and Smith* [1981].

Tentative plans for the more distant future include nighttime launches from White Sands, late in 1982, re-using the Energy Budget Campaign payloads. The main scientific objective will now, however, be the yet unresolved question of the role of metal ions in maintaining the nighttime lower ionosphere.

In the following year (1983) it is hoped to participate in a NASA launch operation at the magnetic equator using the existing site near Lima, Peru.

REFERENCES

Braswell, F. M. and L. G. Smith [1981], A rocket-borne microprocessor-based experiment for investigation of energetic particles in the *D* and *E* regions, *Aeron. Rep. No. 96*, Aeron. Lab., Dep. Elec. Eng., Univ. Ill., Urbana-Champaign.

Durkin, C. and L. G. Smith [1981], A rocket-borne Langmuir probe for high resolution measurement of the ionospheric electron temperature profile, *Aeron. Rep. No. 96*, Aeron. Lab., Dep. Elec. Eng., Univ. Ill., Urbana-Champaign.

France, L. A. and E. R. Williams [1976], An improved Faraday rotation experiment for rocket measurement of lower ionosphere electron concentrations, *J. Atmos. Terr. Phys.*, *38*, 957-964.

Fries, K. L., L. G. Smith and H. D. Voss [1979], A rocket-borne energy spectrometer using multiple solid-state detectors for particle identification, *Aeron. Rep. No. 91*, Aeron. Lab., Dep. Elec. Eng., Univ. Ill., Urbana-Champaign.

Jacobsen, T. A. and M. Friedrich [1979], Electron density measurements in the lower D-region, *J. Atmos. Terr. Phys.*, *41*, 1195-1200.

Klaus, D. E. and L. G. Smith [1978], Rocket observations of electron-density irregularities in the equatorial ionosphere, *Aeron. Rep. No. 80*, Aeron. Lab., Dep. Elec. Eng., Univ. Ill., Urbana-Champaign.

Smith, L. G., L. H. Weeks and P. J. McKinnon [1968], Rocket observations of electron temperature in the *E*-region, *J. Atmos. Terr. Phys.*, *30*, 1301-1312.

Voss, H. D. and L. G. Smith [1977], Energetic particles and ionization in the nighttime middle and low latitude ionosphere, *Aeron. Rep. No. 78*, Aeron. Lab., Dep. Elec. Eng., Univ. Ill., Urbana-Champaign.

Zimmerman, R. K. and L. G. Smith [1980], Rocket measurements of electron temperature in the E region, *Aeron. Rep. No. 92*, Aeron. Lab., Dep. Elec. Eng., Univ. Ill., Urbana-Champaign.

D3

N81-32755

3. PARTIAL REFLECTION

This group is involved in the study of the *D* region of the ionosphere by the technique of partial reflection. This includes regular measurements of electron concentration by the differential-absorption technique for use in studies of *D*-region variability, further work on the differential-phase technique, improving measurement techniques for the lower *D* region, and partial-reflection drifts measurements. The research is supported by the National Aeronautics and Space Administration under grant NGR 14-005-181.

3.1 *Urbana Measurements*

R. M. Weiland has collected differential-absorption electron concentration and drifts wind data on a daily basis near local noon at the Aeronomy Laboratory Field Station near Urbana (geographic coordinates: 40° 10' 10" N, 88° 09' 36" W), from December 1980 through mid-February 1981. Data are digitized at 1.5-km intervals in the altitude range of 60 to 90 km. Files of 512 samples (or 3.4 minutes) are collected with 0 dB, 10 dB, and 25 dB of attenuation ahead of the receiver. The lowest attenuation file which does not saturate the receiver at a given altitude is retained for further processing. Five of these groups of unsaturated composite files (for a total of 15 files) are collected. The collection time is about one hour. The median of the five unsaturated values of electron concentration at each altitude is found to obtain a final electron-concentration profile. The collection routine has been further described in an earlier report [*Penny and Bowhill*, 1973].

During the past winter the data collection time was doubled. A partial-reflection drifts wind measurement was first made, followed by an hour of electron-concentration data collection, a winds measurement, a second hour of electron-concentration data, and ending with a winds measurement. Winds were measured at 3-km intervals from 75 to 90 km. The collection procedure was modified to fill one half hour during the approximately 25 days that the Urbana meteor radar was operational during this winter.

Figures 3.1 through 3.3 show the electron-concentration data obtained during the months of December 1980 through February 1981. Data plotted includes the electron concentration at 72, 76.5 and 81 km, and the A_x/A_o ratio at 81 km.

The daily winds data are being compared with the daily electron-concentration data to study the meteorological causes of the winter anomaly. By averaging the three wind profiles per day it was hoped that the effects of short-period fluctuations in the wind would be removed to provide a wind estimate more closely approximating the prevailing wind for that day. Preliminary comparisons of these winds data with electron-concentration data have not shown very much correlation, indicating that the noon winds are not a good predictor of the 24-hour prevailing winds.

The Urbana meteor radar system was operating for about 25 days during this past winter. The meridional prevailing wind is being compared with the electron concentration measured on those days. Figure 3.4 is a plot of the

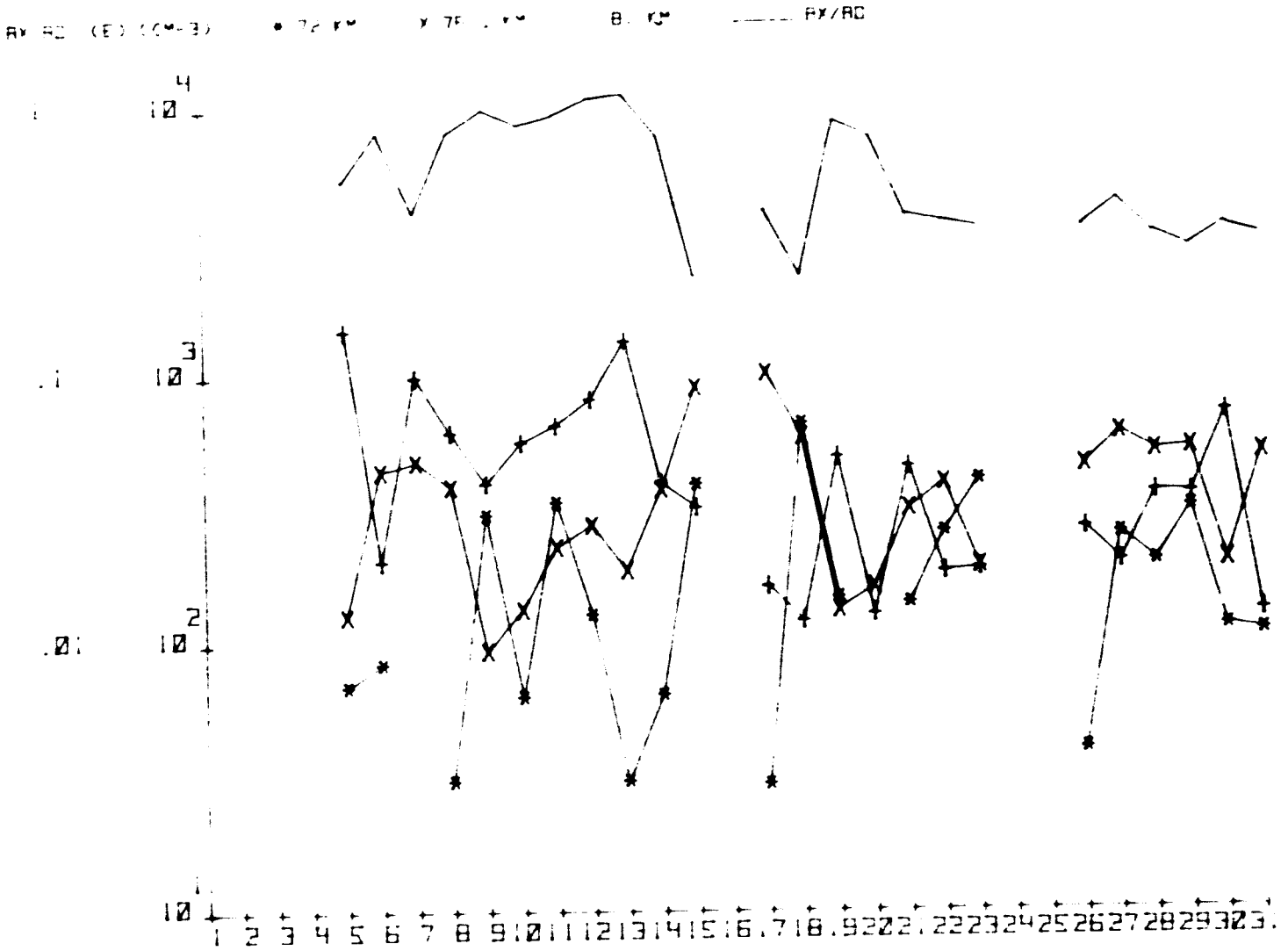

Figure 3.1 Daily plot of electron density at 72, 76.5 and 81 km and A_x/A_o at 81 km for December 1980.

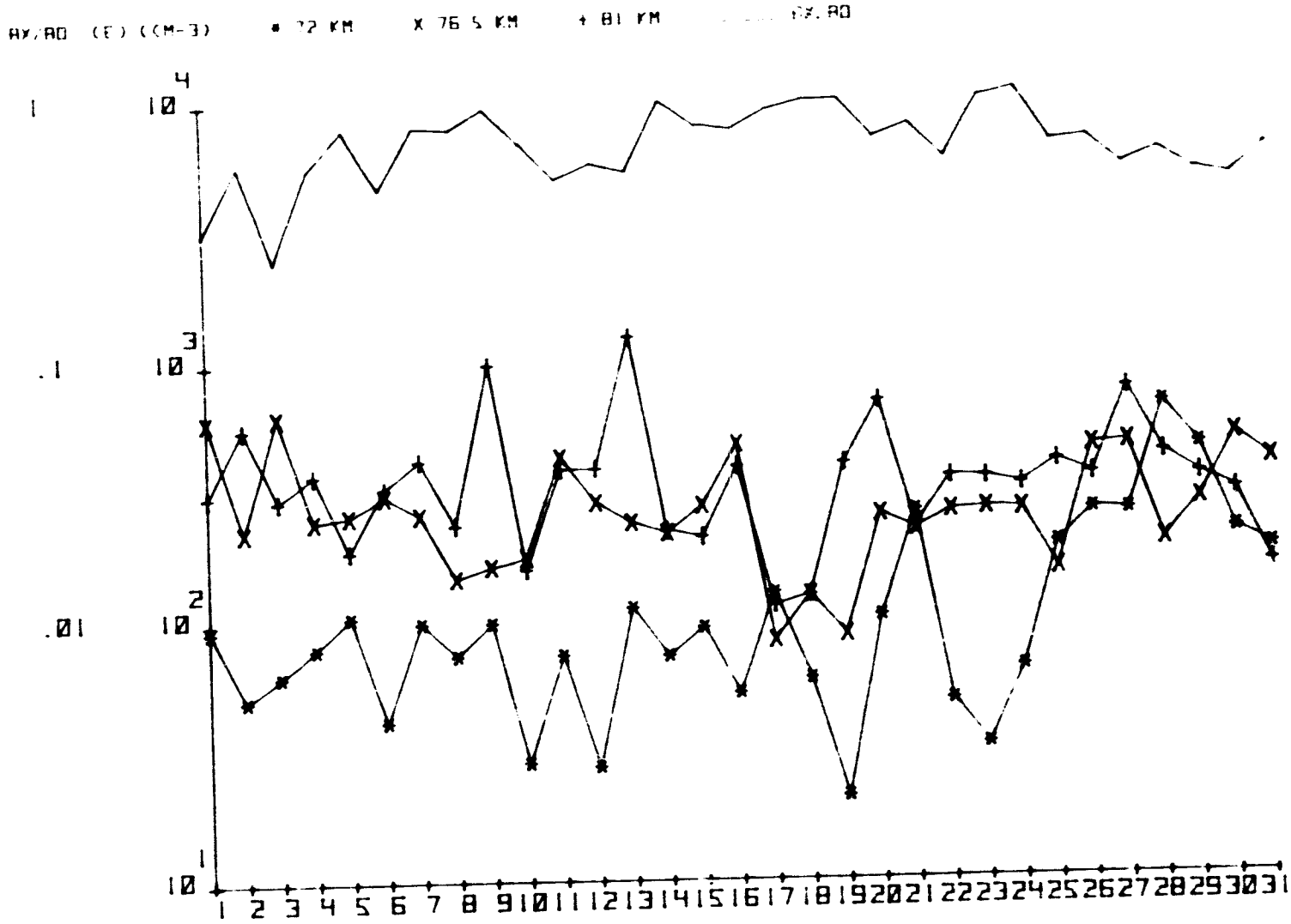

Figure 3.2 Daily plot of electron density at 72, 76.5 and 81 km and A_x/A_o at 81 km for January 1981.

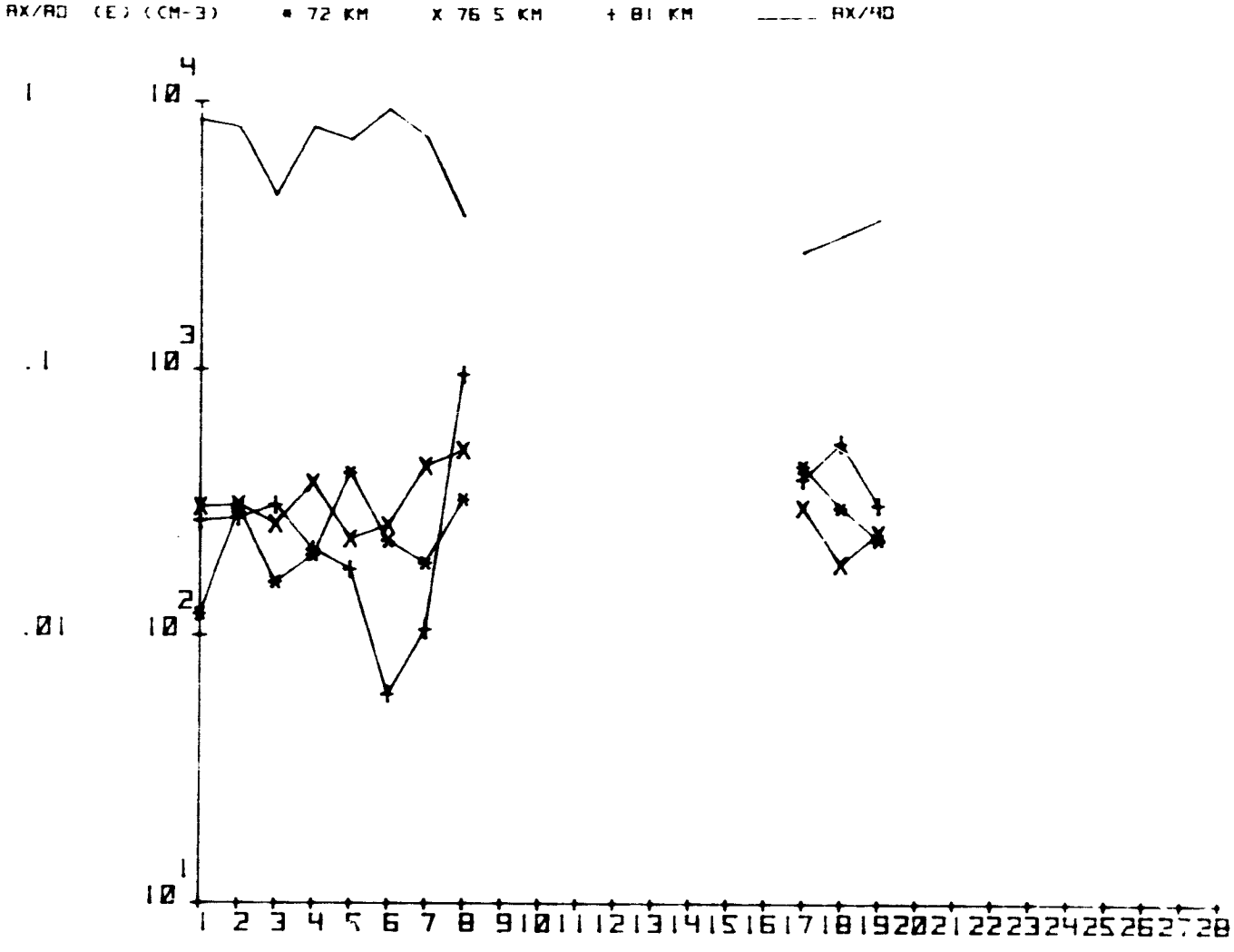

Figure 3.3 Daily plot of electron density at 72, 76.5 and 81 km and A_x/A_o at 81 km for February 1981.

meridional wind component and 81 km A_x/A_o (inversely proportional to the total electron content below 81 km). It must be noted that in this preliminary figure the winds data plotted are from a 24-hour period centered at noon on the day shown. For this comparison the winds for a 24-hour period centered at midnight the day before are needed, so when viewing Figure 3.4 the winds should be shifted to the right by one day. The correlation between winds and electron concentration shown in Figure 3.4 is quite good.

3.2 *Future System Development*

Investigation is being made into emulating the partial-reflection drifts experiment on an Apple microcomputer. Preliminary work has been done by R. Ruggerio into the various methods which can be used to implement this system.

The present method is that of the spaced antenna. This method involves the analysis of the amplitude information received from four spaced antennas. By computing the auto- and cross-correlation of the returned signals, the wind velocity is computed using the full correlation analysis.

The other method involves using coherent integration. This requires the addition of phase detectors to the present system in order to extract the in-phase and quadrature components so that a complex correlation is formed for the determination of the drift velocity.

The implementation of the microbased system will allow simultaneous measurements with meteor radar or coherent scatter which will enable accurate correlative measurements.

The analog-to-digital interface for this system is under construction. This interface will contain two channels making it compatible for either the amplitude or phase method. Height resolution of 1.5 km is expected from the interface which is identical to the present system.

If the amplitude method is used the second channel in the interface can be used as a backup circuit or to implement dual processing by using two microcomputers simultaneously. Dual processing may be implemented if the number of altitudes desired is more than a single microcomputer can handle.

REFERENCE

Denny, B. W. and S. A. Bowhill [1973], Partial-reflection studies of *D*-region winter variability, *Aeron. Rep. No. 56*, Aeron. Lab., Dep. Elec. Eng., Univ. Ill., Urbana-Champaign.

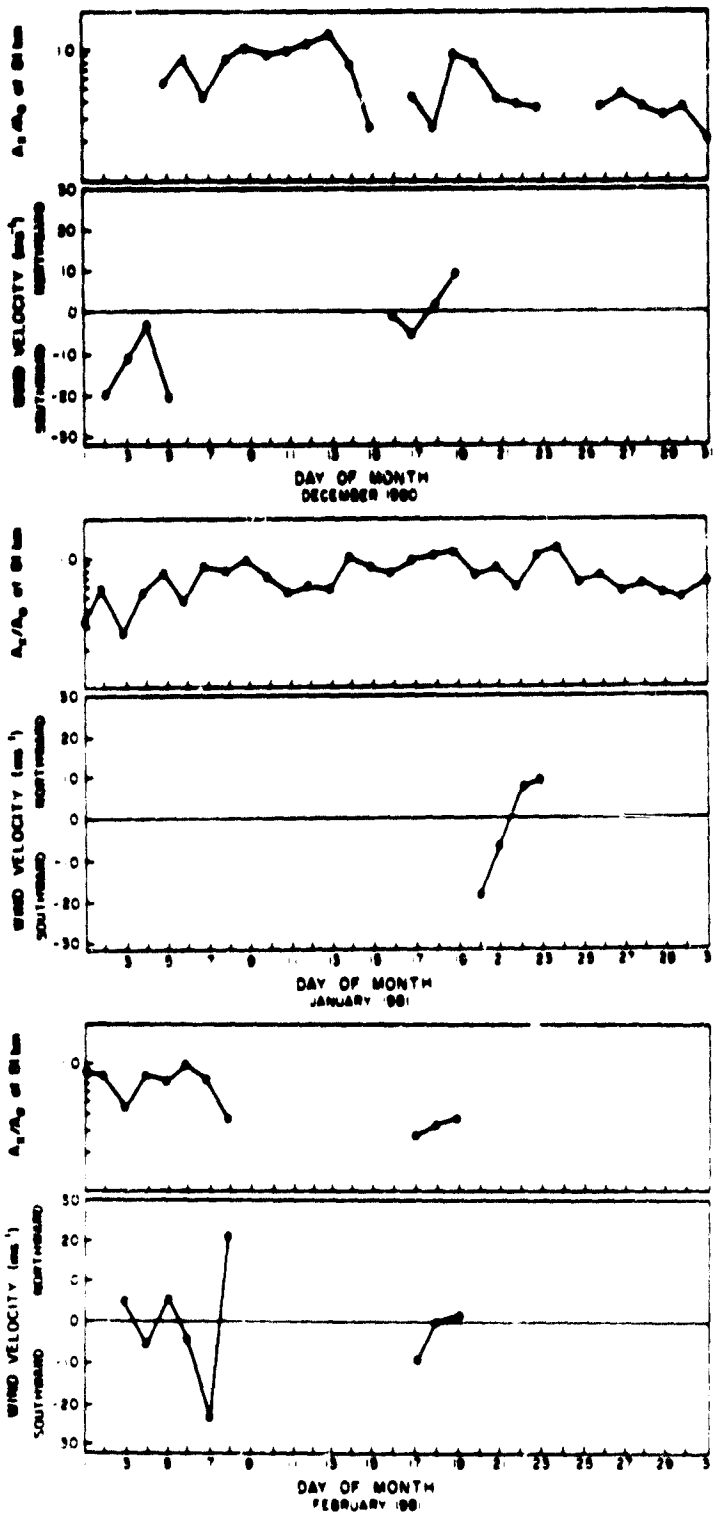

Figure 3.4 81 km, A_x/A_o and 86 km meteor radar winds (see note in text).

4. METEOR RADAR

Experimental and theoretical studies of the dynamics of the meteor region (75-105 km) are being conducted using a meteor-radar system. This research is supported in part by the National Science Foundation under grant ATM 79-09982; in part by the National Oceanic and Atmospheric Administration under grant NA-80-RAD-00016; and in part by the National Aeronautics and Space Administration under grant NGR 14-005-181.

4.1 *Meteor Radar Observations*

During the period October 1, 1980 to March 31, 1981, the radar has been operated approximately 700 hours, covering the periods:

November 4, 1980
December 2-5, 1980
December 16-19, 1980
January 20-23, 1981
February 3-8, 1981
February 17-20, 1981

The data have been fully analyzed to yield the north/south and east/west horizontal wind components, and curve-fitting routines are used to yield the daily mean winds, and the diurnal and semidiurnal tides.

4.2 *Lidar Correlative Study*

As discussed in Aeronomy Report No. 80-2 [*Edwards*, 1980], near-simultaneous measurements of the wind field and sodium density were obtained on January 19, 1980, March 15 and March 22, 1980 in order to study the effect of dynamics on the structure of the sodium layer. The results have been further analyzed and are summarized as follows: The east/west wind field has been reconstructed using the mean + diurnal + semidiurnal components, and compared with the sodium density profile at the same time. If the wind-shear mechanism for the downward sweeping of ionization is dominant, then one should see peaks in sodium density at roughly the same altitude where there is a wind mode, with westward winds above eastward winds.

On March 15, there is a node at 90 km with the requisite westward above eastward winds (Figure 4.1a). At the same time, the principal peak in the sodium density is also at about 90 km (Figure 4.1b). The profile shows very little wave activity. Similarly, the vertical wind profile on March 22 shows a node at about 94 km with westward above eastward (Figure 4.1c). The principal peak in the Na profile is at approximately 93 km, again showing good correlation with the tides (Figure 4.1d). More wave activity is present in the sodium profile, and a spectral decomposition of the north-south wind shows that the high-frequency components are strong relative to the diurnal and semidiurnal tide that day (Figure 4.2), as compared to the data of March 14-15 (Figure 4.3). If this correlation, between little wave activity in the Na profile and little high-frequency wave activity in the horizontal winds, carries sufficient weight, then we are in a position to separately identify

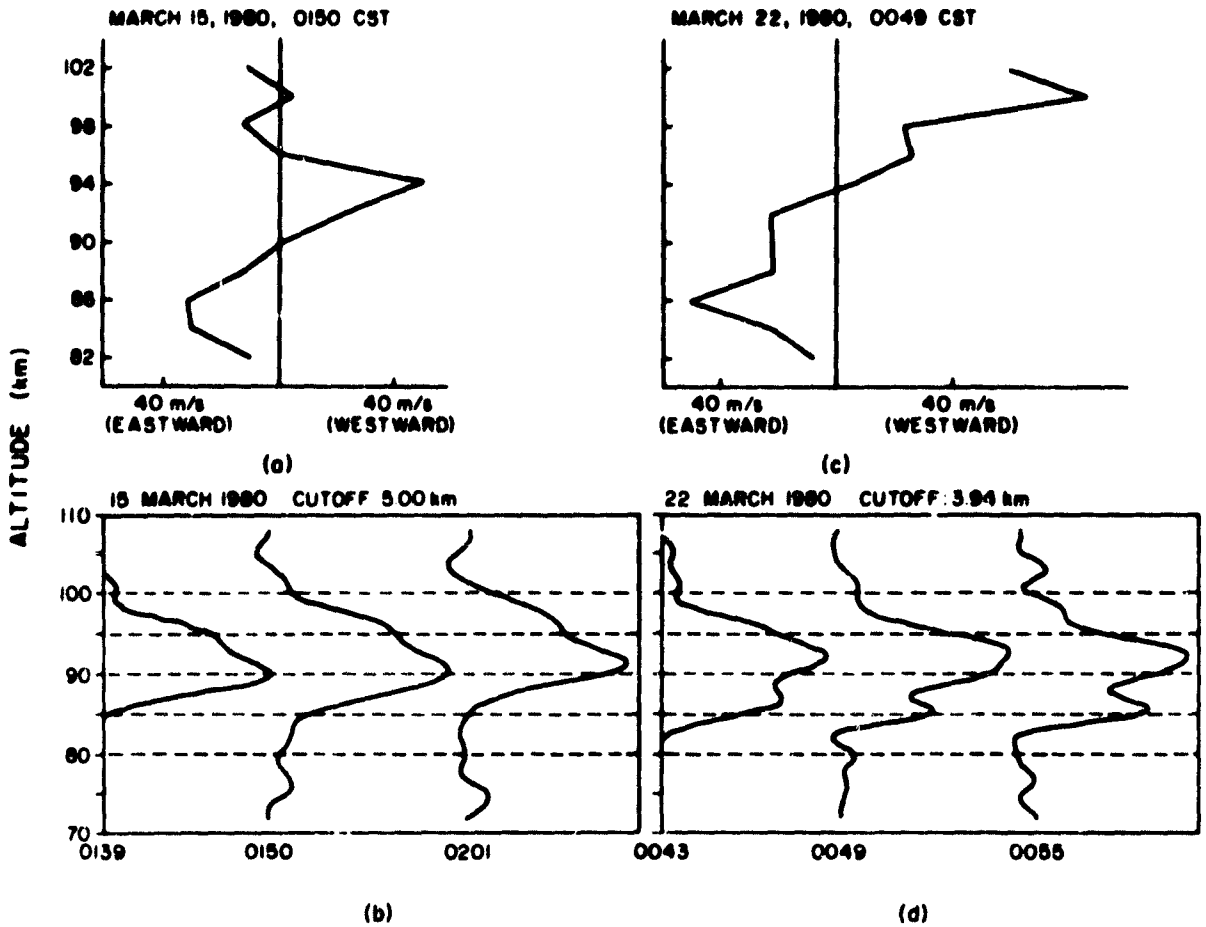

Figure 4.1 (a) Mean + diurnal + semidiurnal winds at 0150 hrs CST on March 15, 1980; (b) sodium density profile; (c) mean + diurnal + semidiurnal winds at 0049 hrs CST on March 22, 1980; (d) sodium density profile.

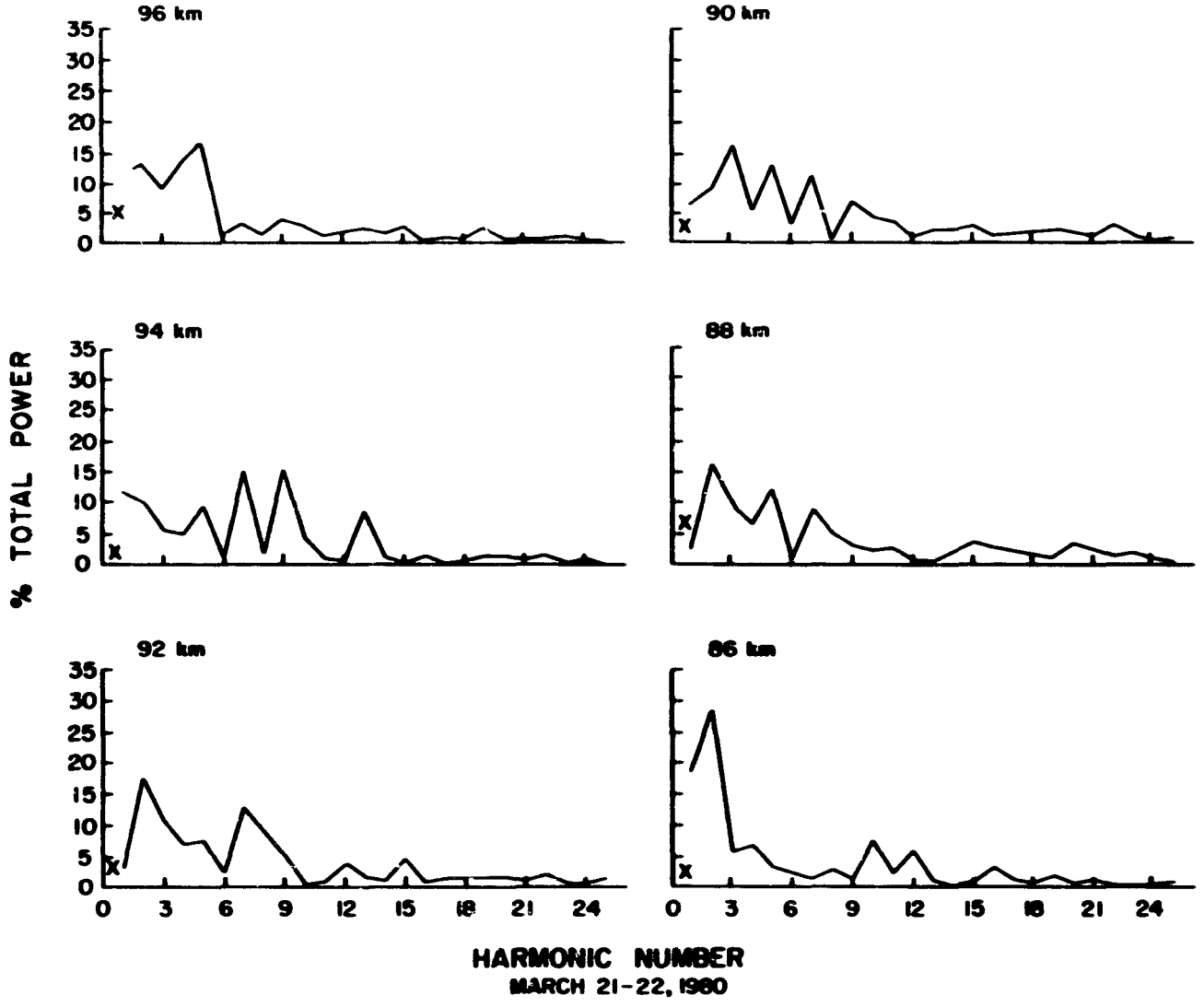

Figure 4.2 Power spectrum of north-south wind for March 21-22, 1980. Period is 48 ÷ (harm. #) "x" denotes mean wind.

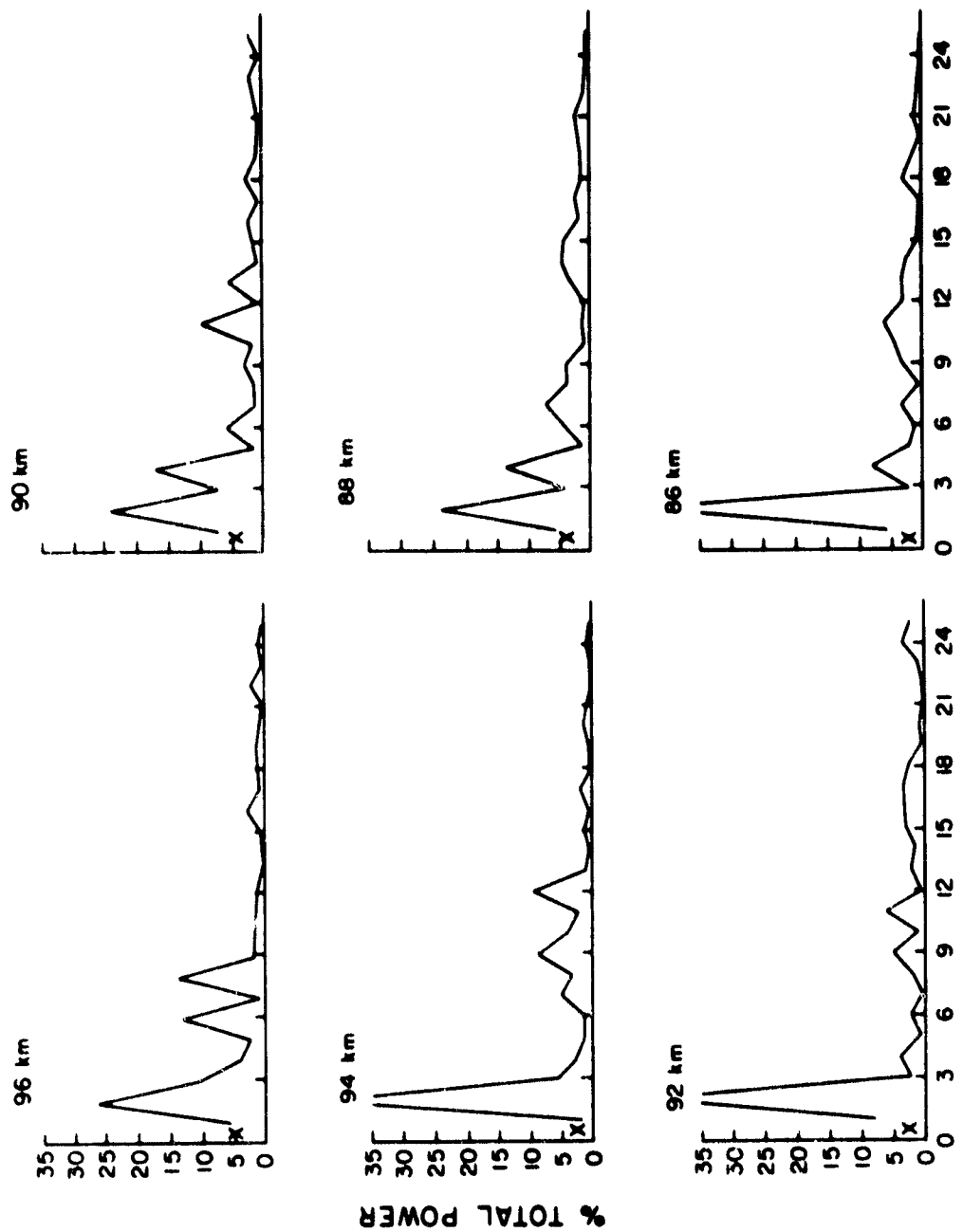

Figure 4.3 Power spectrum for March 14-15, 1980.

tidal and gravity wave effects, since the wind shear mechanism does not apply to north-south ion drifts. The high-frequency waves in the periodograms are definitely gravity waves.

Finally, the data from January 18-19 show a node in the wind profile at roughly 93 km (Figure 4.4a). At the same time, the sodium density profile shows a peak at 90 km (Figure 4.4b). This discrepancy is unresolved at the present time. However, the spatial periodogram reveals a vertical wavelength of about 9.1 km, whereas the analysis of the vertical structure of the semi-diurnal tide shows a wavelength of about 10.3 km, with downward phase propagation. This motion is evident in the lidar data, and it is plausible to suggest that the Na layer is indeed tracing tidal motion via the wind shear mechanism, in addition to tracing gravity wave density perturbations. Periodograms are noisy estimators of spectral information, and it is not unreasonable to suggest that the 9.1 and 10.3 km wavelengths correspond to the same phenomenon.

The results of these correlative studies, albeit modest, do seem to point in the right direction, and further analysis of meteor radar winds may determine which features of the sodium profile are due to gravity waves or due to tides.

4.3 *System Improvements*

An improved data collection system is presently being designed for the Urbana meteor radar experiment. The present system uses a Digital Equipment Corporation PDP-15 for real-time data collection and processing. The new system features two Apple II microcomputers, one for raw data collection and the other for preliminary processing.

The new system will provide the opportunity for simultaneous data collection with other experiments and will be more reliable than the old system. At the present time, correlative studies between experiments must rely upon interspersed data collection due to equipment conflicts. The new setup allows for simultaneous meteor-radar and partial-reflection data collection along with other experiments in the future. The reliability of the system will improve because of its modular design. Any component that fails can be quickly replaced.

Most of the work to date has gone into the investigation of the various languages available for the Apple II. The FORTH language provides low-level control of memory and is compatable with machine language. It seems to be the best choice for the raw data collection. BASIC and PASCAL are higher level languages which are easier to read, understand and maintain. The FORTH language is a faster processing language and it has now been extended to compute floating point operations. The processing language has not been selected.

Some of the hardware choices for the new system have been explored. A sample-and-hold array has been fabricated and bench tested, but final selection of the interfacing hardware must wait until the collection software has been written and is available for testing.

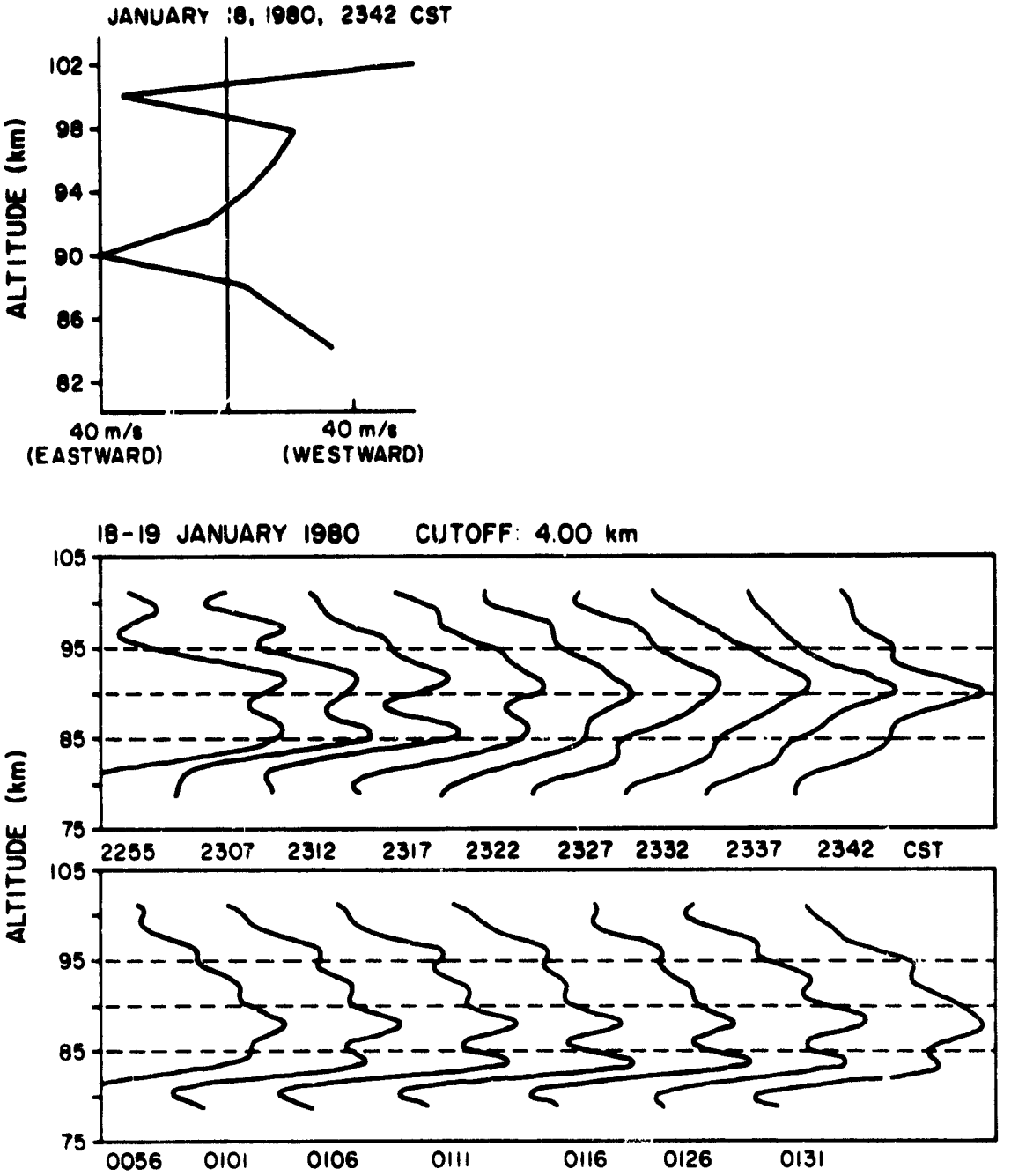

Figure 4.4 (Top) Mean + diurnal + semidiurnal winds at 2342 CST on January 18, 1980. (Bottom) Sodium density profiles on January 18-19, 1980.

4.4 *The Poker Flat, Alaska MST Radar as a Meteor Radar*

During the past eight months, an echo selection criterion has been developed to distinguish between echoes due to meteors from those due to turbulent mixing (regular echoes) that are received on the Poker Flat, Alaska MST radar. Several interesting results have been found. The daily variation of echo rates meeting this criterion can be partially explained by the geometry of the earth's orbital path intersecting the meteor trajectories and the geometry of the two antenna directions. The height profile of meteors agrees well with what is expected from the ablation process of meteors entering the atmosphere. Winds calculated from the doppler shift of the trails are not completely in agreement with the winds determined from the regular echo data. More work needs to be done in this area.

The selection criterion is schematically shown in Figure 4.5. A meteor echo must not appear on both receivers at (t_0, h_0). It also must not appear at (t_0, h_0) and (t_0, h_0+1) and (t_0, h_0-1). Nor can it appear at (t_0, h_0) and (t_0-1, h_0) and (t_0+1, h_0). Finally, it cannot appear at more than two of the eight remaining positions shown in the figure. Since each grid point represents a four-minute average of data, this criterion is probably too exclusive; more work will be done on relaxing the assumptions in the criterion.

Based on this criterion, histograms of daily meteor rates and height distributions were determined. The height distribution of the meteor echoes is shown in Figure 4.6. This profile can be explained in terms of the physical characteristics of meteors. As a meteor enters the atmosphere, heating and ablation begins. Depending on the mass and velocity of the meteors, these processes begin at 100-120 km where the air density is large enough to generate friction. As the meteor penetrates further, the exponentially increasing air density leads to an increase in ablation and ionization until the ionization reaches a maximum at roughly 92 km. At lower altitudes, the ionization falls off rapidly as the meteor diminishes in size. The small thickness of the meteor region (80-110 km) is the result of the rapid change in air density.

The daily meteor count for each receiver is shown in Figure 4.7. The hourly distribution is partially consistent with the earth's geometry and with the directions of the two antennas. The daily variation is not consistent with what is observed with the Urbana meteor radar system which peaks at 0500 and 1100 CST. This may be due to errors in the selection criterion and/or poor statistics due to the low echo rate on the Poker Flat MST radar. The Urbana meteor radar has a maximum echo rate of approximately 500 hr^{-1} compared to 4 hr^{-1} from the Poker Flat radar. When the MST radar is in full operation, the echo rate should improve by a factor of at least 100. Even with the current low echo rate, by looking at several days, a measurement of the prevailing wind and diurnal and semidiurnal components is possible.

As meteors enter the upper atmosphere, they vaporize forming trails of ionized particles. The trails diffuse rapidly but during their brief existence they reflect radio signals. Because the neutral-ion collision

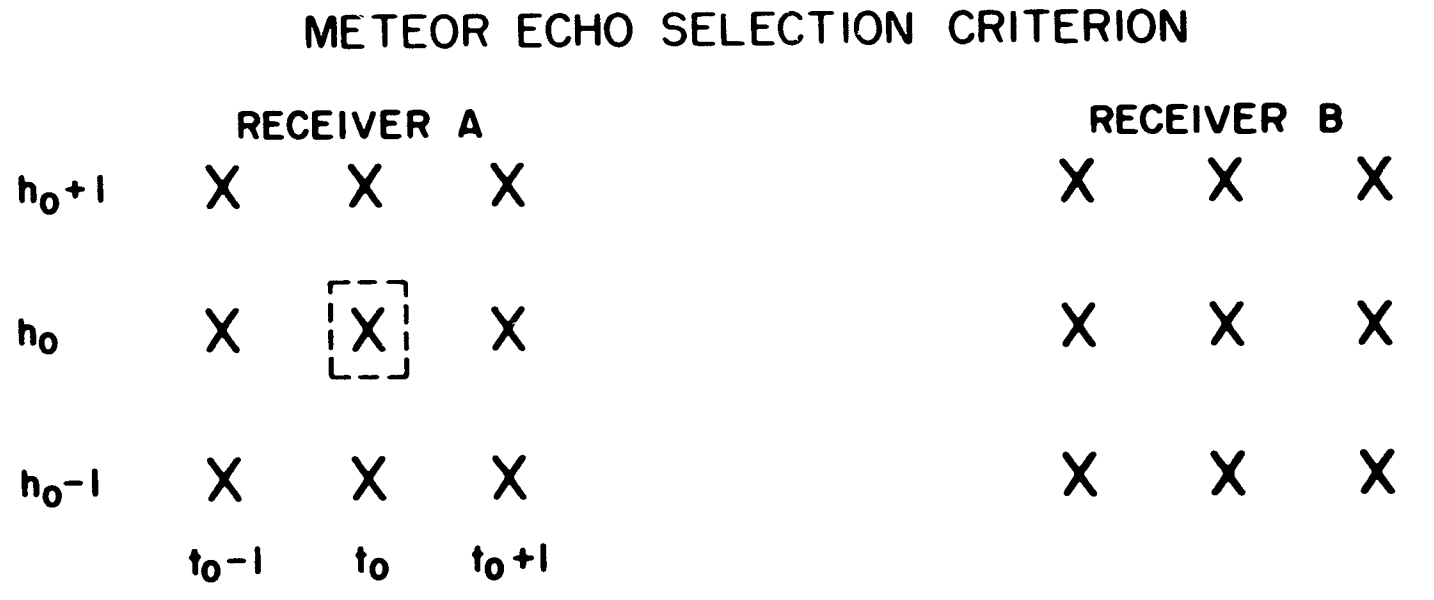

Figure 4.5 Meteor echo selection criterion: (a) Echo must not appear on both receivers at (t_0, h_0), (b) Echo must not appear at (t_0, h_0), (t_0, h_0+1) and (t_0, h_0-1), (c) Echo must not appear at (t_0, h_0), (t_0-1, h_0) and (t_0+1, h_0), (4) Echo must not appear at more than two of the eight remaining positions.

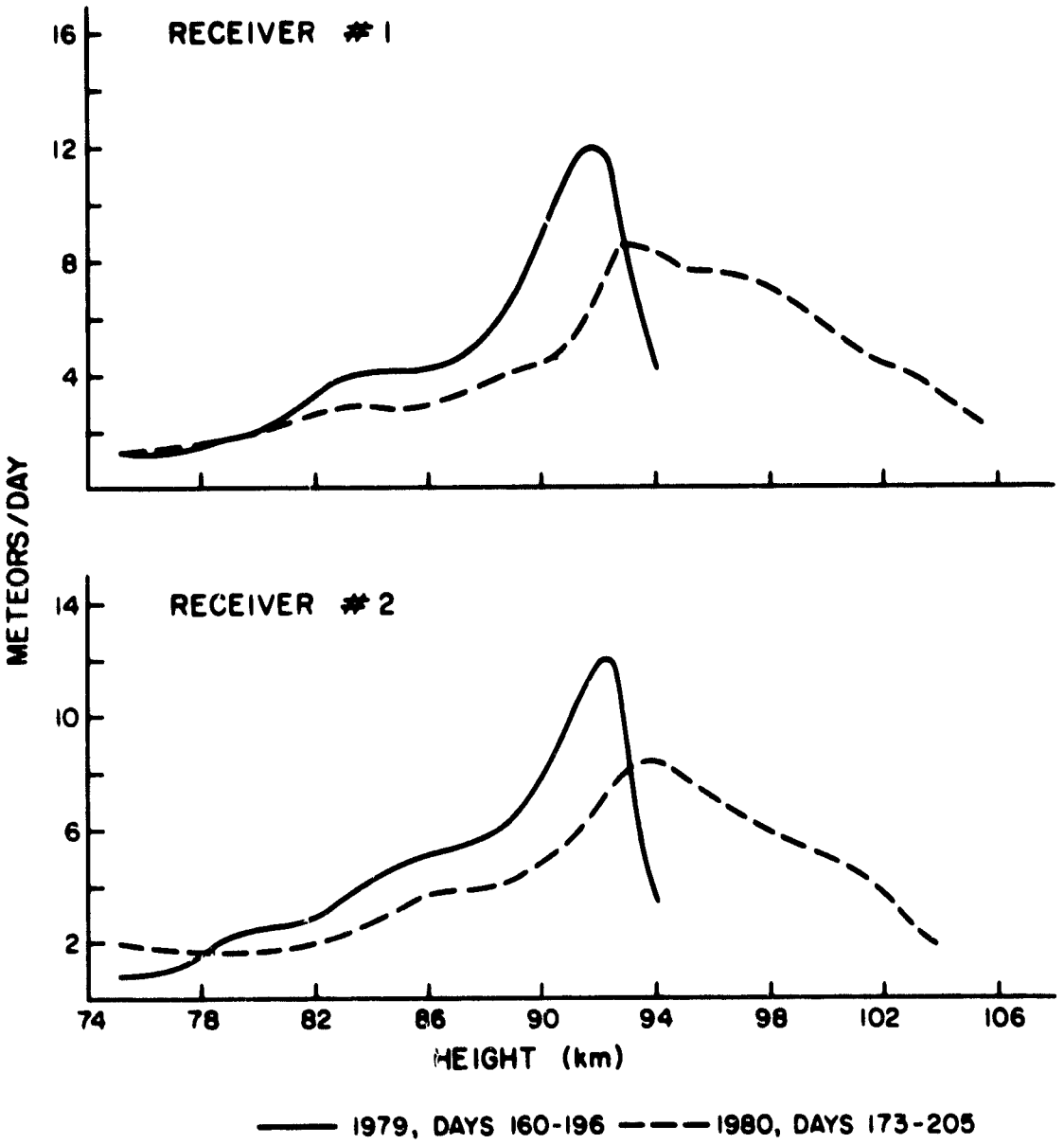

Figure 4.6 Height distribution echoes selected by meteor echo criterion.

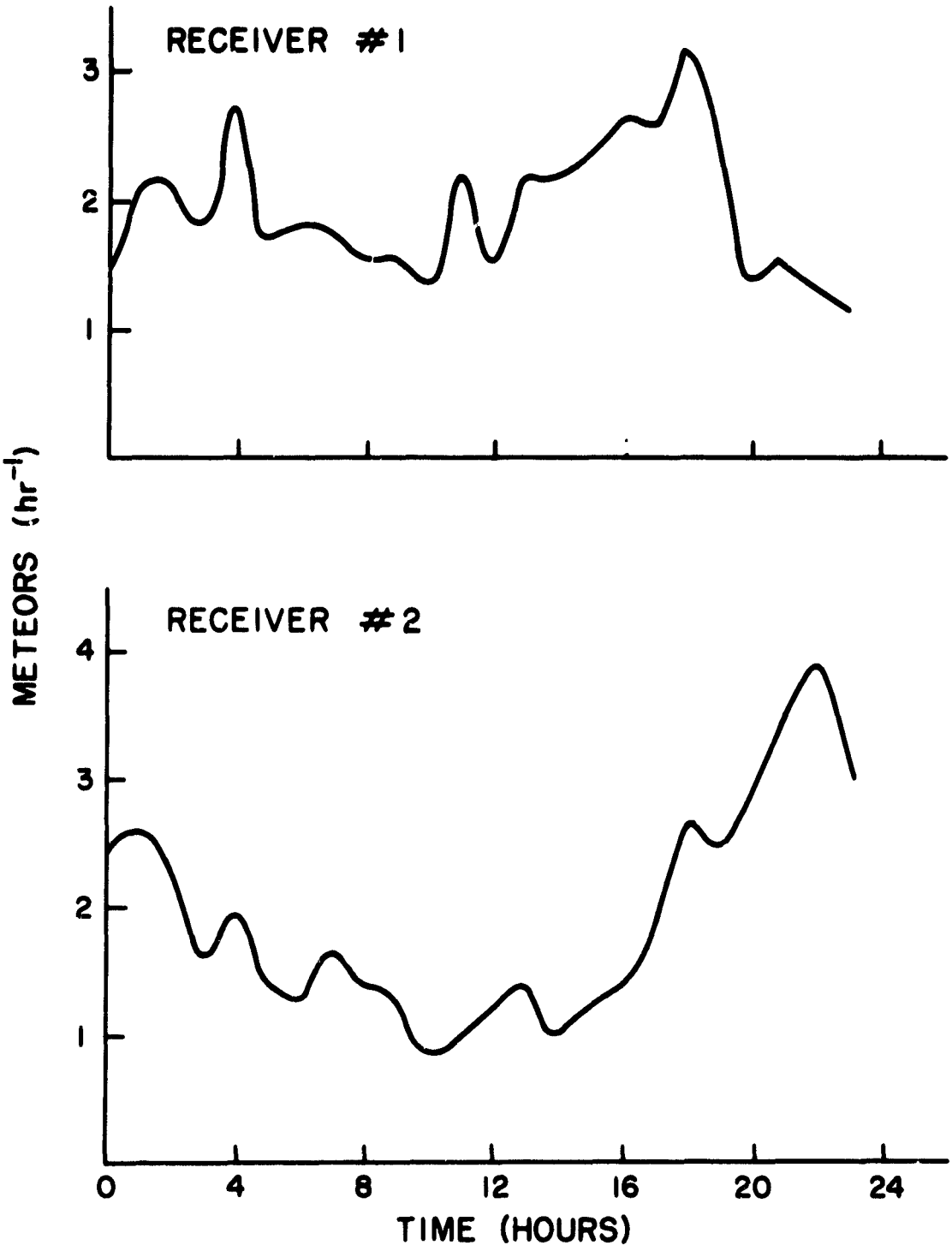

Figure 4.7 Daily variation of meteor rate.

frequency is so high (200 collisions s^{-1}) the ionized trail drifts with the neutral wind. Consequently, the Doppler shift of the return signal gives a measure of the wind motion.

The mean wind for days 160-196, 1979 and days 173-205, 1980 is shown in Figure 4.8. Also shown is the mean wind determined from the regular mesospheric echoes at Poker Flat and the mean meridional wind determined from the Urbana, Illinois meteor radar system during the same period. First, note that there is interannual variability in the mean wind. The eastward wind determined from the meteor echoes has the same trend as the wind determined from the regular echoes, however, it is approximately 20 ms^{-1} too low in comparison. This is true for both the 1979 and 1980 data and needs to be investigated further. The northward wind from the meteor echoes is also low when compared with the regular echo wind but the differences are not as great as those found in the eastward wind. A comparison with the Urbana northward wind shows that the mean wind is weaker at lower latitudes. This is in agreement with theoretical studies of the mean circulation in the middle atmosphere as discussed in *Schoeberl and Strobel* [1978].

The north and east diurnal tides for the same period are shown in Figure 4.9. The eastward diurnal tide from the meteor echo data has an amplitude that is low compared to that calculated from regular echo data. Also, the phase structure is scattered. This may be due to the daily variability in the 24 hour period wave. The northward diurnal tide compares more favorably both in amplitude and phase although values are still somewhat lower. The Urbana diurnal tide showed very little daily variability during this time interval based on daily Fourier analyses. Due to the low meteor echo rate at this time, daily Fourier analyses on the Poker Flat data cannot be calculated to compare with the Urbana results.

The eastward and northward semidiurnal tides are shown in Figure 4.10. Again, the eastward amplitudes are weaker from the meteor data but the phase structure compares fairly well. The eastward phase structure indicates an upward propagating energy wave below 88 km and downward energy propagation above 88 km. The regular echo data indicates only an upward propagation but it must be remembered that the regular echo data is approaching its upper height limit at that point. The northward tides compare more favorably. The differences between the Urbana and Alaska tides are seen in the phase structures here. The Urbana semidiurnal tide has a much longer vertical wavelength than the Alaska tide since its phase profile is nearly vertical.

The observed tidal structure has been compared with recent theoretical calculations from *Forbes* [1981]. The modeled eastward diurnal tide shows a strong upward phase propagation. The Poker Flat regular echo data has this same trend, but not as strong a phase tilt. Both the regular echo and meteor echo northward diurnal phase agree well with the modeled results indicating a constant phase height profile near 1200 hrs. The Urbana northward diurnal tide also has constant phase with increasing height which does not agree with Forbes' calculations which show a strong downward phase propagation.

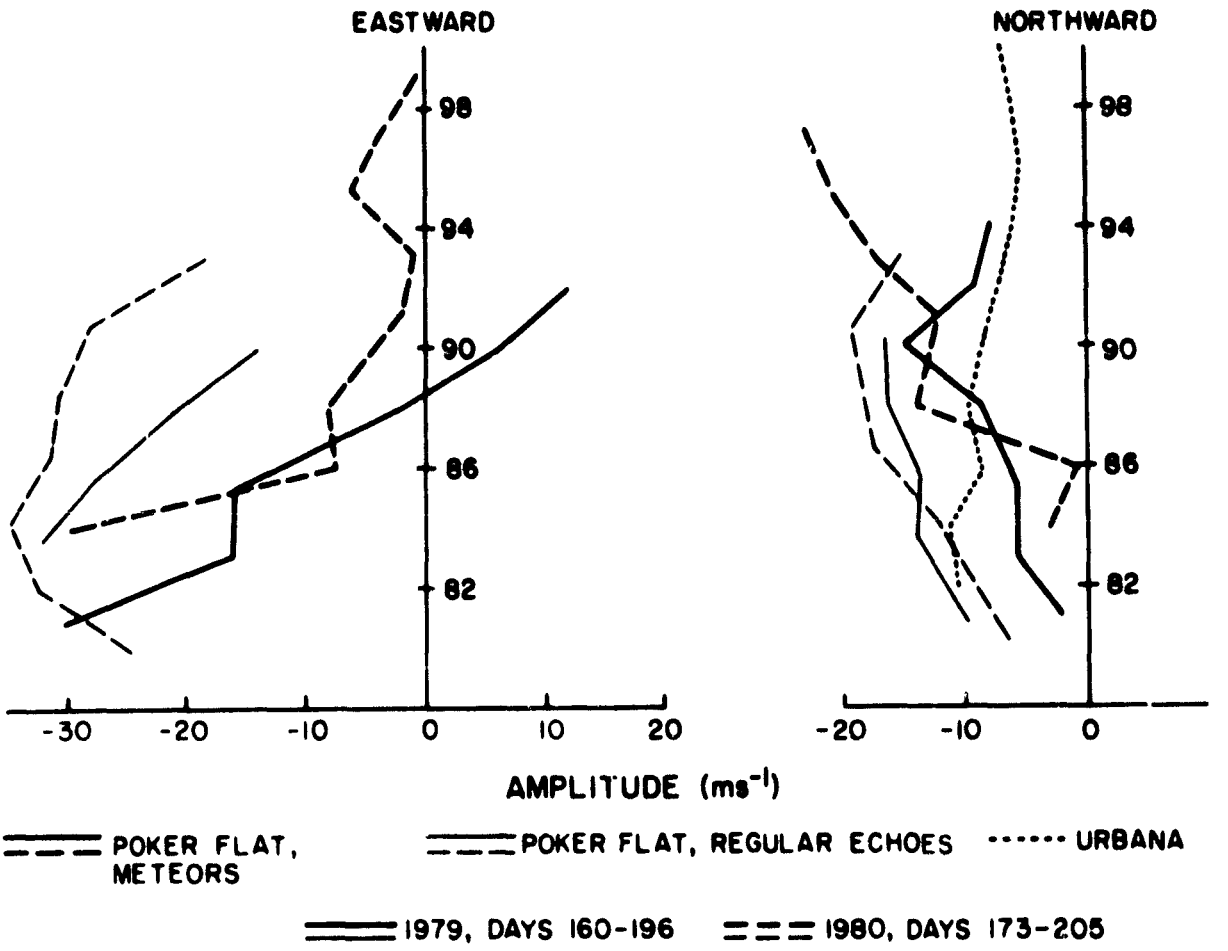

Figure 4.8 Mean eastward and northward winds.

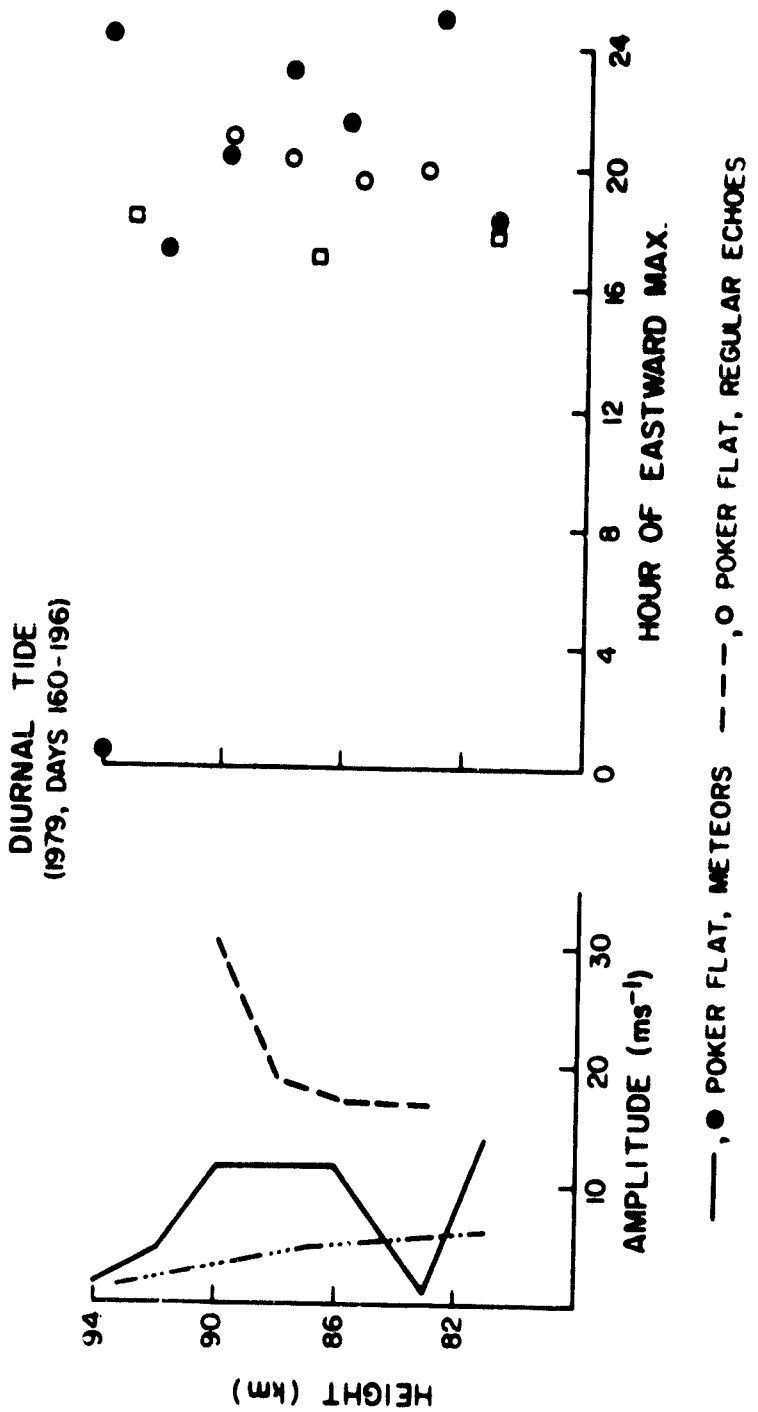

Figure 4.9a Eastward diurnal tide.

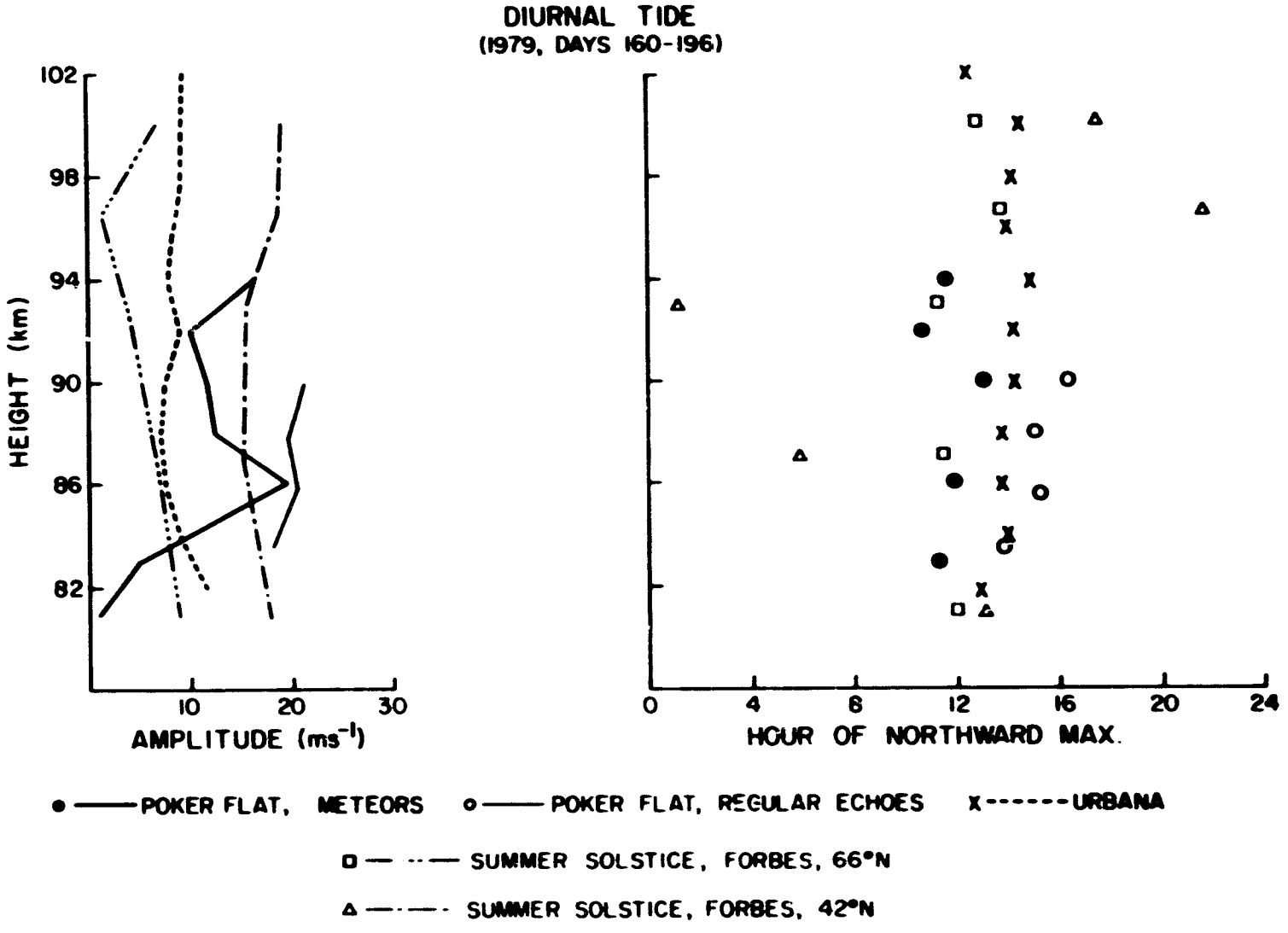

Figure 4.9b Northward diurnal tide.

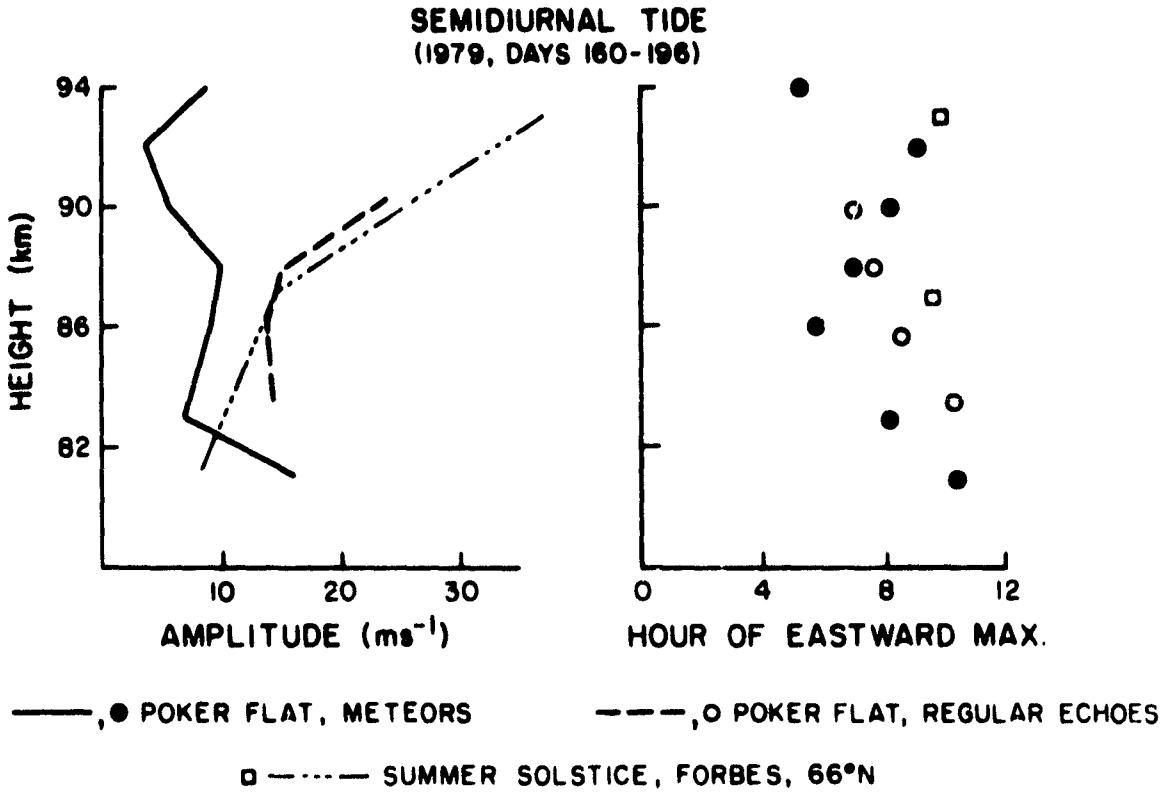

Figure 4.10a Eastward semidiurnal tide.

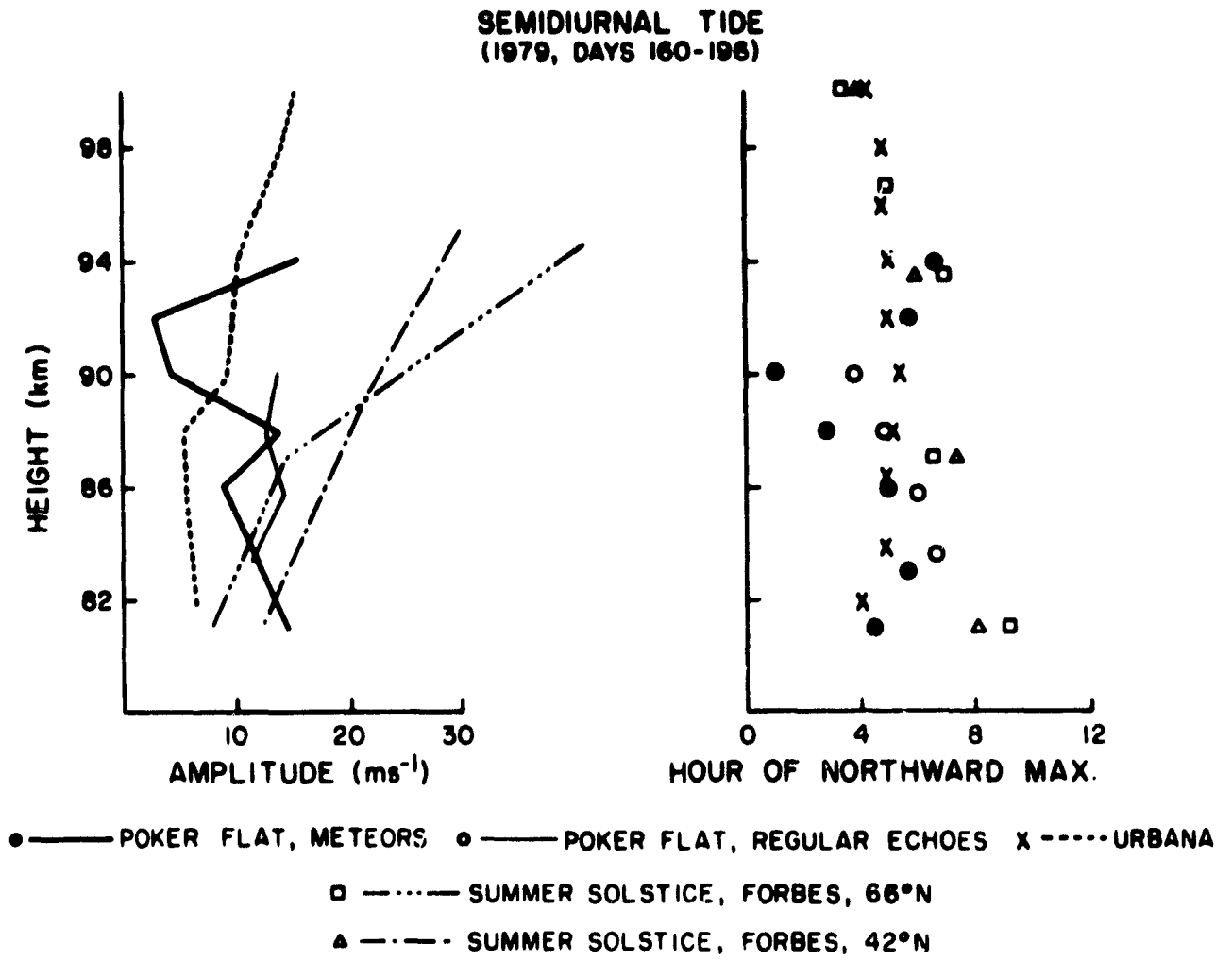

Figure 4.10b Northward semidiurnal tide.

The semidiurnal eastward tide agrees well with the calculations at the lower levels, however, the modeled tide does not reverse phase direction above 88 km. The phase structure of the Poker Flat northward semidiurnal tide also is in good agreement with the theoretical calculations. The Urbana northward tides do not have the downward phase propagation as indicated in Forbes' calculations.

REFERENCES

Edwards, B., (Editor) [1980], Research in Aeronomy, April 1 - Septe[illegible] 30, 1980, *Prog. Rep. 80-2*, Aeron. Lab., Dep. Elec. Eng., Univ. Ill[illegible]bana-Champaign.

Forbes, J. M. [1981], Private communication.

Schoeberl, M. R. and D. F. Strobel [1978], The zonally averaged circulation of the middle atmosphere, *J. Atmos. Sci.*, *35*, 577-591.

5. COHERENT- AND INCOHERENT-SCATTER RADAR

Experimental and theoretical studies of the ionized regions of the atmosphere are being conducted using high-power backscatter radars at VHF and UHF frequencies. The first year (1978) of data from the Urbana coherent-scatter radar have been analyzed by O. Røyrvik, K. Gibbs and S. A. Bowhill. This research is supported by the National Science Foundation under Grant ATM 78-21765 and ATM 78-15224 and by the National Aeronautics and Space Administration under grant NSG 7506.

5.1 *Array Processor Research*

5.1.1 *Introduction.* The needs of computer users are demanding faster and more powerful computers. Faster computers may be obtained by either improving the raw circuit speed or by using the same circuits in a more efficient architecture. Unlimited improvements in circuit speed are not possible due to fundamental physical constants such as the speed of light. Therefore new approaches to computer organizations must be found if projected demands of computer users are to be met.

Only one particular organization is dealt with in this study by R. O. Colbert: the array processor. In this form of processor, high throughput is achieved by introducing parallelism, that is to say, several processors performing nearly identical operations. In this work, the array architecture is examined on a new approach to the design of an array processor is proposed in order to take advantage of the recent advent of low-cost, high-performance microprocessors.

Illiac IV is taken here to be the conventional array processor (Figure 5.1). In an array processor, only the arithmetic units and memories are replicated and one single control unit (CU) drives the array of arithmetic units. For certain arithmetic units, the operation may have to be modified or suspended based on the contents of a gate or mark register in each processor. Hence, a minimum amount of control is kept local and each arithmetic unit plus its local control is called a processing element (PE).

Greater flexibility is obtained through the use of local indexing, mode control and routing. Local indexing allows each address broadcast by the CU to be modified by each PE. Mode control allows each instruction to be modified by each PE. Routing is defined as the method by which PE_i may obtain an operand which is stored in PEM_j ($i \neq j$).

5.1.2 *Issues of the study.* Several issues related to the array architecture, such as processor-memory interconnection, interprocessor communications, software requirements, system expandability and fault tolerance of system. This study examines the results when the processor-memory interconnection consists only of a single address bus and a single data bus. This research also explores the problem which results when the only form of communication between two PEs is through the stored memory (SM). This work considers the possibility of recoding uniprocessor programs into code which contains no context-dependent branches. That is, all PEs

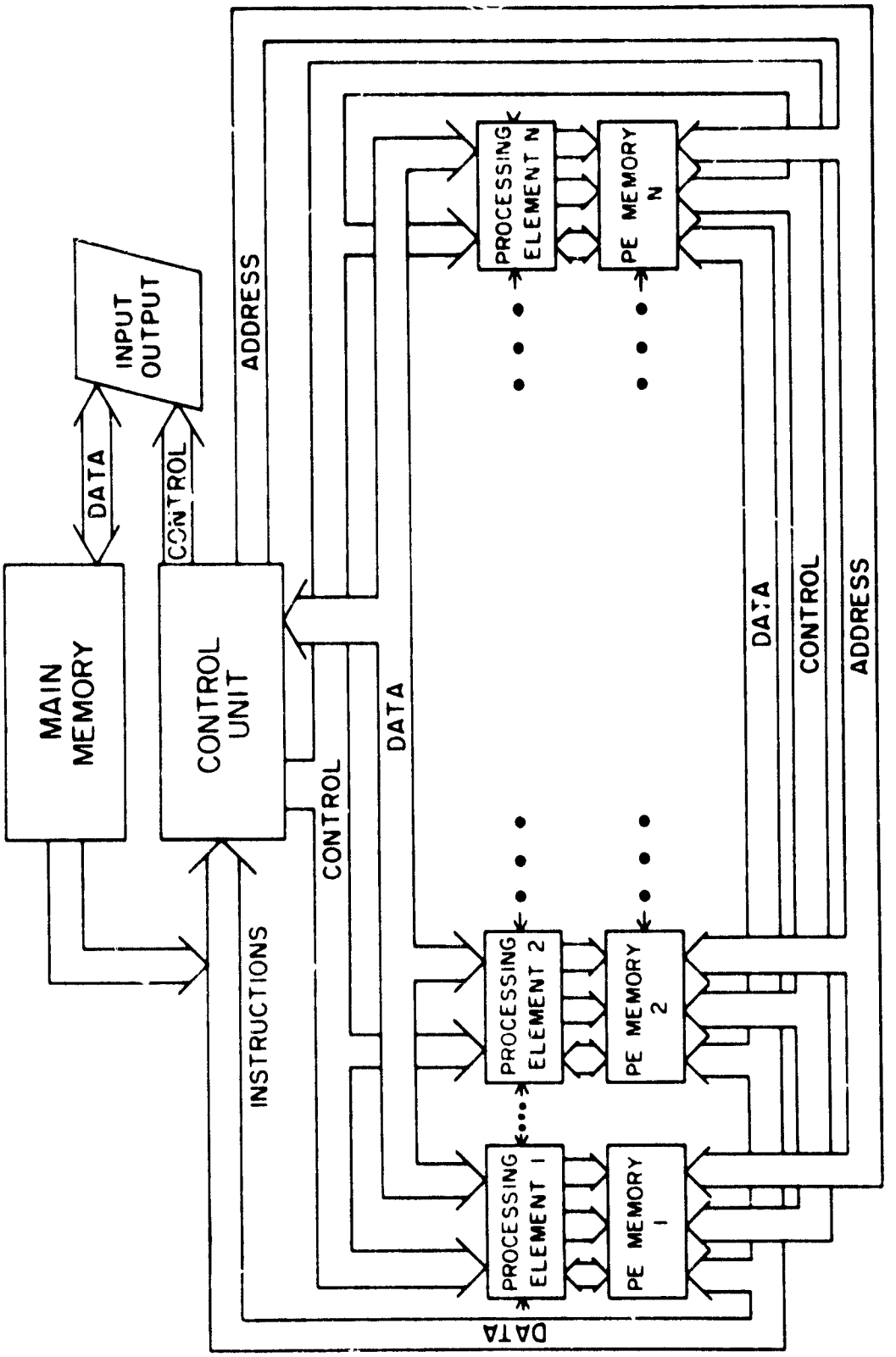

Figure 5.1 Conventional array computer.

must branch the same way when they encounter a branch instruction else the branch must be removed and that segment of code recorded. This work examines the expandability of an array processor which executes only Context-Independent Code and the possible fault tolerance and fault detection capabilities of such a system.

5.2 *Approach to a New Array Processor*

Context-dependent branches reduce an array system's throughput significantly. With no context-dependent branches (assuming little or no memory contention), the throughput of n processors is n times that of a single processor system. A program containing context-dependent branches requires that some of the PEs must wait while the other execute the branch of code they desire and then the groups reverse roles forcing the other PEs to wait while the first PEs execute their branch of code. The worst possible case for an array processor is the case of nested-context-dependent branching.

5.2.1 *Context independent code and its implementation.* A new concept in the generation of array processors is introduced here. This is the concept of Context Independent Code (CIC). The principle behind CIC is the elemination of context-dependent branches. One notes that CIC eleminates all context-dependent branches not all conditioned branches from the program. Context-dependent branches are those conditioned branches for which the data or condition may be different for different PEs. Conditioned branches which cause the program to loop a certain number of times are not context-dependent as all PEs branch the same way every time. Context-dependent branches must be recoded so that the program appears not to branch at all. For instance, the usual algorithm for multiplication shifts the multiplicand and tests each bit of the multiplier. If the multiplier bit is 1, the multiplicand is added to the partial product; if the bit is 0, the program skips the add instruction. For the conventional array processor, all PEs whose bit is 1 execute the odd instruction while the rest of the PEs are turned off.

This program written in CIC causes all of the PEs to execute the odd instruction, the difference being that those PEs whose bit is 1 add the multiplicand to the partial product while those PEs whose bit is 0 add zero to the partial product.

One might argue that adding zero is no better than turning a PE off. However, the CIC approach accomplishes two things which the previous approaches have not done.

1) All PEs are constantly synchronized in lock step mode.
2) The software is tailored to suit the array processor rather than tailoring the processor to suit sequential software.

The single restraint of CIC is that all PEs must execute the same instruction at the same time. This means that the operands of the instruction determine which branch the PE is actually executing. Several examples of CIC are included in the study, among these are 8 × 8 multiplication, 8-bit Magnitude of Twos-Complement Numbers, 16/8-bit Binary Division, 32-bit Accumulation and 32 × 32 bit Multiplication.

5.3 *Hardware Aspects of the Super-65 Multi-Microprocessor System*

After careful analysis of the available, single-chip, 8-bit microprocessors, the MOS Technology 6502 microprocessor was selected for the array processor.

Selecting the 6502 allowed the use of a versatile microcomputer known as the APPLE II. The APPLE II provides users with eight peripheral connectors along the back of the APPLE's main board. These slots allow the user to plug in proto-boards containing user-designed circuits. The APPLE II has available a supervising program called the APPLE System Monitor. Use of the APPLE II relieved the burden of writing a monitor for the array processor. The APPLE II also provides the user with a mini-assembler which allows one to type programs into the APPLE in assembly level language. For these and other reasons, the APPLE II is an excellent choice for implementing an array processor.

5.3.1 *Architecture of the overall system.* The Super-65 consists of four 6502 microprocessors, one being the APPLE II 6502, with three others. Each 6502 is given a private RAM of dimension 1K by 8 bits. The rest of the 6502's memory (the upper 63K) resides in the APPLE II. This is both RAM and ROM. The combined RAM and ROM are jointly designated as Stored Memory (SM). The architecture of the Super-65 (Figure 5.2) allows each processor to access its private memory at any time but only one processor may access the Stored Memory Address Bus at a time. All processors access the SM Data Bus on a Read. However, for obvious reasons, only one processor may access the SM Data Bus during a Write operation. The processor having control of the Stored Address Bus and the Stored Data Bus during a Write operation is called the Controlling Processor (CP). The CP has control over all stored resources. A convenient feature of the architecture is that it requires no modification of the APPLE II. The reason is that the APPLE II 6502 is removed from its socket and placed on a peripheral board. However, a 40-pin conductor connecting the 6502 to the empty socket allows the APPLE to operate as if the 6502 were actually still in the original socket.

The APPLE II 6502 is in control when the APPLE II is powered up, just as it would normally be. In order to designate another of the processors as the CP, one simply addresses the memory range $Cnxx, where n equal the processor number (1, 3, 5, or 7). Seven is the number given to the APPLE II 6502. When one accesses Cnxx (x = don't care), the APPLE II automatically activates the I/O Select line on the n th peripheral slot. This signal is used to give the processor in slot n control of the stored buses. When one accesses C\phi$n$\phi$ (n = processor number + 8), the APPLE II automatically activates the Device Select line on the n th peripheral slot. This signal is used to stop the clock of the n th processor. When one accesses $CFFF, the APPLE II automatically activates the I/O Select line on all of the peripheral slots. This signal is used to resynchronize and restart all of the processors simultaneously.

As the execution of CIC programs requires that all of the PEs have the same address at the same time, a minimal amount of fault detection was implemented by simply comparing the address on each of the private address

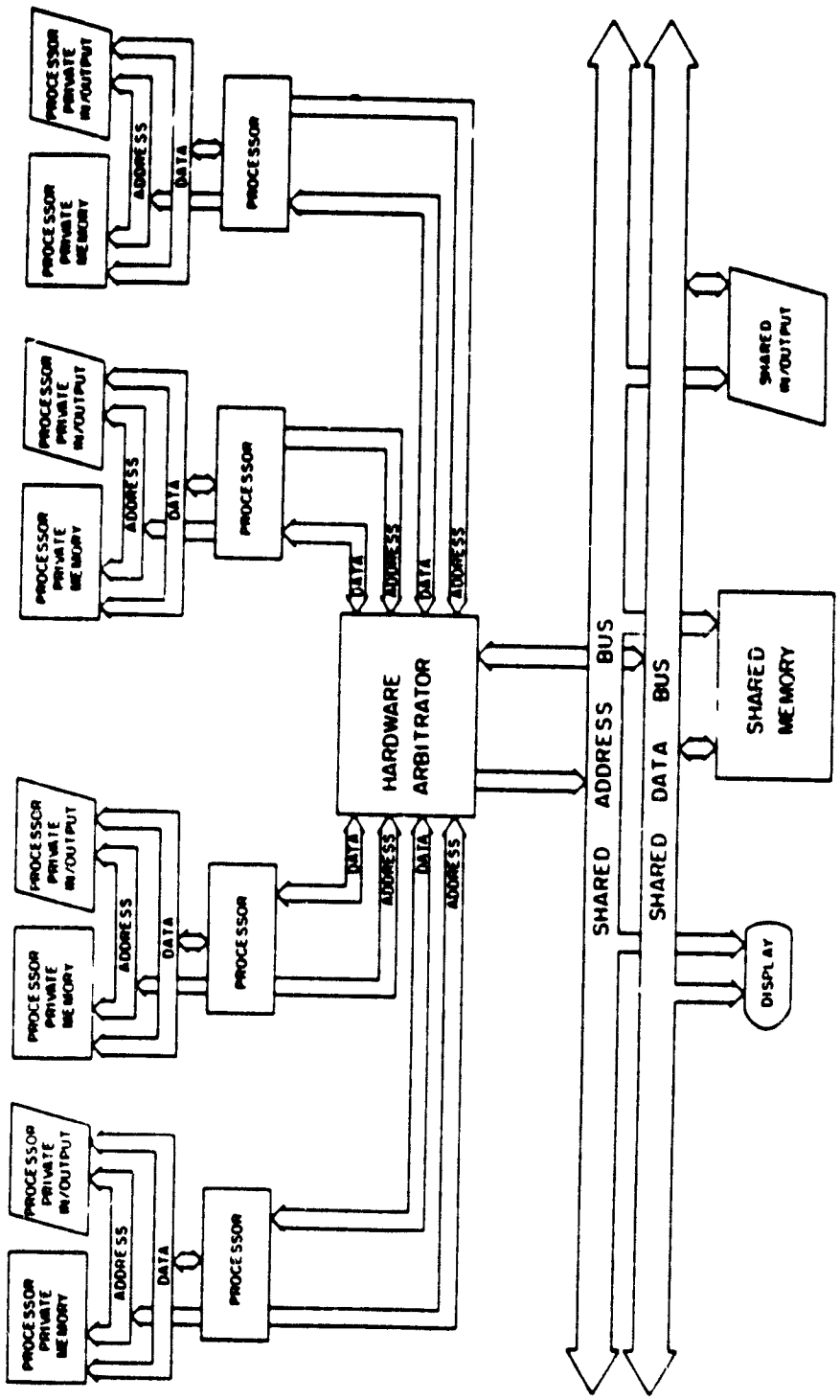

Figure 5.2 Super-65 system block diagram.

buses to the address on the stored Address Bus and lighting on LED if they did not match.

Finally provisions has been made for the inclusion of a 6522 Versatile Interface Adapter (see Figure 5.3) which contains two 8-bit parallel ports, on each of the processor boards.

5.3.2 *Summary.* The main objective of this work was to assert that recoding of microprocessor programs into CIC programs is feasible for an important set of applications. This objective was achieved by implementing a four-processor array and recoding several programs for it. The programs were divided into two categories, independent and dependent data handling. The first catagory allowed each processor to work on a separate set of data so that no processor required any results from any other processor in order to complete its task. The second category required each of the processors to work on a subset of the entire problem. This meant that the processors needed to communicate at various times in order to complete their task. It was found that for the set of independent-data recoded programs the throughput of an array of n processor would range from 0.45 n to n times the throughput a single processor. For the set of dependent data recoded programs the n processor array would achieve a throughput of approximately 0.3 n to 0.6 n (see Table 5.1) as long as the carry propagation delay is minimal. For the architecture chosen, their delay will not be minimal as n gets very large and this is one weakness of this architecture. One can see then that so long as carry propagation delay and the time required to store final results in Stored Memory are insignificant, one may achieve roughly a linear increase in throughput by adding more processors. This is, of course, after the initial penalty for the recorded program has been taken into account. In theory, then, one may achieve arrays of thousands of processors each of which adds on incremental throughput to the overall system.

There are several areas for further research. Among them is the pursuit of the ideal microprocessor solution of the carry propagation delay problem and of the problem of storing to Stored Memory and the recoding of more sample CIC programs to obtain a better understanding of the potential for and against CIC programs.

5.4 *Interface Between HP9830A and APPLE II*

The final stage of post-processing for the Urbana coherent-scatter radar is presently done on a Hewlett-Packard 9830A desktop computer with pen-plotter and paper tape reader. Brief descriptions of the post processing are contained in *Gibbs and Knobil* [1979] and *Edwards* [1979].

K. Gibbs has built an interface between the HP9830A computer and an APPLE II plus microcomputer. There are several reasons for having a bidirectional link between these two machines: 1) the pen-plotter attached to the HP9830A can be used from the APPLE II computer; 2) the APPLE II, which is a much faster machine, can be used for more complex post-processing; 3) the data previously collected can be transferred to APPLE II disk storage to be compatible with an APPLE II based data-collection system under development. The design of the interface is discussed on the next page.

Table 5.1 Recoding factors for the sample program.

	Independent Data	Dependent Data
8-Bit Magnitude	0.33	
8 × 8-Bit Multiply	0.53	
16/8-Bit Divide	0.45	
32-Bit Accumulator	1.00	0.60
32 × 32-Bit Multiply	0.59	0.30

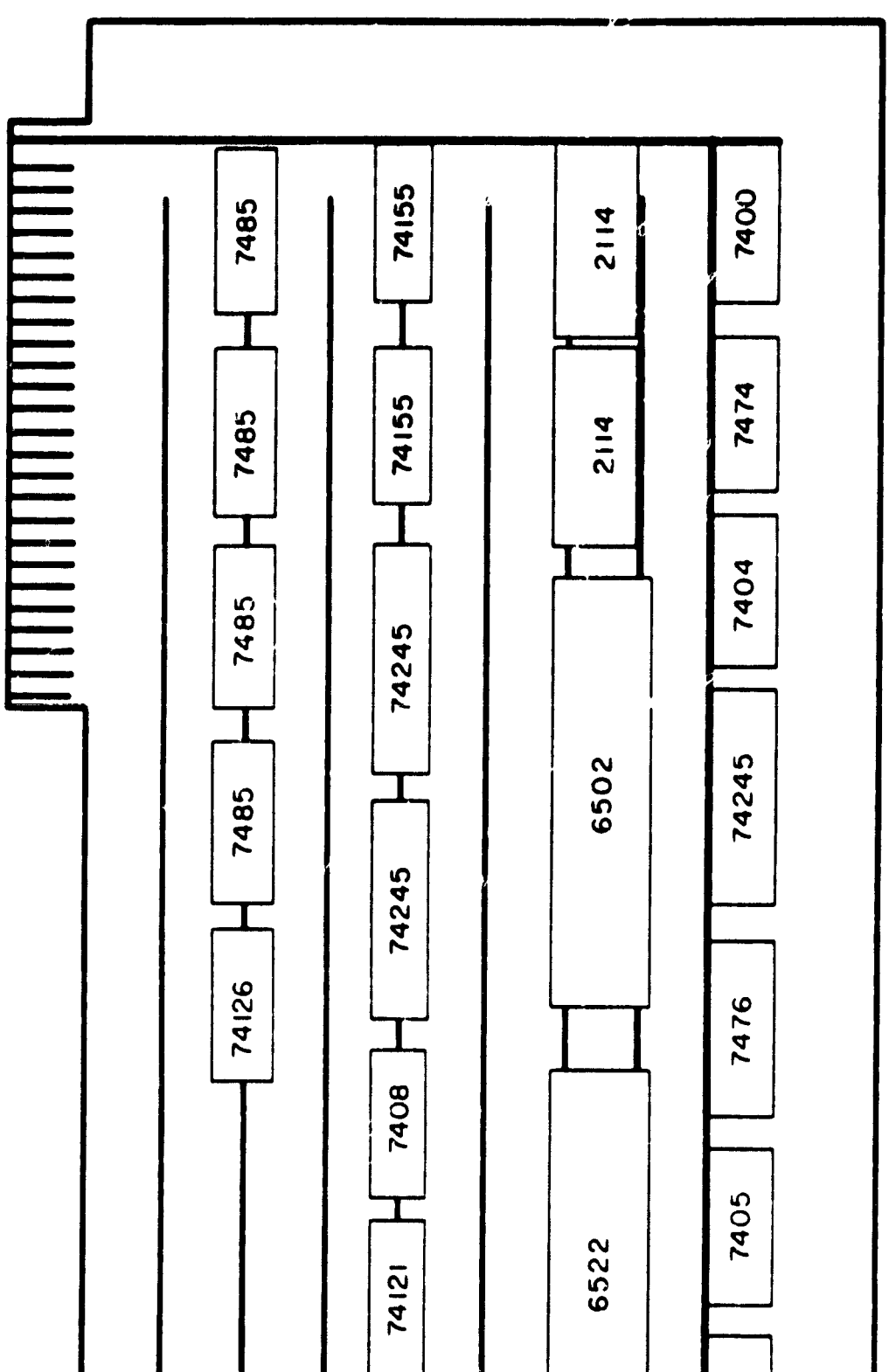

Figure 5.3 Processor card layout.

The HP9830A section of the interface is a standard HP11202A I/O TTL interface card. The card is bidirectional with separate lines for input and output. The inputs are terminated with an active pullup and the output lines are driven open-collector. All signals on the HP lines are inverted. A handshake control pair is also provided on the card.

The APPLE II section of the interface is shown in Figure 5.4. It consists of a 6522 VIA chip and several TTL chips to adapt the 6522 to the HP line conditions and the APPLE II bus timing. Port B of the 6522 drives open-collector inverters to transfer to the HP9830A. Lines from the HP9830A are actively terminated, driving port A of the 6522 through inverters. The 74LS74 adjusts the timing signals from the APPLE II to properly run the 6522. Finally, the control pins are wired for a handshake mode for either direction of transfer. The interrupt flags for both parts are raised together however so that switching data directions requires clearing the flags before starting.

5.5 *Construction of VHF Radar Preprocessor*

During this period much of the preprocessor was constructed and debugged. The hardware consists of four 4½" × 9" vector boards with standard wire wrapping techniques used for interconnections on each board. The four boards are contained in a standard equipment rack chassis allowing interboard communication via a wired backplane of the four boards, Board #1 contains the preprocessor memory (4K RAM), the memory address register (MAR) and the arithmetric logic unit (ALU). Board #2 holds the control store (two 32 × 8 bit ROMs), instruction decoders and control logic. Additional control logic resides on Board #3. Board #4 contains the sample and holds, analog-to-digital converters and a pair of latches.

Two valuable debugging and troubleshooting aids were included in the preprocessor design, single step capability and external access to the instruction bus. The single step circuitry disables the system clock and allows the user to issue individual clock pulses. The preprocessor executes one instruction for each clock cycle hence by single stepping the preprocessor can be examined before and after an instruction execution and the change in logic state determined.

External access to the instruction bus enables the user to issue any desired instruction to the preprocessor. Combined with single stepping the user is able to test any sequence of instructions desired observing the change in logic state for each instruction. This capability was used to test the microcode which will control the preprocessor operation. At this time the preprocessor correctly single steps through the entire microcode program. The next step is to program the control store PROMs and run the preprocessor from its 10 MHz system clock. This work was done by F. Zendt.

5.6 *New Coherent-Scatter Antenna*

The specifications and preliminary design configurations for a new coherent-scatter phased array antenna have been reported in *Edwards* [1980]. The proposed antenna shall have an aperture of 40.92 MHz over a 1 MHz band-

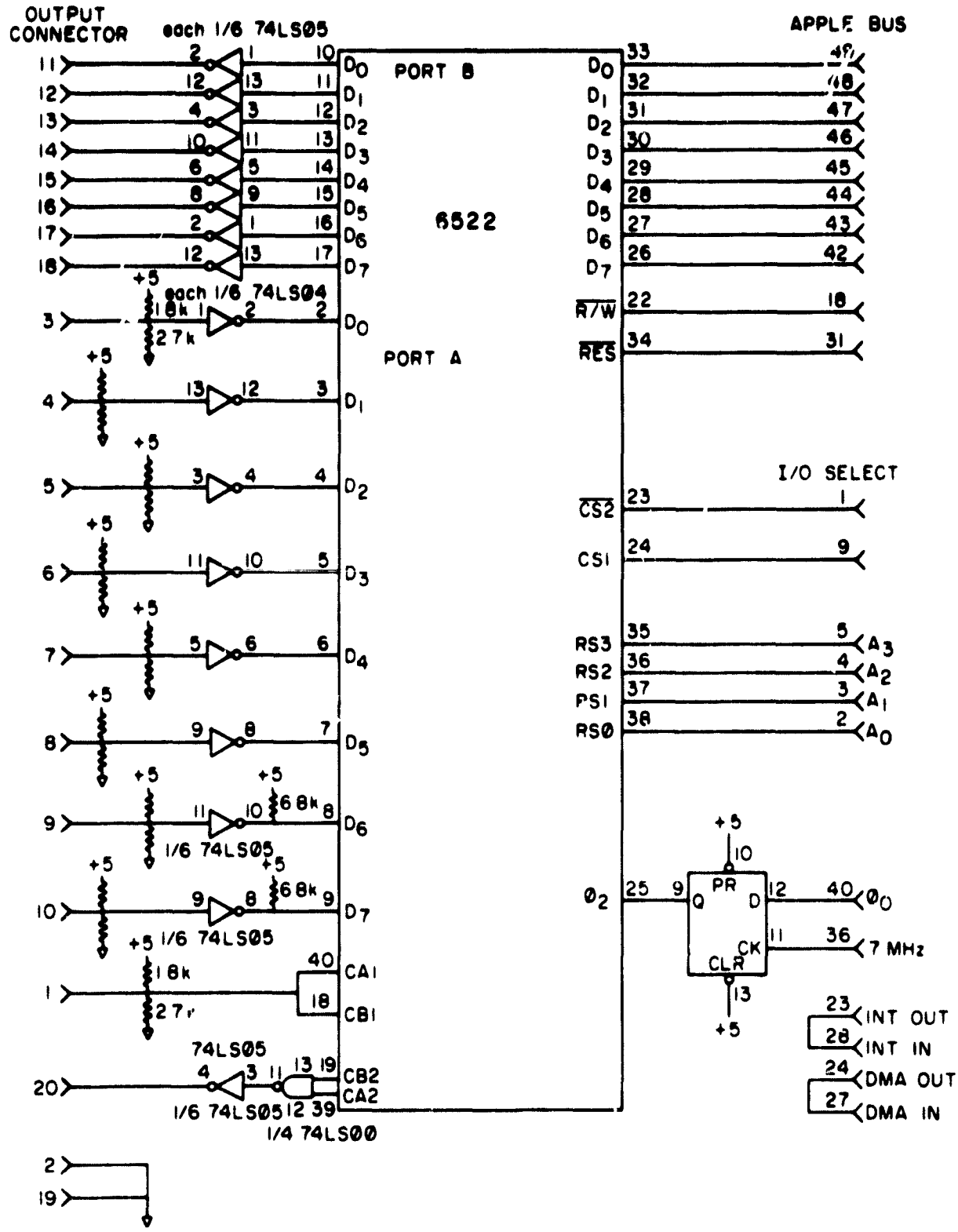

Figure 5.4 Schematic diagram for the APPLE II - HP9830A interface card installed in the APPLE II.

width. The array will be steerable in two orthogonal planes to discrete angular directions of 30 degrees from the vertical, in addition to a vertical pointing direction.

A proposed realization is to space half-wave dipoles on a square grid of one half wavelength spacing, a quarter wavelength above ground plane. To scan the beam in one plane, progressively phased excitation currents of 0, 90, 180, and 270 degrees are applied along each row of elements. Likewise, applying the progressively phased excitation along the columns scans the beam in the orthogonal plane. Feeding all elements in phase produces a vertical beam. This arrangement results in every fourth element, in each row or column, being feed in identical phase for each pointing direction. The inphase elements will be hardwired together into 16 interlaced arrays. Therefore, emanating from the antenna are 16 ports which scan the beam when excited with the appropriate phases.

To evaluate the performance of such a system, a scale model has been built for antenna pattern studies by D. Tanner and J. Loane. To cover the required aperture the full scale realization will contain in excess of seven thousand dipoles. The model, however, has been limited to a small section of 64 dipoles (8 × 8) due to practicality and constraints of the available antenna range and equipment. The scaled wavelength of the model is exactly 6 inches corresponding to a frequency of approximately 1.97 GHz. The unscaled wavelength is 24 feet; thus the frequency scaling factor is about 48.

The model is fed through 50 Ω coax cables of matched electrical length. Thirty-two half-wave baluns were etched on Rexolite PC board to convert the unbalanced feeders to a balanced 200 Ω source. A pair of dipoles of 2 wavelength separation is fed in parallel from each balun through equal transforming lengths (i.e. and odd number of quarter wavelengths) of balanced transmission line. The proper phasing of the input cables is achieved with a network of power dividers and quadriture and 180 degree hybrids.

5.7 *Midlatitude Mesospheric Scattered Power and Winds*

VHF radars have been used successfully to observe the dynamics of the mesosphere at the equator [*Woodman and Guillen*, 1974; *Rastogi and Bowhill*, 1975a,b; *Countryman and Bowhill*, 1979], at midlatitudes [*Miller et al.*, 1978; *Röttger et al.*, 1979] and at high latitudes [*Balsley and Gage*, 1980]. Although VHF radars can detect incoherently scattered signals from thermal fluctuations in the electron density, most VHF radar observations from below 100 km rely on coherently-scattered signals from irregularities in the refractive index caused by turbulent advection of ionization gradients provided by the continuous increase with altitude of the mixing ratio of electrons between 60 and 90 km. Coherent-scatter radars are able to obtain line-of-sight velocities at these altitudes, and thus are important tools in the study of dynamics of the mesosphere.

A coherent-scatter radar has been operated by the University of Illinois at Urbana since the spring of 1978 [*Miller et al.*, 1978; *Gibbs and Bowhill*, 1979], and data have been collected during daylight hours on a number of days. This section by O. Røyrvik describes the spatial and temporal variations in the

scattered power, and their relation to atmospheric motions of different amplitude and period in the mesosphere.

5.7.1 *Power and correlation time.* VHF scattered power returns from the mesosphere over Urbana vary substantially as a function of both altitude and time. The most prominent feature of the power profile is the consistent occurrence of peaks, or layers, of high scattering cross section. The scattered power in these layers are typically 10 dB above the reference level, but can reach as much as 25 dB above that level (Figure 5.5). The sporadic enhancements in scattered power must represent a local increase in the 3.7-meter-wavelength component of the turbulent spectrum. The tendency of these "whitecaps" to occur in well-defined layers is illustrated by Figure 5.6, which shows hourly 50% and 90% power profiles for four hours. These layers of high scattering cross section may remain stationary in altitude for several hours, as is seen in the peak at 80 km altitude. There may be small but significant vertical shifts in the scattering layer within one hour, as can be seen in Figure 5.5. These apparent vertical motions are generally small, one or two kilometers or less, and the shift may take place within a minute.

It is necessary to be cautious in interpreting these apparent vertical motions of the layer. They certainly cannot be vertical mass motion of the air itself; they may however, correspond to turbulence associated with either

(a) a vertically migrating shear; or
(b) a sloping shear layer which is being carried past the vertical radar beam by a horizontal wind.

Since we cannot easily resolve between these two possibilities, we will refer to the phenomenon as "vertical motion" even though no actual vertical motion may be involved.

Since we know that tidal oscillations and long-period gravity waves produce downward-propagating velocity profiles, it is tempting to explain the vertical motions of the layers on this basis. However, seldom is such a continuous downward propagation seen. Table 5.2 shows the number of days on which different types of behavior of the scattered-power profile were observed. It is seen that continuously descending layers were found on only 16% of the fall 1978 data and none at all in the spring data set.

The best example of a continuously descending scattering layer is seen in Figure 5.7. A strong stable layer was present at the start of the observation at 10:25 CST on December 1, 1978 at the altitude of 81 km. By the end of observation at 16:25 CST this layer, maintaining a constant scattering cross section, had descended to 75 km, leaving behind a non-descending layer peaking at 84 km. Note also that a weaker layer at 63 km maintained its altitude throughout the six-hour period.

Individual scattering layers last from ten minutes to six hours or more (typically four hours) with some short-time variability, as can be seen by comparing the 50% and 90% averages in Figure 5.5 or Figure 5.6. A 15-dB change in scattered power within five minutes is observed in Figure 5.6 around 8:30 CST in the 80 km altitude region, a good illustration of the growth of

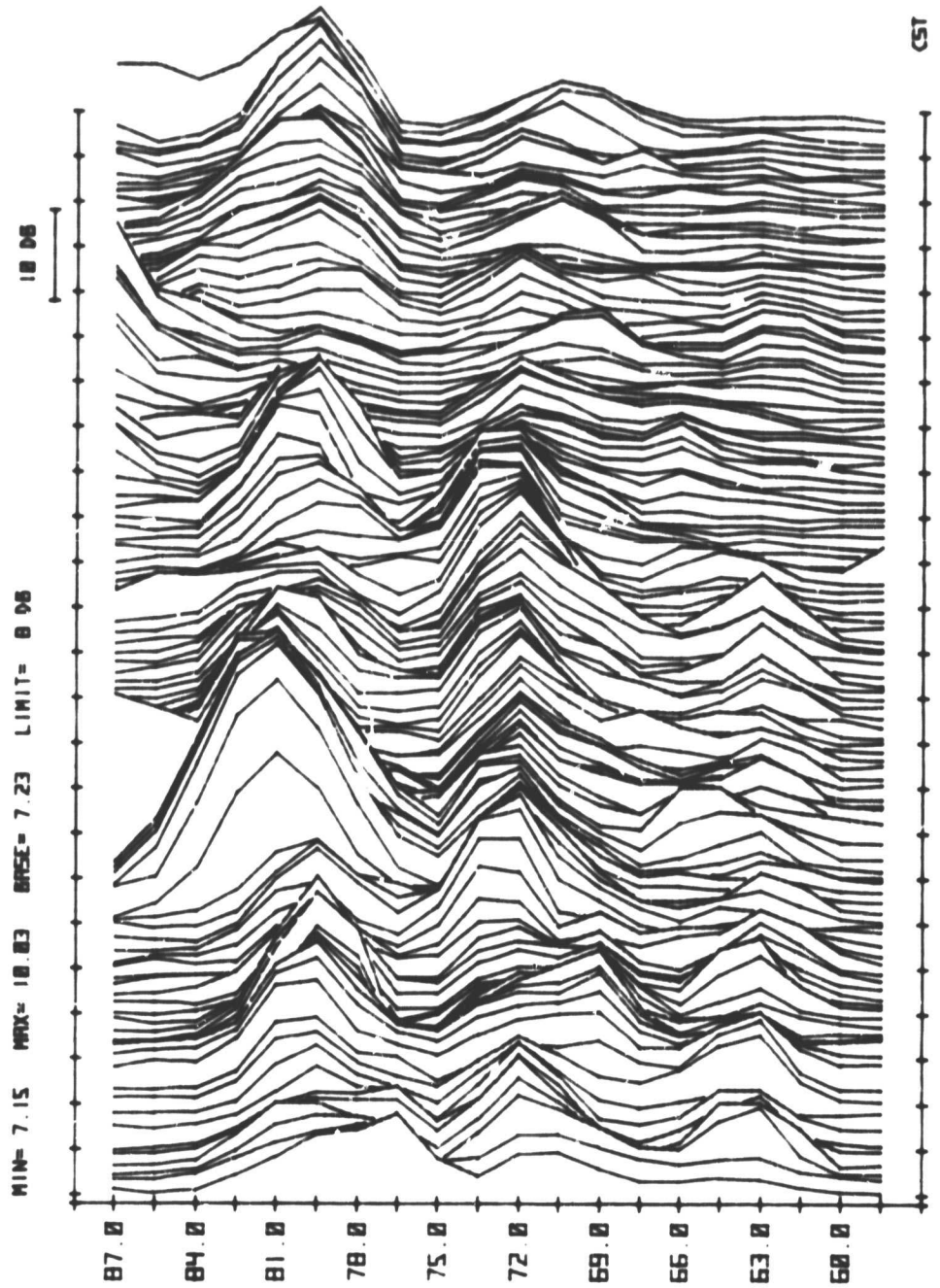

Figure 5.5 Minute-by-minute scattered power profiles between 800 and 1000 CST on April 11, 1978.

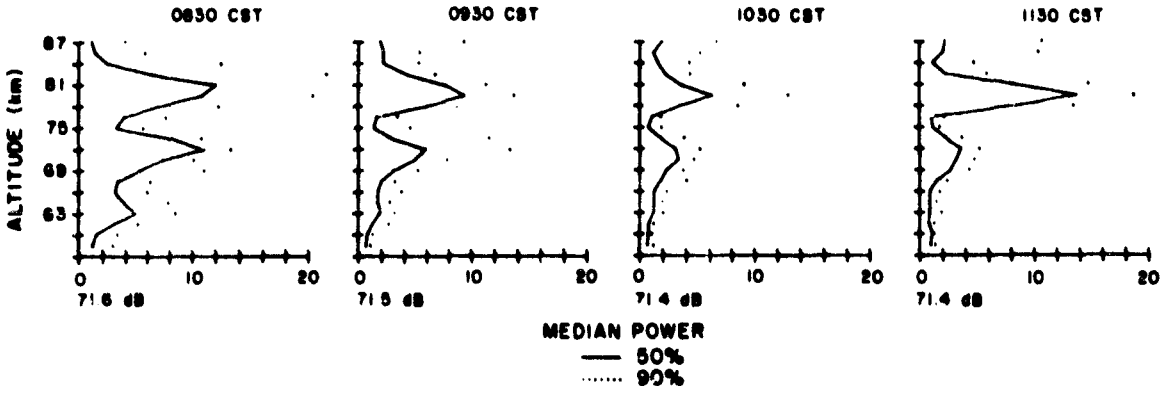

Figure 5.6 Hourly median scattered power profiles for four hours between 800 and 1200 CST on April 11, 1978.

Table 5.2 Number of days on which a particular scattering-layer configuration occurred at least once.

	No layer lasting more than 30 min.	Layer; moving less than 3 km vertically	Layer moving more than 3 km vertically, but with no consistent direction.	Layer descending continuously, for at least 2 hours.
Spring 1978	19% (7)	57% (21)	24% (9)	0% (0)
Fall 1978	20% (8)	27% (11)	37% (15)	16% (7)
Total	20%	4%	30%	8%

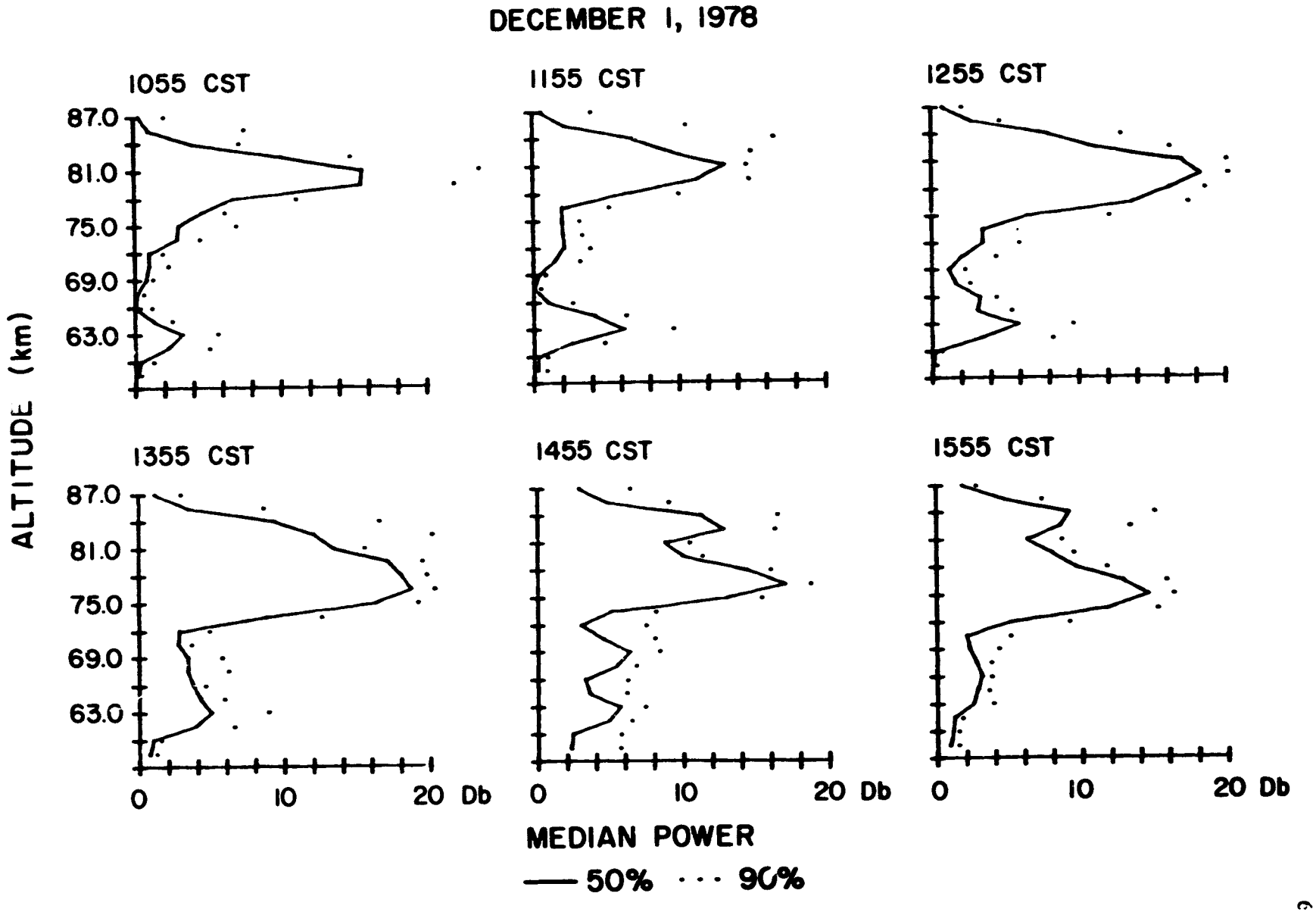

Figure 5.7 Hourly median scattered power profiles 1025 and 1625 CST on December 1, 1978.

a whitecap. The lifetime of a whitecap is of the order of tens of minutes, suggesting that energy from internal gravity waves plays a role in generating the turbulence. Substantial hour-to-hour changes in the median power are also evident.

Although enhancements in the scattering cross section generally occur in well-defined layers, there are times where these layers are absent and continuously enhanced scattering occurs through most of the mesosphere. One example of this is shown in Figure 5.8 between 10:15 and 12:15 CST on April 13, 1978. It is likely that this broad distribution of scattered power is due to continuously breaking gravity waves generating turbulence over an extended region of the mesosphere.

The present pulse width of the Urbana radar does not allow good determination of the vertical extent of most stable scattering layers, but the thickness is often less than the vertical resolution of approximately 3 km.

Estimates of the correlation time of the scattered signal have been found by integrating the autocorrelation function. It appears that the correlation time varies with height as seen in Figures 5.9 and 5.10. A maximum in the correlation time of about 1 sec is seen in these figures between 60 and 70 km. The shape of the correlation time profile (Figure 5.9) compares well with the median half-correlation-time profile found by *Countryman and Bowhill* [1979] in the mesospheric echoes from Jicamarca, Peru. A maximum correlation time of approximately one second is seen in both data sets. The difference at the highest altitudes is due to contamination by the equatorial electrojet in the Jicamarca data, causing zero correlation time. The Urbana profile, on the other hand, levels off around 0.5 second. It may be significant, however, that the Jicamarca radar uses a frequency of 50 MHz compared to the 41 MHz of the Urbana radar.

The decrease in correlation time below 65 km, seen in both data sets, is probably due to strong photochemical relaxation of the ionization, which limits the lifetime of the irregularities. Below 63 km, this relaxation time becomes less than one second and thus affects the observed correlation time [*Hill and Bowhill*, 1976]. Above the peak in the correlation time at about 68 km, the decrease in correlation time with increasing altitude may be partly due to divergence of the radar beam. A larger scattering volume has less coherence in the line-of-sight velocity across the beam, thus broadening the spectrum and giving a shorter correlation time. It also follows that any broadening of the antenna pattern will shorten the correlation time at each altitude unless some limit is reached.

An experiment was made to shed further light upon the correlation time variation. Three sections of the existing antenna were fed slightly out of phase, thus defocusing the antenna pattern. The curve marked "Wide Beam Antenna" in Figure 5.9 shows the height profile of the resulting correlation time; it has decreased markedly and has become constant with altitude. This suggests that the antenna beam has been broadened enough at all altitudes to give a scattering volume larger than the outer scale of the turbulence, thus

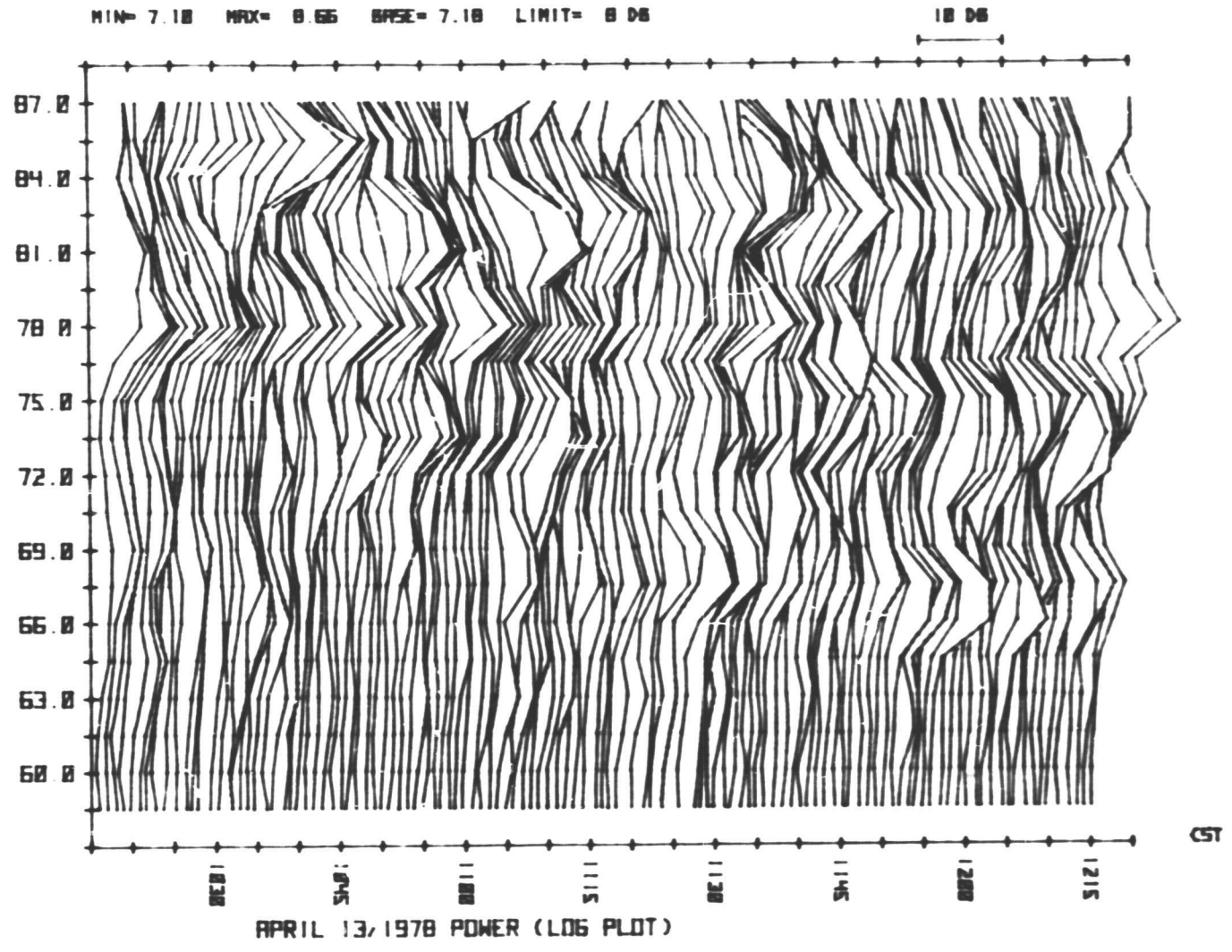

Figure 5.8 Minute-by-minute scattered power profiles 1015 and 1215 CST on April 13, 1978.

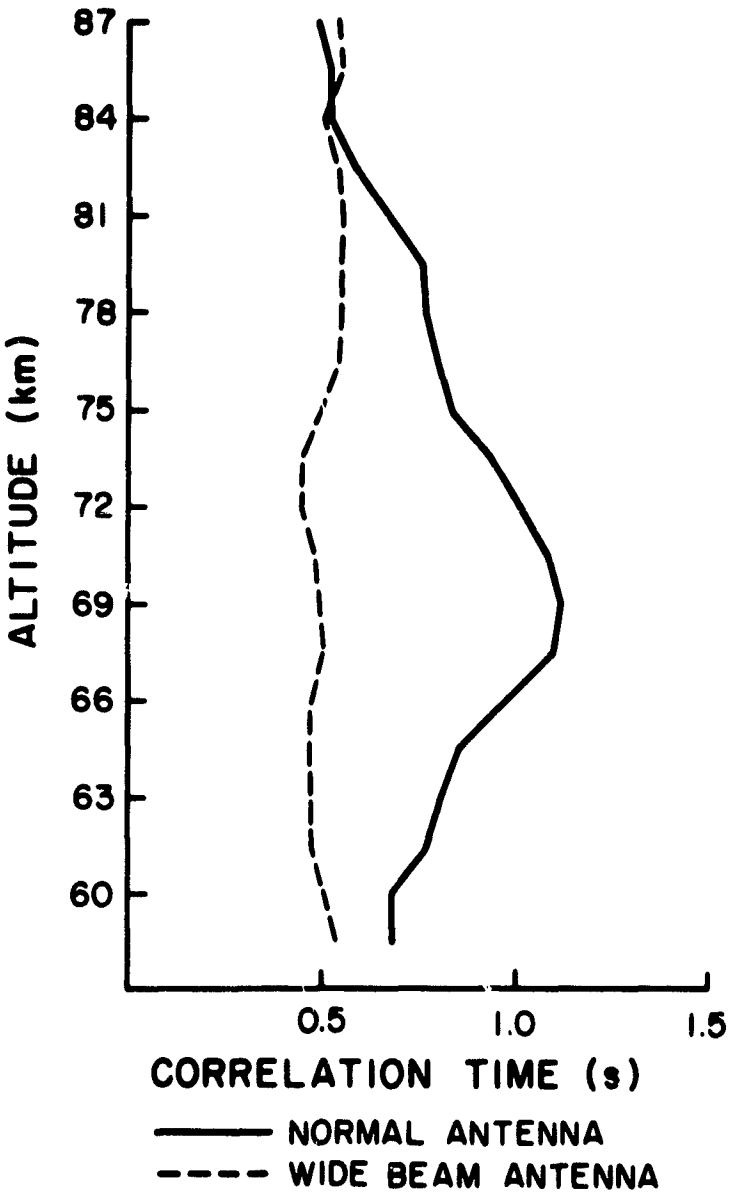

Figure 5.9 Profiles of the correlation time of the scattered power from the normal Urbana antenna and the modified wide beam antenna.

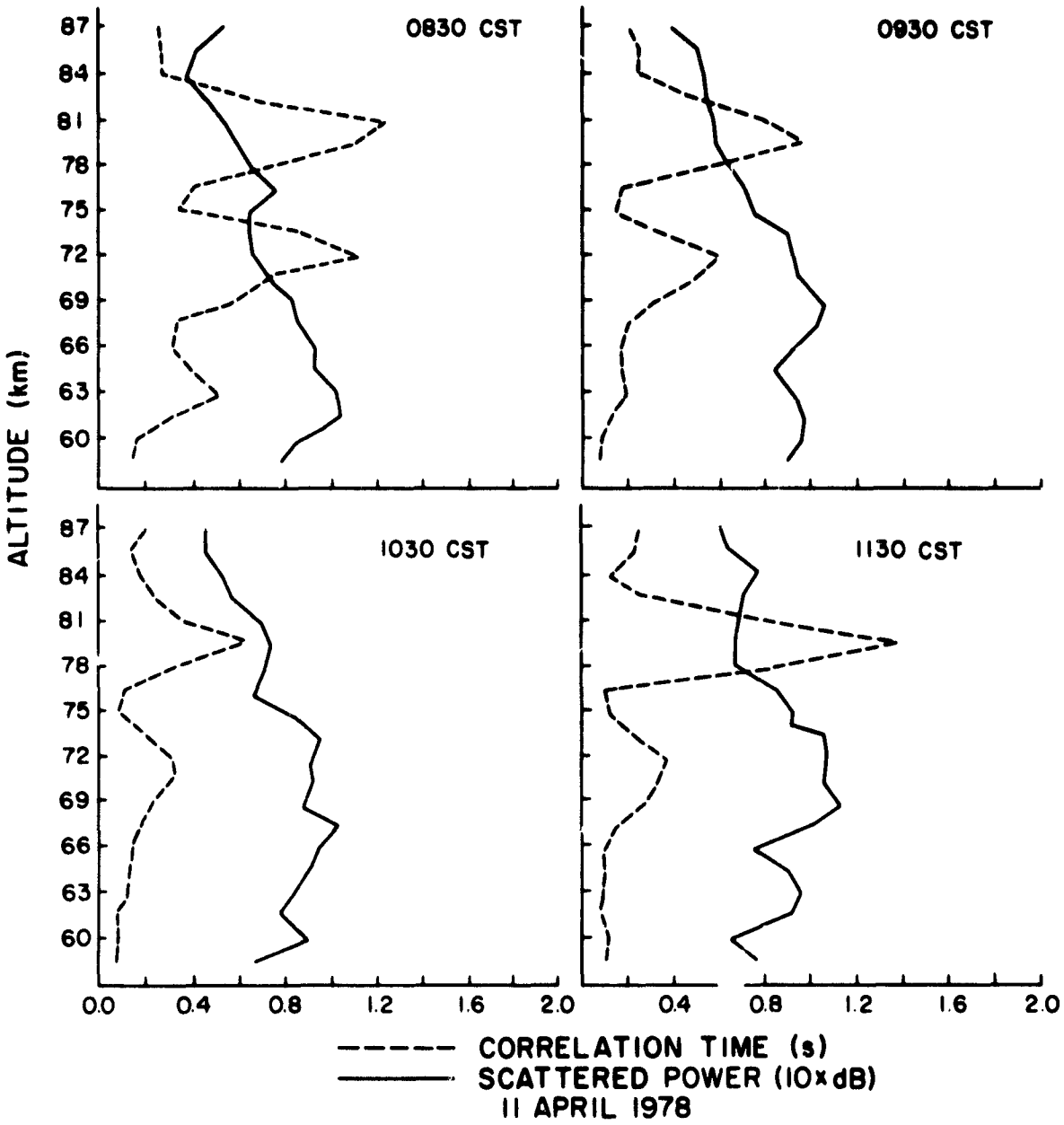

Figure 5.10 Hourly median scattered power profiles and corresponding hourly mean correlation time between 800 and 1200 CST on April 11, 1978.

including the whole velocity spectrum.

The correlation time does not seem to depend on whether a layer of increased scattered power is present (Figure 5.10). Particularly around 09:30 CST is the correlation time decreasing continuously through the two peaks at 72 km and 81 km. This contrasts with the observations of *Rastogi and Bowhill* [1975], *Harper and Woodman* [1977] and *Countryman and Bowhill* [1979] at Jicamarca who showed that longer correlation times are associated with higher scattered signal power at 70 km, where as at 77.5 km the association is reversed.

Median scattered power profiles obtained between 07:00 and 17:00 CST are shown in Figure 5.11 for the spring (April-May 1978) and the fall (August-December 1978) seasons amounting to 97 and 58 hours, respectively. The peaks in the profiles are close to 76 km in both seasons. Most data used in this study were obtained between the altitude of 58.5 km and 87 km; however, some data from May 1978 show that very little coherent scatter is present above 95 km.

Figure 5.12 shows the median and 90% relative power profiles for all 1978 data. The 90% profile peaks at an altitude of 83 km compared with 76 km for the median. This probably reflects the increased incidence of whitecaps at altitudes above 76 km since the 90% power level is more sensitive to these transient disturbances than is the median. It is also interesting to note that the discrete scattering layers noted above are not sufficiently consistent in altitude from day to day to appear on the cumulative profiles of Figure 5.12.

5.7.2 *Velocities.* Unlike long-period atmospheric waves, the air motions caused by short-period gravity waves have a substantial vertical component. Thus the line-of-sight velocity observed by the Urbana radar is dominated by oscillations with periods of the order of ten minutes. However, on the scale of hours, it is known that the horizontal motions are two orders of magnitude larger than the vertical motions, so one may reasonably assume that the hourly average air motion observed is primarily due to the line-of-sight component of the horizontal velocity appearing in the slightly off-vertical antenna beam. We are therefore able to study both short-period gravity waves in the form of vertical velocity oscillations and long-period gravity waves.

A complete study of waves in the upper atmosphere requires knowledge of both the vertical and horizontal wavelength as well as the period. The Urbana radar configuration does not allow observations of the horizontal wavelength so our conclusions are somewhat limited.

A few typical examples of short-period gravity waves are presented in this section. Figure 5.13 contains velocity time series for the period 8:00-10:00 CST on April 11, 1978. The corresponding power profiles have been shown in Figure 5.5. Note that the phase of the waves present throughout the period is a step function of a function of altitude, where the changes in phase correspond to minimums in the power profile in Figure 5.5. This is the result of oversampling of the signals scattered form a layered profile of turbulence.

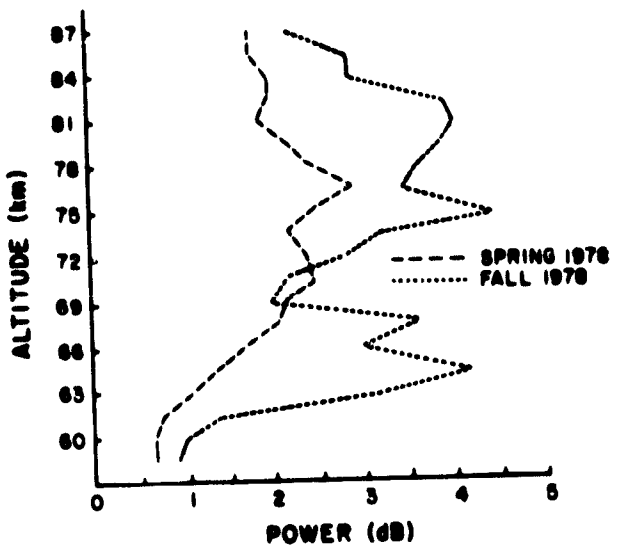

Figure 5.11 Seasonal median power profiles for spring and fall 1978.

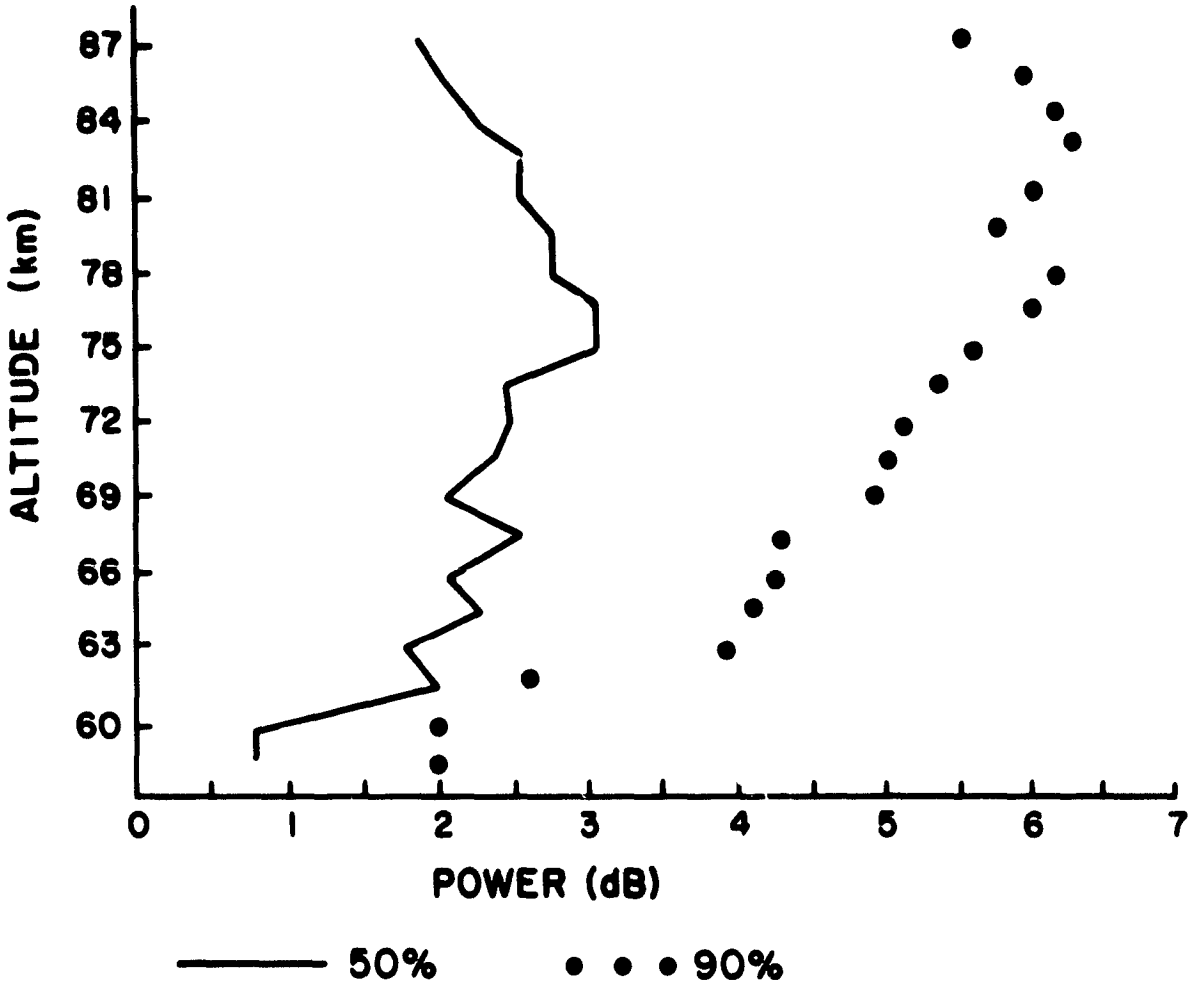

Figure 5.12 Median power (50%) and 90% relative power profiles for the 1978 data.

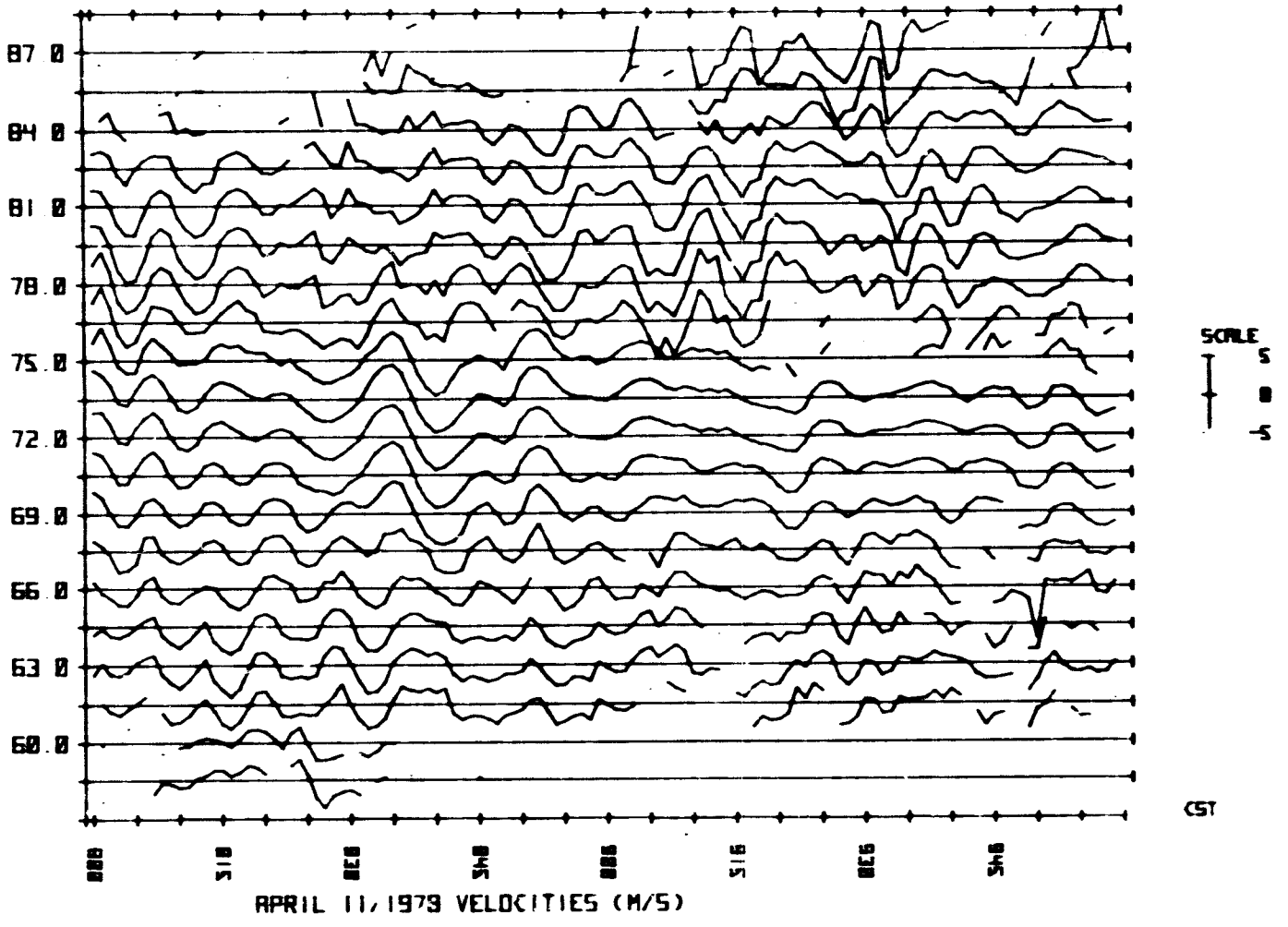

Figure 5.13 Minute-by-minute line-of-sight velocity between 800 and 1000 CST on April 11, 1978.

Apart from this effect, it is clear that the velocity oscillations show upward phase propagation throughout all altitude regions between 8:00 CST and 8:18 CST. This corresponds to downward propagating energy. The vertical wavelength is of the order of several tens of kilometers. At 8:18 CST the waves in the altitude region between 78 and 84 km is replaced by nonperiodic motions lasting until 8:43 CST. Comparing with the power profiles in Figure 5.5, this corresponds to the time of the large peak in the scattered power, interpreted as the breaking of the short-period gravity waves at a pre-existing scattering layer creating additional turbulence. This phenomenon is quite frequent in the data. At lower altitudes during this time, there is a change from upward phase propagation to downward phase propagation involving a transient change of period around the 72 km level. After 08:43 CST there are waves with downward propagating phase throughout the whole altitude range from 61.5 to 84 km, representing upward propagating energy. The vertical wavelength is of the order of several tens of kilometers.

Another common phenomenon is seen around 09:30 CST where the wave field above and below 75 km is completely unrelated. This could possibly be due to ducting of gravity waves between a layer at 75 km and one at a higher altitude.

Figure 5.14 shows the velocities from April 13, 1978 between 1017 and 1217 CST, corresponding to the scattered power shown in Figure 5.8, the scatter being fairly evenly distributed with altitude. The frequency spectrum of the velocity oscillations appears to vary considerably during the 2-hour period, perhaps due to multiple packets of gravity waves propagating through the region of observation. On several occasions, phase reversals with altitude can be seen, the best example being between 79.5 and 91 km at 11:10 CST. This probably represents a standing-wave pattern caused by gravity-wave reflection at some level above 84 km. However, the short duration (approximately 15 minutes) of the standing-wave pattern indicates a short-lived reflecting layer.

Hourly averages of the horizontal wind for the same time period as Figure 5.5 are shown in Figure 5.15, together with the standard deviation of the line-of-sight velocity and its half-correlation time. Comparing the horizontal velocity profiles with the corresponding power profiles in Figures 5.5 and 5.6, we find that the peaks in the power profile occur at altitudes of local maxima in the S-E horizontal wind profile, or to zero vertical gradient in the S-E horizontal wind.

It is, however, premature to draw conclusions about the relationship between wind shear and scattered power on the basis of the present data, for two reasons. First, nothing is known from the present data about the N-E component of the wind. Second, there may be a tendency for the wind profiles of Figure 5.15 to be dominated by a relatively small number of discrete scattering layers having some systematic relationship to the actual wind-shear profile, resulting in a distorted apparent wind profile. This point clearly needs further investigation.

The spring and fall averages of the standard deviation of the vertical

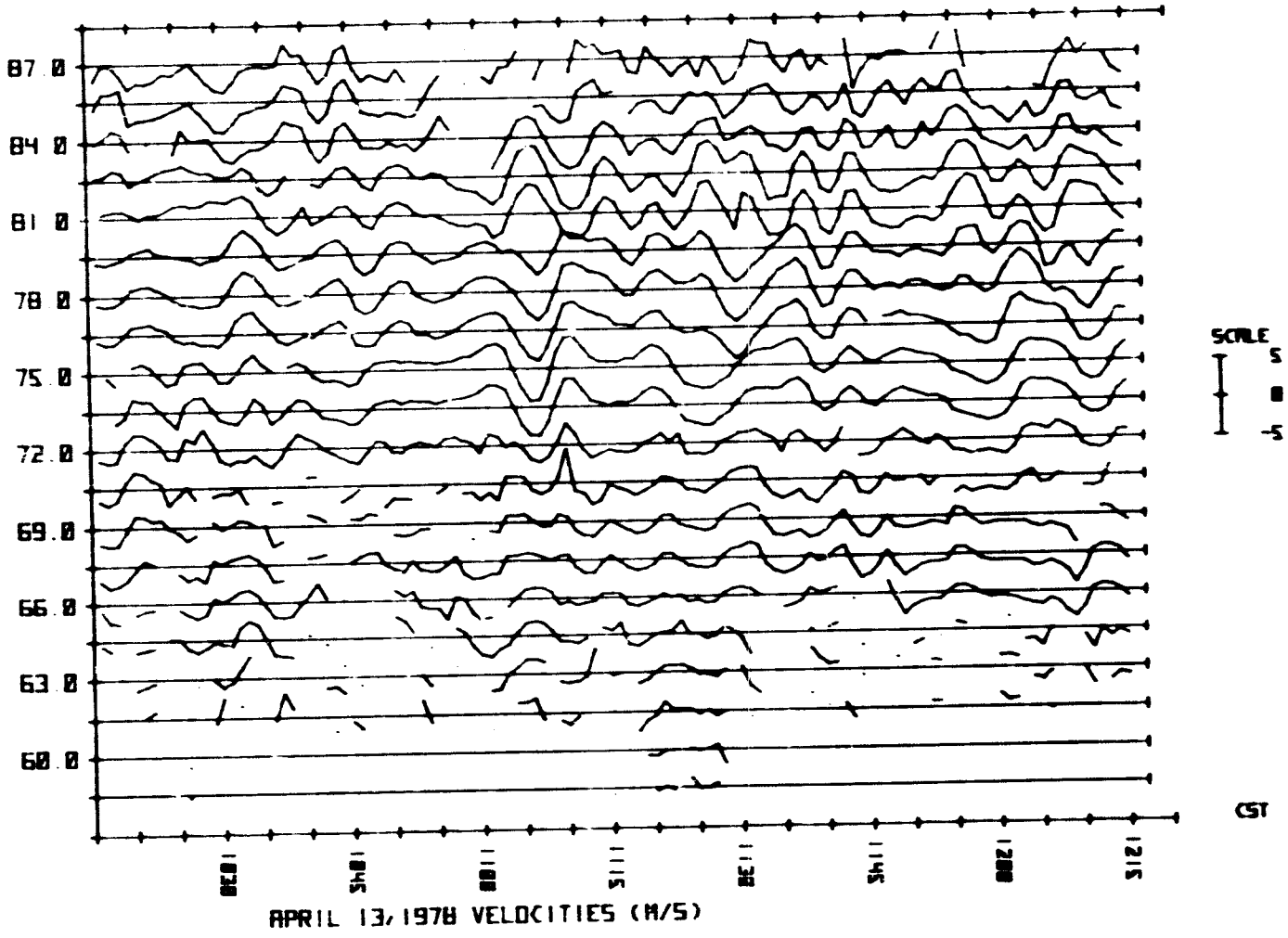

Figure 5.14 Minute-by-minute line-of-sight velocity between 1015 and 1212 CST on April 13, 1978.

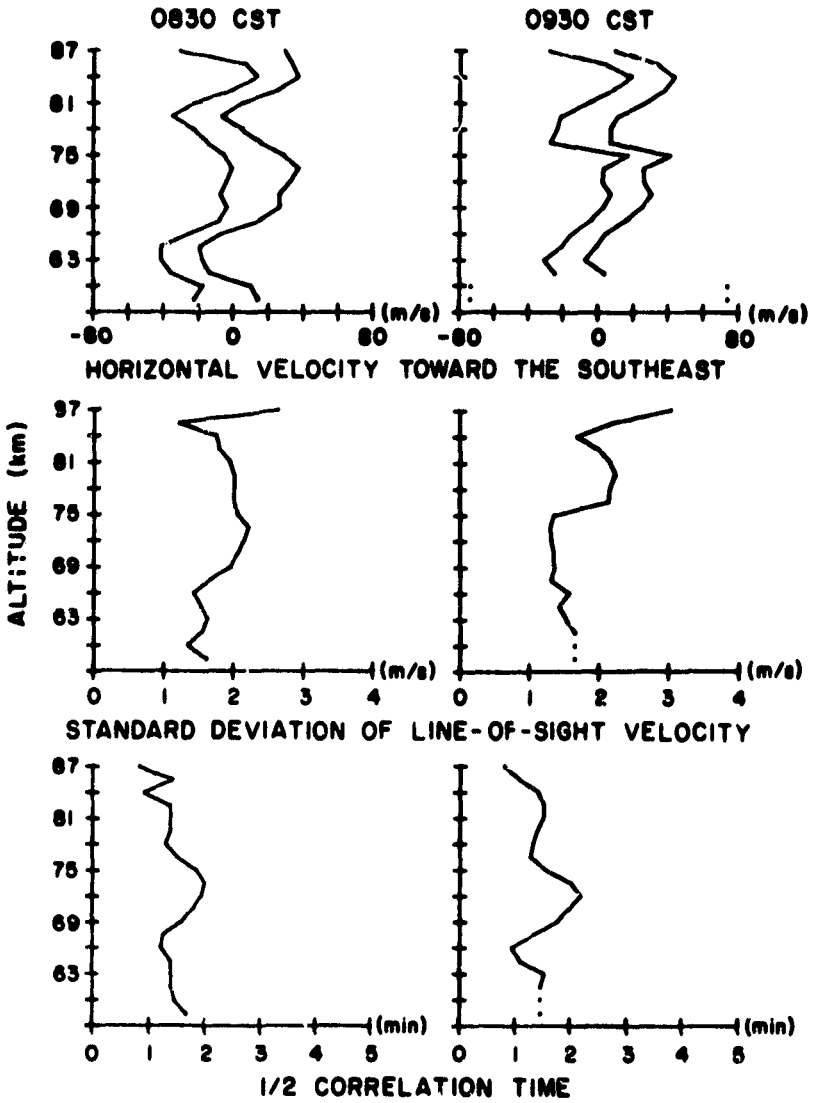

Figure 5.15 Calculated hourly means of the horizontal velocity, the standard deviation and the half correlation time of the line-of-sight velocity profiles between 800 and 1000 CST on April 11, 1978. The two curves in the horizontal velocity profile represents the standard deviation profiles.

velocity are shown in Figure 5.16. Note the enhanced wave amplitude below 63 km for the fall data and below 67.5 km for the spring data. Figure 5.17 from *Bowman and Thomas* [1976], shows a local maximum in the Brunt-Vaisala period around 65 km. This barrier in the Brunt-Vaisala frequency acts as a reflector of short-period gravity waves creating a standing-wave pattern below 65 km. The increase in amplitude seen in Figure 5.16 around 60 km may correspond to the top of this standing-wave pattern, the Brunt-Vaisala barrier being located at a higher altitude in the spring than in the fall. It is emphasized however, that there are cases (such as that in Figure 5.15) where there is no increase below 60 km.

Above 60 km the wave amplitude in Figure 5.10 is essentially constant with altitude both for the spring and the fall data. This suggests a continuous absorption or reflection of wave energy with altitude, since otherwise the conservation of energy with altitude implies a wave amplitude that increases as the -0.5 power of the pressure.

Since the Brunt-Vaisala barrier tends to suppress shorter-period waves, it is intuitively expected that wave spectrum above 65 km should contain more long-period waves than below 65 km. From Figure 5.18, it is seen that the correlation time increases above 63 km in the spring and above 60 km in the fall probably corresponding to the lower edge of the Brunt-Vaisala barrier. Below 60 km the correlation time indicates a wave period of about 4.5 to 5 minutes, close to the Brunt-Vaisala period. Between 66 and 80 km the average wave period is constant at around 8 minutes in the spring and about 12 minutes in the fall. The reason for this difference in wave periods is unclear, but could be due to variations in the strength of the Brunt-Vaisala barrier. Above about 80 km the correlation time starts falling off, indicating a cascading of energy from long-period gravity waves in to short-period gravity waves and turbulence above 80 km. This interpretation is consistent with the data of Figure 5.13 showing breaking waves or whitecaps above 78 km. At 87 km both the spring and the fall correlation times again approach a value corresponding to the local Brunt-Vaisala period of about 5 minutes.

5.7.3 *Discussion and conclusion.* Scattered power in the mesosphere tends to occur in persistent layers with a separation of a few km, as seen in Figure 5.5. It is tempting to assume that this separation is related to the vertical wavelength of tides or long-period gravity waves. However, the nearly constant altitude of most of these scattering layers then requires a standing-wave pattern, caused by wave reflection at an altitude above 90 km. Reflection of tidal components has been reported by several groups [*Fellows et al.*, 1975; *Tsuda et al.*, 1979]. Vertical wavelengths as deduced from the power profiles range from 12 to 36 km; or 6 or 18 km if there is only one layer per wavelength.

Scattering profiles such as Figure 5.7 can be interpreted as a combination of a standing and a descending tidal component resulting from partial reflection of a tidal wave.

Since turbulence is related to velocity gradients we expect tides with short vertical wavelengths to be the dominant cause, since long vertical wave-

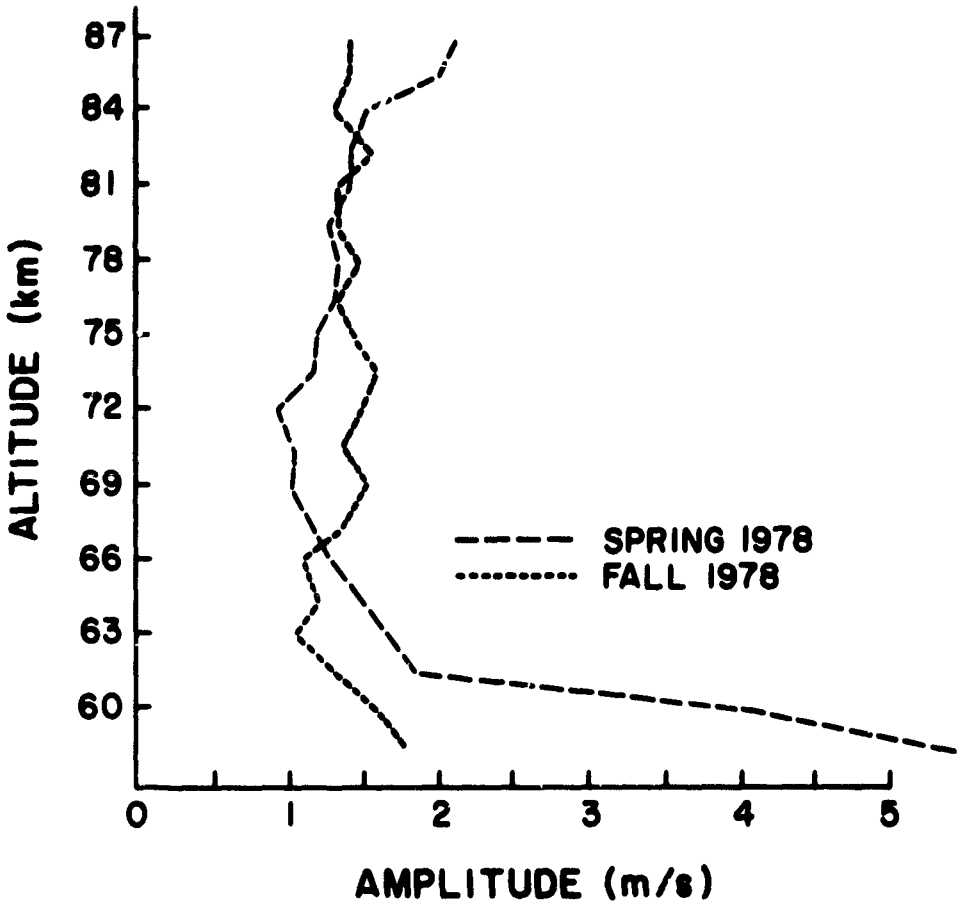

Figure 5.16 Seasonal averaged profiles for the standard deviation of the line-of-sight velocity for spring and fall 1978.

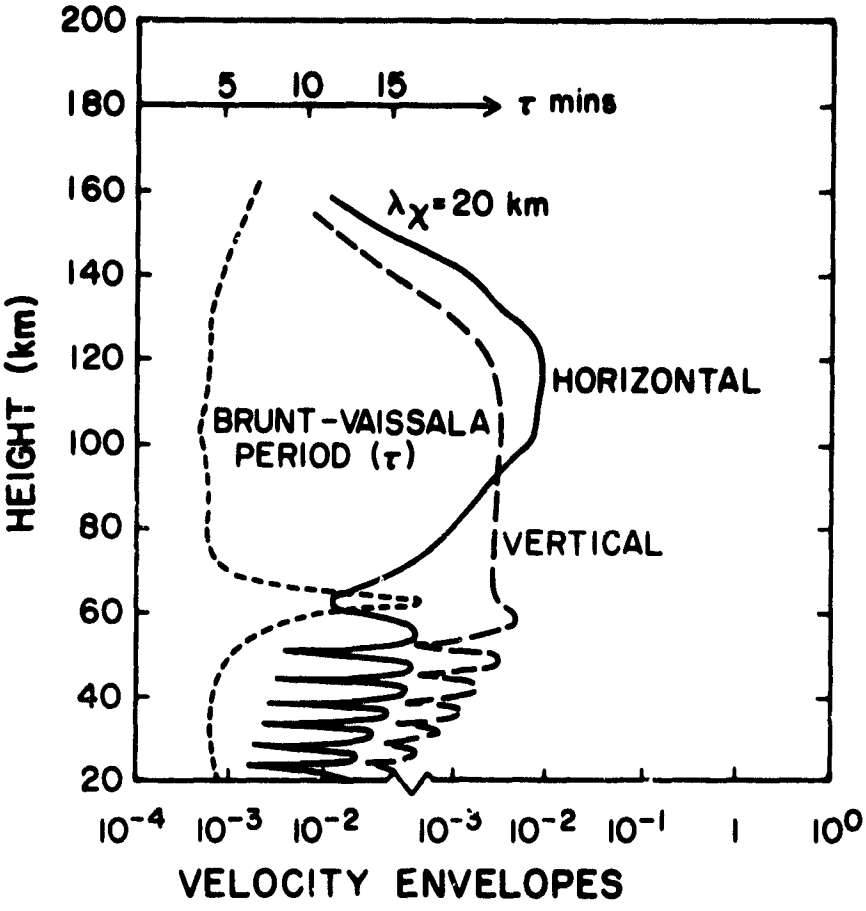

Figure 5.17 Variations of the horizontal and vertical velocity envelopes as a function of altitude for a wave period of 10 min and for a horizontal wavelength λ_x of 20 [*Beaman and Thomas*, 1976].

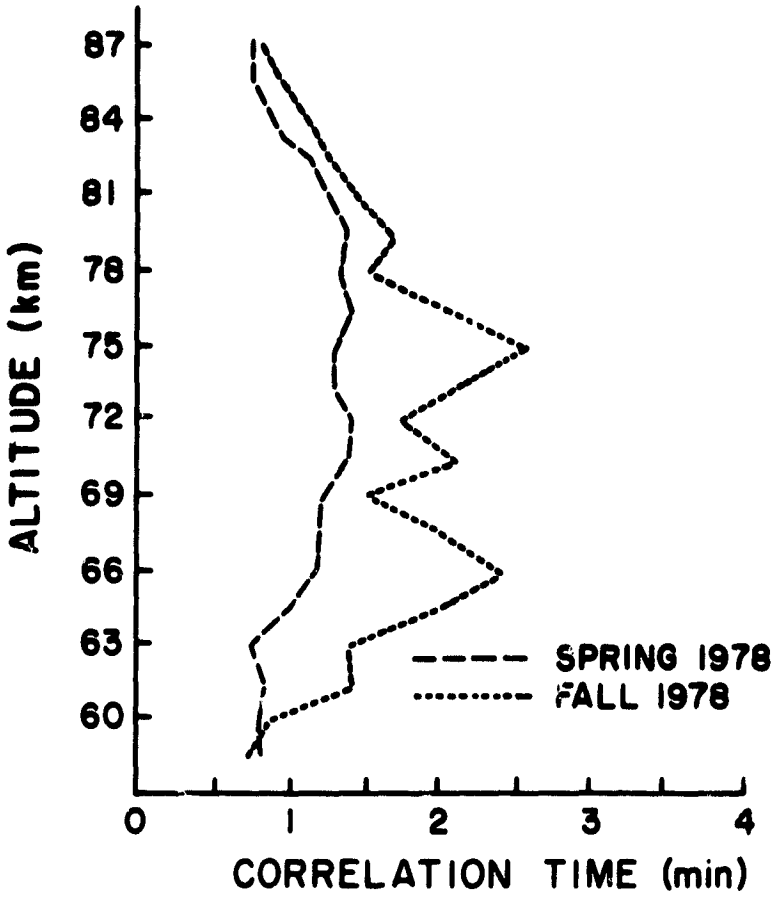

Figure 5.18 Seasonal correlation time profiles for the line-of-sight velocity for spring and fall 1978.

lengths give very small gradients even if the amplitude is large. Both *Fellous et al.* [1975] and *Tsuda et al.* [1979] have shown that observed diurnal tide has much shorter vertical wavelength than the observed semi-diurnal tide. Assuming that the descending tide in Figure 5.7 is diurnal, we have a vertical wavelength of 24 km which corresponds well with the expected vertical wavelength of the S_{11} diurnal mode at the altitude of 80 km.

The standing-wave pattern in Figure 5.6 is most likely due to a diurnal or semidiurnal tide with vertical wavelength of 18 km. This compares well with the south-east component of the horizontal wind in Figure 5.15 which shows a dominant vertical wavelength of 18 km.

Although stable layers usually dominate the scattered-power profile, there are still substantial variations in amplitude and scattering height (Figure 5.5). Since the short-term variations in scattered power have periods (about 10 min) comparable to those of the velocity fluctuations, we believe that these short-term variations are caused by gravity wave modifications of the wind profile, thus varying the amplitude and altitude of maximum shear, and hence the turbulence. However, we have been unable as yet to establish a detailed relationship between wave velocity and scattered power.

The amount of scattered power depends also on the background electron-density gradient, which is advected by the turbulent velocity field, subject to the effects of relaxation [*Hill and Bowhill*, 1975]. The mutual interaction between these effects is quite complex, and the electron-density gradient is quite variable from day to day. However, the averaged electron-density-gradient profile (Figure 5.19, a component from *Mechtly et al.* [1972]) increases with altitude except for local maxima at the bottom ledge of the D and E layers respectively. In addition, the photochemical relaxation rate is higher at lower altitudes, thus favoring greater scattering from higher altitudes.

Below 70 km the decrease in turbulent energy with increasing altitude, at the wave number of the Urbana radar, in linear [*Rastogi and Bowhill*, 1976b]. However, the energy-spectrum of the turbulence falls off exponentially as a function of altitude above approximately 70 km. Furthermore, above 80 km the e-folding distance of the exponential decay decreases, indicating an even greater decrease of turbulence with altitude. Thus, we believe the decrease in observed scattered power with altitude to be due to the sharp decrease in turbulent energy overriding the increase in electron-density gradient above about 70 km.

We have seen that vertical wavelength of short-period gravity waves is large, 30 km or more, for the gravity waves with periods around 10 min. and that the averaged vertical wave-velocity is more or less constant above 65 km. This agrees well with computation by *Bowman and Thomas* [1976] who found that the vertical gravity wave motion reaches a maximum around 60 km whereas the horizontal wave motion has maximum at 85 km. Thus, we conclude that the observations of the gravity wave profile confirms the existence of the Brunt-Vaisala barrier between 60 and 65 km.

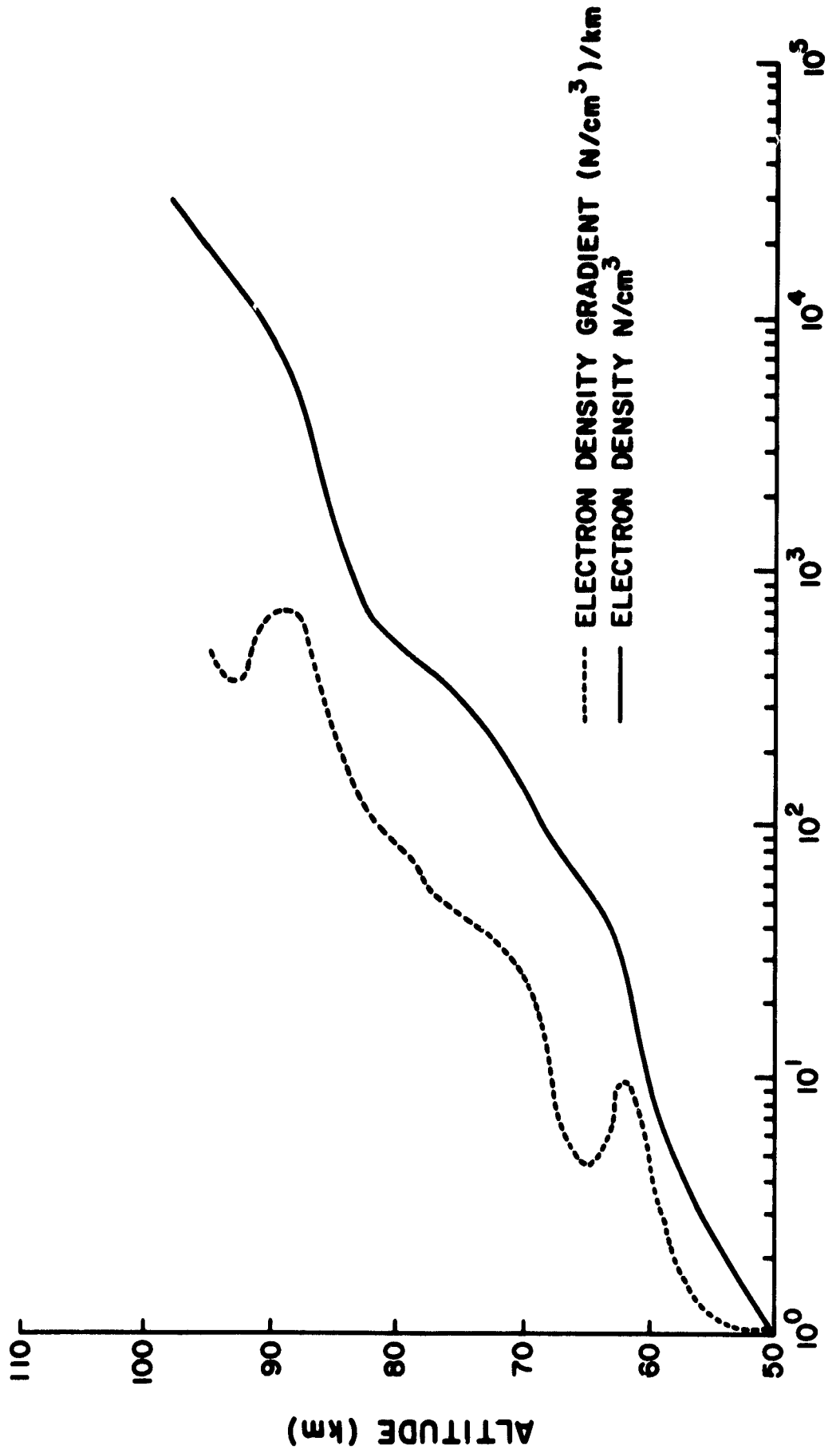

Figure 5.19 Profiles of mean electron density and electron density gradient in the mesosphere.

In summary, the data suggests that the VHF scattered power profile from the mesosphere over Urbana depends on the existence of short-vertical-wavelength tidal components to generate turbulence. In addition, short-period altitude and amplitude variations are believed to be due to gravity wave interacting with the tidal components. These short-period gravity-wave profiles show a variation that is consistent with theoretical predictions of *Bowman and Thomas* [1976].

REFERENCES

Balsley, B. B. and K. S. Gage [1980], The MST radar technique: Potential for middle atmospheric studies, *Pure & Appl. Geophys., 118,* 452-493.

Bowman, M. R. and L. Thomas [1976], The numerical calculation of wave-fields for gravity waves propagating in an inhomogeneous atmosphere, *Planet. Space Sci., 24,* 1199-1205.

Countryman, I. D. and S. A. Bowhill [1979], Wind and wave observations in the mesosphere using coherent-scatter radar, *Aeron. Rep. No. 89,* Aeron. Lab., Dep. Elec. Eng., Univ. Ill., Urbana-Champaign.

Edwards, B., (Editor) [1979], Research in Aeronomy, October 1, 1978 - March 31, 1979, *Prog. Rep. 79-1,* Aeron. Lab., Dep. Elec. Eng., Univ. Ill., Urbana-Champaign.

Edwards, B., (Editor) [1980], Research in Aeronomy, October 1, 1979 - March 31, 1980, *Prog. Rep. 80-1,* Aeron. Lab., Dep. Elec. Eng., Univ. Ill., Urbana-Champaign.

Fellous, J. L., R. Bernard, M. Glass, M. Massebeuf and A. Spizzichino [1975], A study of the variations of atmospheric tides in the meteor zone, *J. Atmos. Terr. Phys., 37,* 1511-1524,

Gibbs, K. P. and S. A. Bowhill [1979], The Urbana coherent-scatter radar: Synthesis and first results, *Aeron. Rep. No. 90,* Aeron. Lab., Dep. Elec. Eng., Univ. Ill., Urbana-Champaign.

Harper, R. M. and R. F. Woodman [1977], Preliminary multiheight radar observations of waves and winds in the mesosphere over Jicamarca, *J. Atmos. Terr. Phys., 39,* 959-963.

Hill, R. J. and S. A. Bowhill [1976], Small-scale fluctuations in D-region ionization due to hydrodynamic turbulence, *Aeron. Rep. No. 76,* Aeron. Lab., Dep. Elec. Eng., Univ. Ill., Urbana-Champaign.

Mechtly, E. A., S. A. Bowhill and L. G. Smith [1972], Changes of lower ionosphere electron concentrations with solar activity, *J. Atmos. Terr. Phys., 34,* 1899-1907.

Miller, K. L., S. A. Bowhill, K. P. Gibbs and I. D. Countryman [1978], First measurements of mesospheric vertical velocities by VHF radar at temperate latitudes, *Geophys. Res. Lett., 5,* 939-942.

Rastogi, P. K. and S. A. Bowhill [1975], Remote sensing of the mesosphere using the Jicamarca incoherent-scatter radar, *Aeron. Rep. No. 68*, Aeron. Lab., Dep. Elec. Eng., Univ. Ill., Urbana-Champaign.

Rastogi, P. K. and S. A. Bowhill [1976a], Gravity waves in the equatorial mesosphere, *J. Atmos. Terr. Phys.*, *38*, 51-60.

Rastogi, P. K. and S. A. Bowhill [1976b], Scattering of radio waves from the mesosphere-2. Evidence for intermittent mesospheric turbulence, *J. Atmos. Terr. Phys.*, *38*, 449-462.

Rottger, F., P. K. Rastogi and F. R. Woodman [1979], High-resolution VHF radar observations of turbulence structures in the mesosphere, *Geophys. Res. Lett.*, *6*, 617.

Woodman, R. F. and A. Guillen [1974], Radar observations of winds and turbulence in the stratosphere and mesosphere, *J. Atmos. Sci.*, *31*, 493-505.

6. LASER RADAR

A laser-radar syst m has been designed and constructed to measure the altitude distribution of atmospheric sodium in the 80- to 100-km altitude region. The system consists of a high-power pulsed dye laser, large aperture receiving telescope, and photon-counting and signal-processing equipment. Coordination of the project has been provided by Prof. C. F. Sechrist, Jr. Also involved are Prof. C. S. Gardner who has been concerned with the receiving system development, and Prof. H. Merkelo of the Quantum Electronics Research Laboratory who has offered assistance in the construction and development of the dye laser. This research is supported in part by the National Science Foundation under grant ATM 79-20726, and in part by the National Aeronautics and Space Administration under grant NGR 14-005-181

6.1 *Two-Dimensional Signal Processing*

Theoretically, the laser pulse width, receiver range gate width, data integration time and sampling interval place the fundamental limits on the spatial and temporal resolution of lidar profiles. However, in practice the resolution of sodium lidar data is usually limited by shot noise. Spatial filtering has been shown to be an effective technique for enhancing the spatial resolution of sodium lidar profiles by reducing shot noise in the photocount data [*Rowlett et al.*, 1978; *Rowlett and Gardner*, 1979]. During this past year J. D. Shelton and C. S. Gardner have developed a two-dimensional signal processing technique which utilizes spatial and temporal filtering to further reduce shot noise and increase profile resolution [*Gardner and Shelton*, 1981; *Mihavics*, 1979]. The 2-D technique has been applied to our sodium lidar data since the fall of 1979 and has revealed some interesting small-scale short-term variations in the layer.

The most critical aspect of the 2-D filtering process is the determination of the appropriate spatial and temporal cutoff frequencies. This is accomplished by examining the spatial and temporal periodograms of the photocount data. First, the average background noise level is subtracted from the raw photocounts comprising each sodium profile. The spatial periodogram of each profile is computed using a fast Fourier transform (FFT) algorithm. Then the periodograms of all the profiles collected during the night are averaged. The average spatial periodogram for the 71 profiles collected on the night of October 28-29, 1979 is plotted in Figure 6.1a. The dashed line is the average shot noise level which is approximately 30 dB below the spectral peak at wave number zero. The dashed curves are one standard deviation above and below the average periodogram. Because of the large number of profiles used to compute the average, the error is quite small. Notice that the average periodogram falls into the shot noise at a wave number near 0.3 km^{-1}.

The temporal periodogram is more difficult to compute and analyze for two reasons. First, temporal variations of the sodium layer at a fixed altitude are usually a very small percentage of the average sodium background. The second difficulty arises from the sharp discontinuities in the temporal data at the beginning and end of the observation period. The sharp discontinuities along with the high average level dominate the temporal periodogram and overshadow spectral componenets due to actual temporal varia-

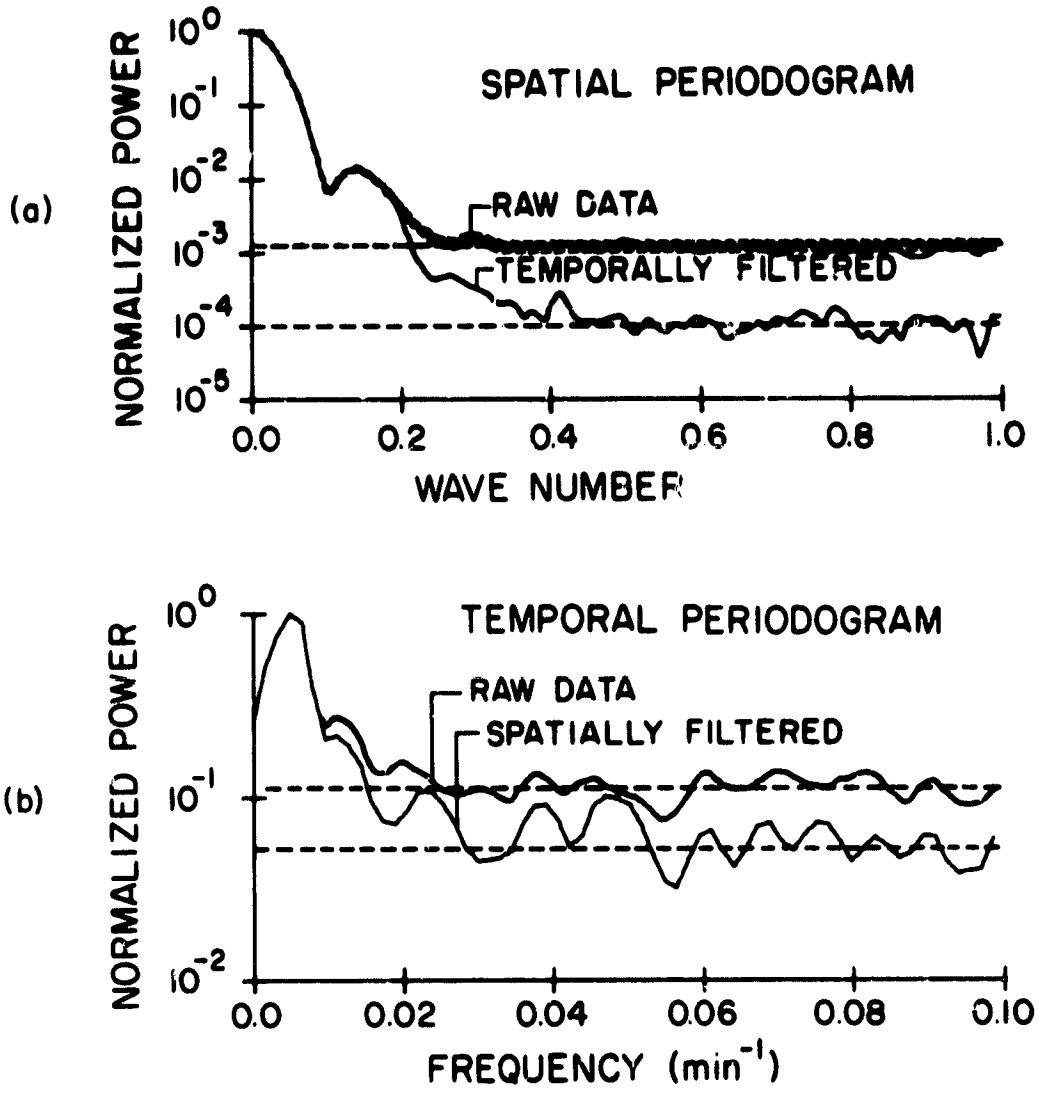

Figure 6.1 Spatial and temporal periodograms of the sodium lidar photocount data collected during the night of October 28-29, 1980.

(a) The cutoff frequency for the temporally filtered data is 0.03 min^{-1}.

(b) The cutoff wave number for the spatially filte.ed data is 0.44 km^{-1}.

tions in the sodium layer. This problem can be ameliorated by subtracting the average sodium background level from each range bin and then multiplying the resulting temporal data by a window function to eliminate the discontinuities at the beginning and end of the observation period. The temporal periodogram for each range bin can then be computed by taking the FFT of the windowed data.

Unfortunately, the periodogram provides a very noisy estimate of the signal spectrum. The noise can be reduced and a more reliable estimate of the spectral features present in the temporal spectrum can be obtained by averaging the periodograms for all range bins in the sodium layer. The dominant spectral features present throughout the layer during the observation period will be retained in the average temporal periodogram. Because we are computing the temporal periodogram for the purpose of choosing an appropriate filter cutoff frequency and are not interested in the detailed spectral structure, the slight distortion introduced by windowing the data and averaging the periodograms is not significant.

The average temporal periodogram for the 71 profiles collected during the night of October 28-29, 1979 is plotted in Figure 6.1b. The peak signal level near temporal frequency 0.003 min^{-1} is approximately 10 dB above the shot noise level indicated by the dashed line. Since the signal falls into the shot noise near the frequency 0.03 min^{-1}, a lowpass filter with a cutoff of 0.03 min^{-1} will be used to process the data. Because the temporal filter is applied directly to the raw photocount data, a finite impulse response filter is required to prevent distortion which could be introduced by the short discontinuities in the data at the beginning and end of the observation period. We have chosen to use a lowpass filter with an impulse response which is identical to the Hamming window function.

Temporal filtering can result in a significant reduction in shot noise. To illustrate, the October 28-29 data were lowpass filtered with a cutoff frequency of 0.03 min^{-1}. Here we define the cutoff frequency as the first zero in the DFT of the Hamming window function. The average spatial periodogram of the temporally filtered data is plotted in Figure 6.1a. By comparing the spatial periodogram of the temporally filtered data with the periodogram of the raw photocount data also plotted in Figure 6.1a, it is clearly seen that temporal filtering has reduced the shot noise level by more than 10 dB. Spectral features which were completely hidden by the shot noise in the raw data are readily observed in temporally filtered data. In a similar manner, spatial filtering can reduce the shot noise level in the temporal periodogram. This is illustrated in Figure 6.1b where the average temporal periodograms are plotted for the raw data and spatially filtered data collected on October 28-29. For this particular data set and choices for the spatial and temporal cutoff frequencies, the approximately 3 dB reduction in the shot noise level due to spatial filtering is not as dramatic as the 10 dB reduction due to temporal filtering.

After the appropriate cutoff frequencies are chosen by examining the spatial and temporal periodograms, the raw sodium profiles are two-dimensionally filtered. The filtered data are then corrected for the inverse square altitude dependence of the lidar signal and the results plotted. In Figure 6.2 are

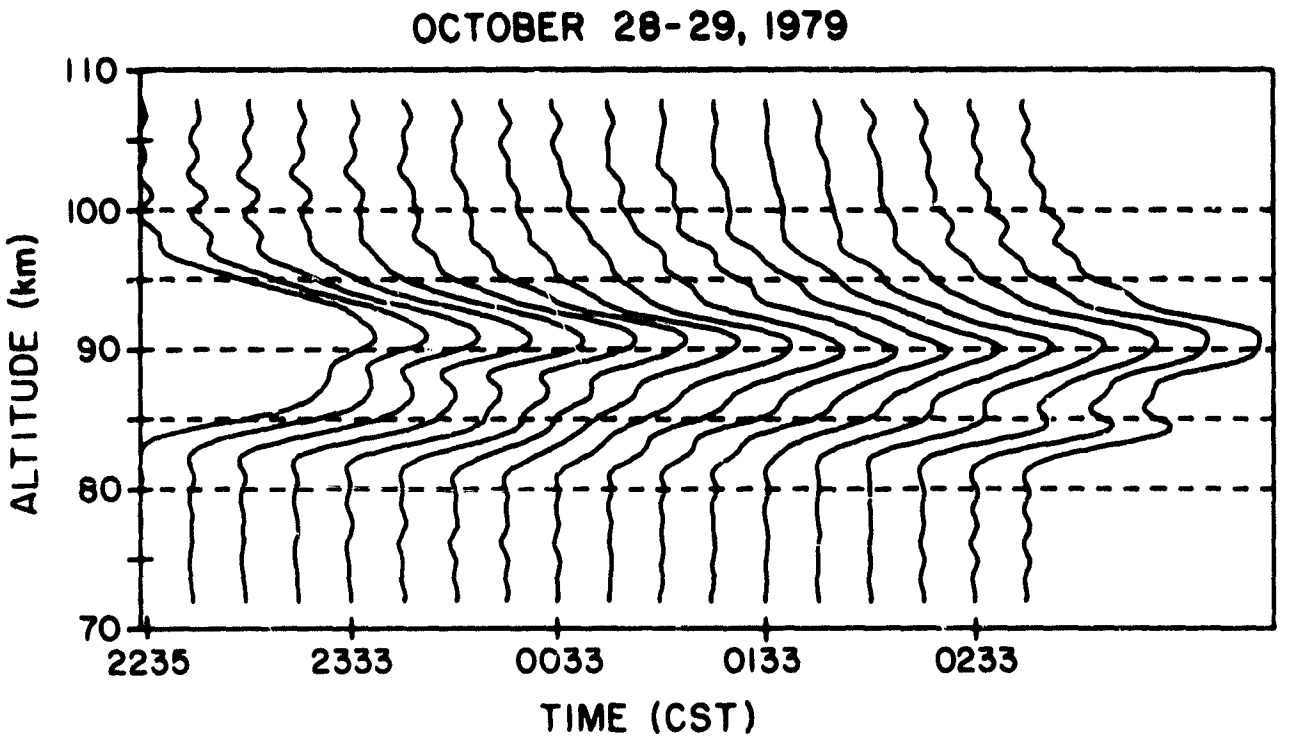

Figure 6.2 Sodium density profiles obtained by 2-D filtering the photocount data collected on October 28-29, 1980. The temporal cutoff frequency is 0.03 min^{-1} and the spatial cutoff wave number is 0.44 km^{-1}; 2-D plot with the horizontal axis representing relative sodium concentration and time.

plotted the 2-D processed sodium profiles for the data collected on October 28-29. The time increment between profiles is 15 minutes. Figure 6.3 is a 3-D plot of this same data. These plots clearly show the propagation of wave-like features through the layer. In the 3-D plot the phase progression of wave is quite apparent on the bottom side of the layer. Notice also the 3-D plot that the sodium concentration near the layer peak at 90 km titude is undulating. The reason for this undulation is evident in igure 6.2. The layer peak moves from an altitude of 91 km at 2233 CST to slightly below 90 km at 0048 CST and then returns to 91 km at 0233 CST.

Rowlett and Gardner [1979], *Mihavics* [1979], and *Gardner and Shelton* [1981] provide more detailed descriptions of the spatial and 2-D filtering techniques.

6.2 *Computer-Model Studies of the Sodium Density Response to Gravity-Wave Perturbations*

The density response of the sodium layer to gravity waves is being investigated theoretically and experimentally by J. D. Shelton. In general, the response of an atmospheric layer to a gravity wave may be determined by examining the equation of continuity. This differential equation indicates that the velocity perturbations associated with a gravity wave will induce density perturbations in the sodium layer. Assuming the diffusion time for sodium is greater than the gravity wave period being considered, the sodium velocity perturbations will be equal to the velocity perturbations in the background atmosphere caused by the passage of this wave. These velocity perturbations may be expressed in terms of atmospheric density variations by utilizing the polarization relations for gravity waves. As a result, the solution of the continuity equation will express the density response of the sodium layer in terms of atmospheric density perturbations caused by gravity waves. A perturbation series solution of the continuity equation may be found. This solution consists of a sum of terms. The first term in this solution describes the linear layer response while the nonlinear portion of the layer response is contained in the higher order terms. In general, the layer response is dominated by the linear term.

Several features are associated with the linear term. These include:

(a) larger density perturbations below the layer peak than above it.

(b) density perturbations with the same temporal frequency and horizontal wave number as the gravity wave.

(c) a point of phase reversal in the linear response occurring slightly above the layer peak.

Near the point of phase reversal, the linear response is small and higher order terms may make significant contributions to the total layer response.

The frequencies of these higher order terms are harmonics of the gravity wave frequency. For example, perturbations associated with the second order term have twice the frequency of the gravity wave. In addition, if

C-2

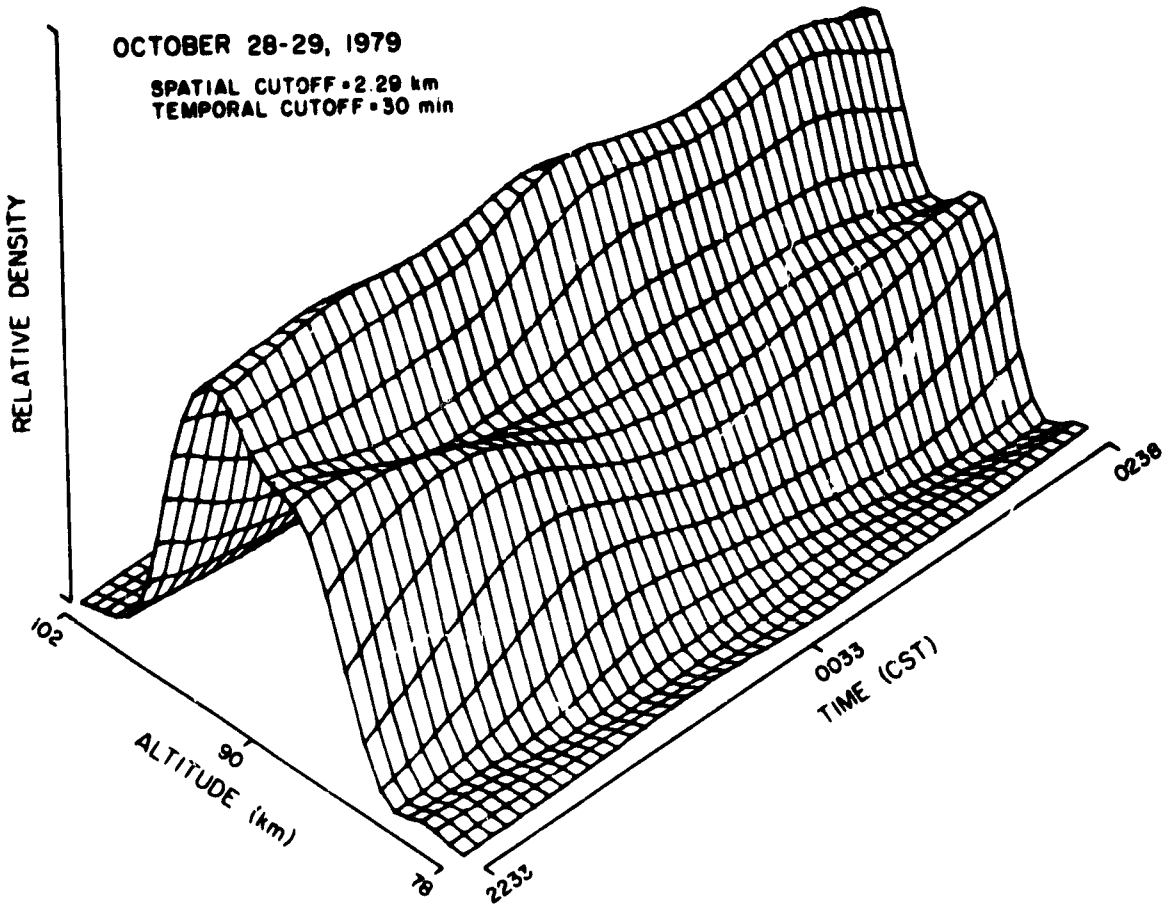

Figure 6.3 Sodium density profiles obtained by 2-D filtering the photocount data collected on October 28-29, 1980. The temporal cutoff frequency is 0.03 min^{-1} and the spatial cutoff wave number is 0.44 km^{-1}; 3-D plot of the same profiles plotted in Figure 6.2.

the perturbations induced in atmospheric density by the gravity wave are small, the magnitude of these high order terms rapidly decreases with increasing order. Figure 6.4 contains a plot of the envelopes of simulated density perturbations associated with the first and second terms of the perturbation series solution and their sum. A Gaussian layer and 5% peak-to-peak variations in atmospheric density have been assumed. It is evident that a double frequency component in the sodium density perturbations should become dominant in the 90.3 to 91.2 km altitude range. This type of behavior has been observed in experimental data. Figure 6.5a contains a plot of the envelope of density variations as well as the average sodium density profile observed on October 28-29, 1979 Figure 6.5 contains a corresponding plot of simulated data assuming the sodium density profile in the absence of gravity waves is the same as the average density profile given in Figure 6.5a. It is seen that good correlation exists between the curves of maximum and minimum density in experimental and simulated data.

6.3 *New Laser for Sodium LIDAR*

A new flashlamp-pumped dye laser for use as the transmitter in the Urbana LIDAR system has recently been obtained. The required specifications for this laser are given below:

	Config. A	Config. B
Center frequency	5890A	5890A
Linewidth, FWHM	0.01A	0.002A
Energy per pulse	50mJ	20mJ

Configuration B is identical to Configuration A with the addition of an electronically tunable etalon to further reduce the linewidth. To have the capability to measure the linewidth of the new laser a spherical mirror scanning interferometer was designed and constructed by R. Nilssen. Testing was done by inserting a "chopper" at the output of a thermally stabilized HeNe alignment laser to simulate a pulsed laser. The purpose of the testing was to determine that the linewidth measurement system performed adequately and to establish that interferometer instabilities were not great enough to interfere with the linewidth measurement. There is little broadening of measured linewidth due to any frequency instabilities. This implies that if this interferometer is used to measure the linewidth of the new laser there will be negligible broadening due to instabilities in the interferometer.

When attempts were made to use this interferometer to measure the linewidth of the new laser it provided to be so difficult to align and the output fringes of such poor quality that meaningful results were not obtained with it. The spherical mirrors were replaced with a pair of flat 85% mirrors. These mirrors had a measured finesse of 8.8 and, for the chosen interferometer spacing this yielded a value of $\Delta\nu_{min}$ of 330 MHz. The output obtained using

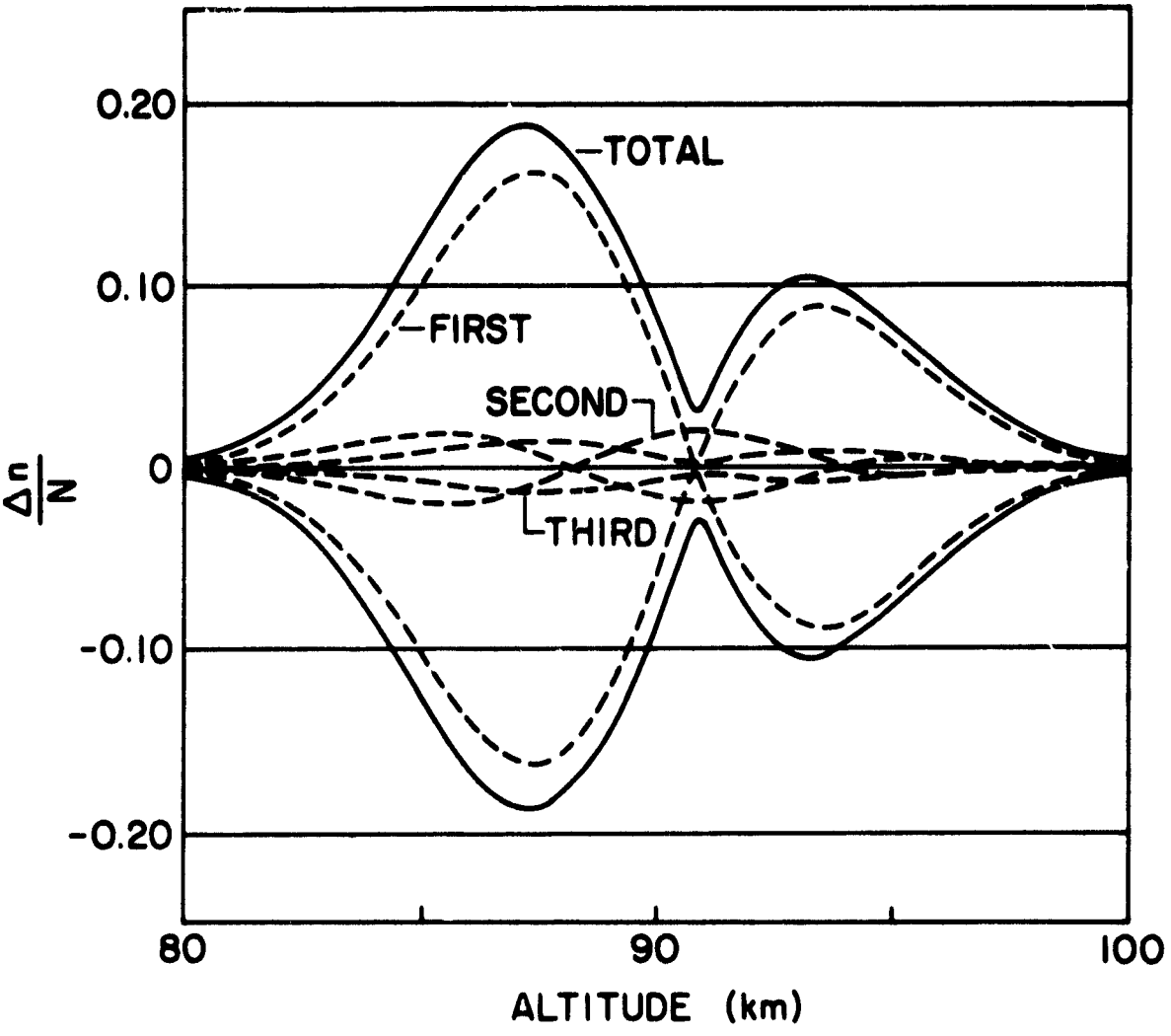

Figure 6.4 Predicted envelope of normalized density perturbations due to first three terms of perturbation series solution. 5% peak-to-peak background density variations are assumed. Gaussian layer described by $n(z) = N \exp[-(z-90)^2/18]$ is assumed.

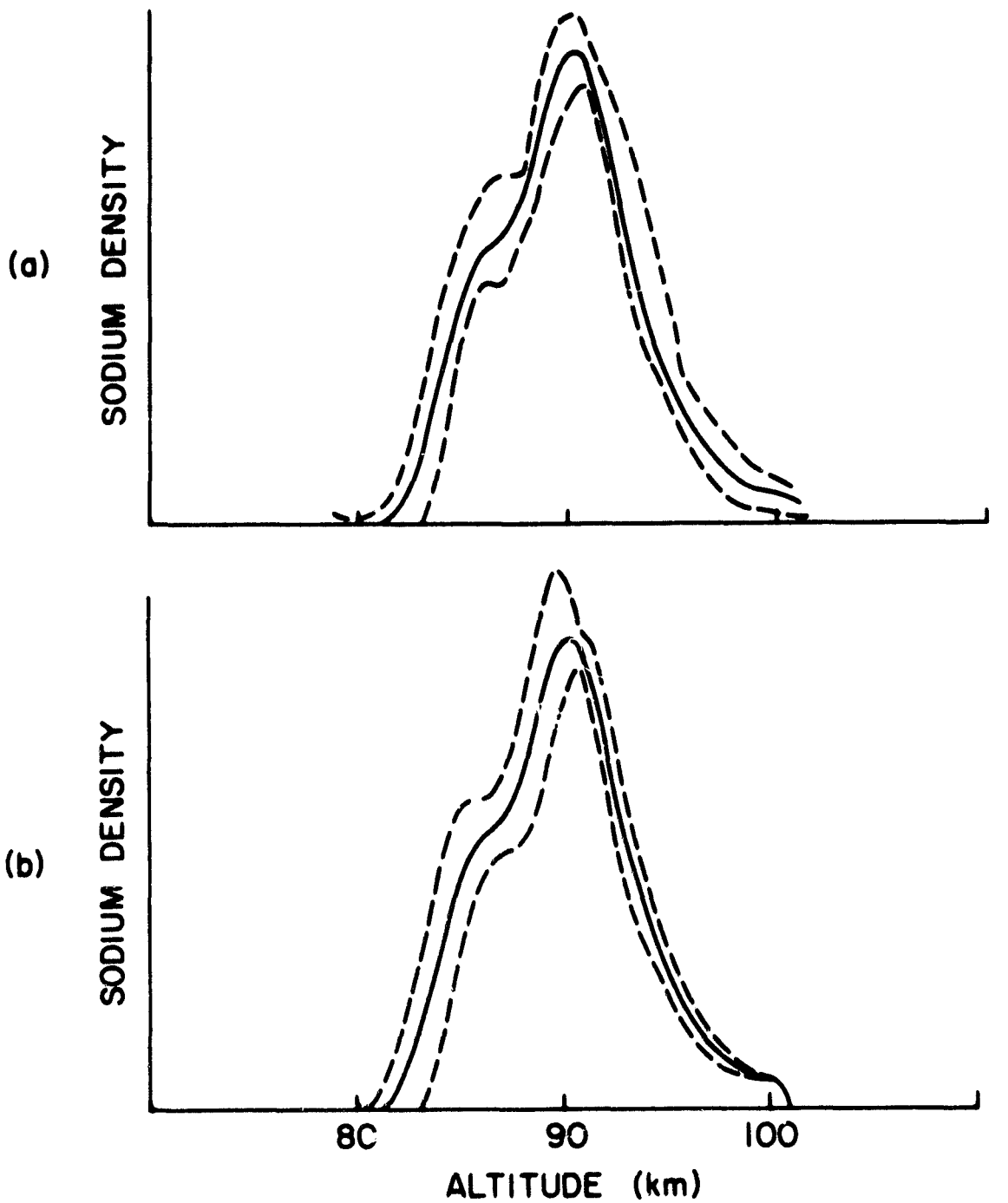

Figure 6.5 (a) Experimentally observed envelope of density variations on October 28-29, 1979. Solid line is average density profile. (b) Predicted density variations due to first- and second-order terms. Solid line is the assumed steady-state density profile.

these mirrors made possible a linewidth measurement, but with a value of $\Delta\nu_{min}$ of 330 MHz, the convolution of the interferometer frequency transmission function and the laser linewidth cannot be neglected; it could have been neglected had the high finesse of the spherical mirrors been available. Knowing the value of $\Delta\nu_{min}$, the laser linewidth can be calculated from the measured linewidth. Using this knowledge a linewidth of 900 MHz was measured at an energy of 50 mJ/pulse for Configuration A and a linewidth of 400 MHz (0.005Å) at an energy of 20 mJ/pulse for Configuration B.

From the measured values of the laser linewidth it is concluded that Configuration A met all of the required specifications but that Configuration B did not. To be sure that the measured value of the laser linewidth was accurate, considering the difficulties encountered with the interferometer, the linewidth measurement was repeated with a Spectra-Physics Model 450-03 scanning interferometer, which is now available. The Spectra-Physics interferometer is a completely sealed unit. Mirrors were aligned at the factory and a photodetector is included. With a finesse of 200 and an FSR of 2 GHz, a bandwidth of 10 MHz results; this is small enough to neglect the convolution effect of the laser linewidth with the interferometer bandpass. The repeated linewidth measurement with the Spectra-Physics interferometer again resulted in a bandwidth of 400 MHz (0.005 Å) for Configuration B at the specified energy of 20 mJ/pulse.

At this time further work is being done by the laser manufacturer, Candela Corp., in an attempt to make the laser conform to the specifications of Configuration B.

6.4 *LSI-11 Microcomputer*

The University of Illinois sodium lidar system presently uses a Z-80 microcomputer to handle its receiver operations and data collection. Soon, an LSI-11 microcomputer will replace the Z-80 for several reasons which are outlined below.

A pulsed dye laser (manufactured by Candela Corporation; see Table 6.1 for laser parameters) is tuned to the D_2 sodium resonance line at a wavelength of 589 nm. Refer to the block diagram of Figure 6.6. This is done by directing a small portion of the laser output to a sodium vapor cell which serves as a wavelength monitor. The sodium vapor will fluoresce when a properly tuned laser beam passes through the cell. When the lidar system is properly aligned, the receiving telescope collects a fraction of the laser energy which has been backscattered from the sodium layer. The telescope filters the collected light to minimize background noise and then focuses the filtered signal onto the photocathode of the photomultiplier tube (PMT). The PMT is thermoelectrically cooled to -20°C in order to reduce dark noise. The discriminator generates logic-level pulses whenever a photon is detected by the PMT. The discriminator is connected to the photon-counter processor which contains a high-speed counter and semiconductor memory.

The microcomputer interfaces with the lidar receiving system directly through the photon-counter processor. After the laser has fired, the computer

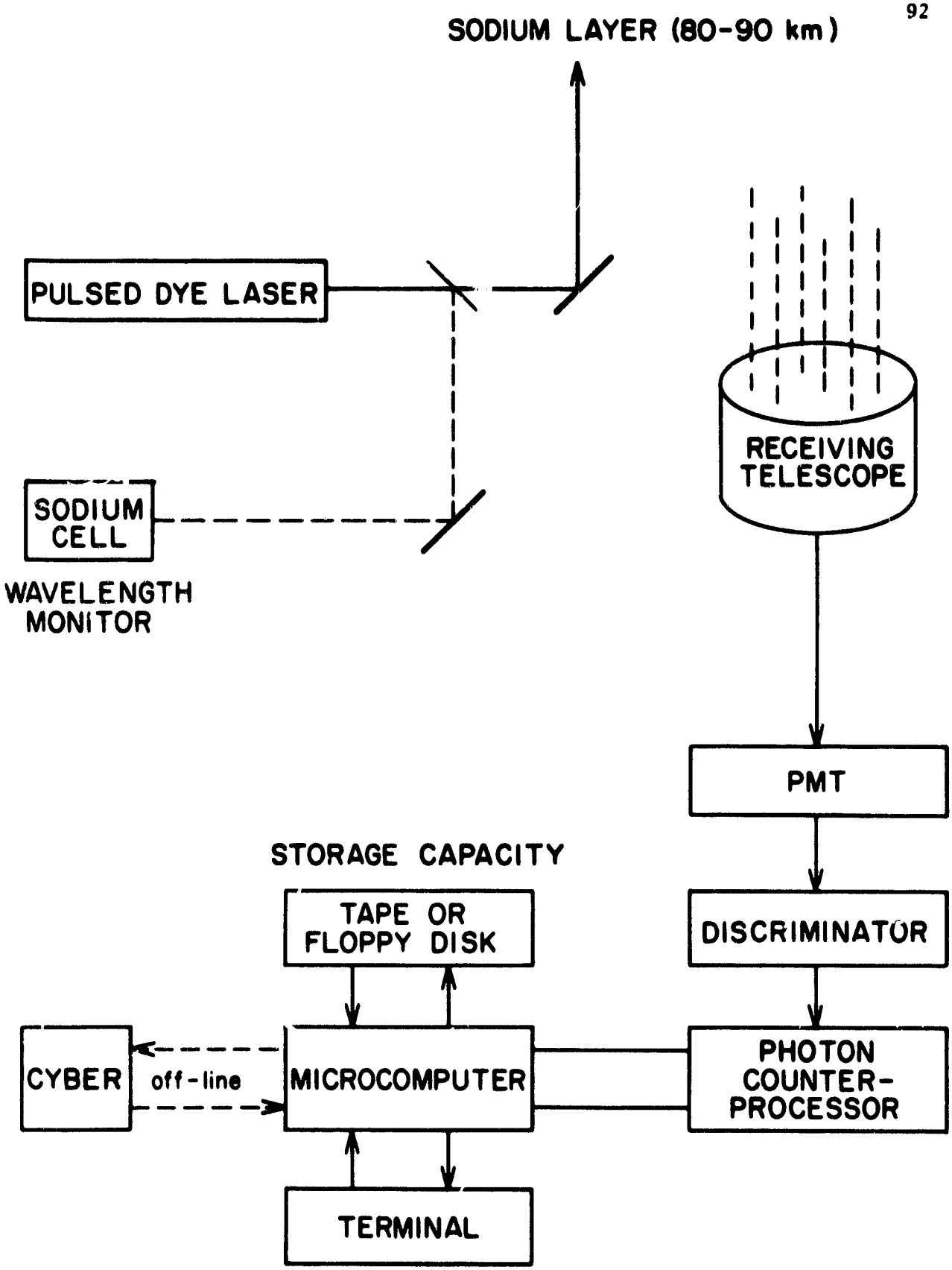

Figure 6.6 Block diagram of Urbana sodium lidar system.

instructs the processor to sample the photon-counter periodically and store samples in a semiconductor memory. 256 samples are obtained for each laser shot. The sampling interval can be varied from 1 to 256 μs. The one μsec sampling interval corresponds to a 150-m range resolution. When all 256 samples have been collected, the data are transferred from the processor memory to the computer. The computer subtracts successive samples to obtain the number of photons counted within each sampling interval or range bin. The photon counter continually increments and is reset only when it overflows. The photocounts are accumulated for each range bin until enough photons have been collected to construct a sodium profile. Typically 50 to 200 laser shots are required to obtain a profile. The raw data profiles are processed off-line on a CYBER-175 computer to obtain profiles of the sodium density versus altitude and time.

Presently a Z-80 performs the tasks of the microcomputer described above in addition to more minor tasks such as: (1) setting time duration between laser shots (typically 2 to 3 sec.), (2) aiding laser and receiver beam alignment, and (3) storing raw sodium profiles on cassette tape.

The LSI-11 microcomputer was chosen to replace the Z-80 because of the much faster processor and larger memory capacity. The faster processor should permit collection of lidar data at the maximum repetition rate of the new Candela laser (which is 10 Hz or once every 100 msec). The Z-80 will permit us to collect data at only a 2 Hz rate or slower. The faster processor coupled with a larger memory (20K vs. the Z-80's 8K) will also allow some basic on-line signal processing, thus permitting real-time observation of the sodium layer profile. Also, the LSI-11 will use a dual floppy disk-drive system to load programs and store raw profiles. The floppy disks provide a much faster means of transferring data to the CYBER 175 computer. Additional LSI-11 tasks will include monitoring the laser parameters of wavelength, line-width, and energy per pulse as well as controlling the laser tuning and firing.

The complete LSI-11 package is centered around the DEC LSI-11/2 processor and housed in an MDB Systems backplane operating unit; the system also includes two DSD 210 floppy disk-drive units, 20K words of memory and two peripherals, one DEC DLV11-J, 4-port asynchronous serial line unit and one DEC DRV11 parallel line unit.

6.5 *Receiving System Improvements*

A thermoelectrically cooled housing has been acquired for cooling the receiver photomultiplier tube. This unit, a Products For Research model TE-206 TS-RF housing, consists of an air heat exchanged housing, associated power supply, and a double pane pyrex window. An integral part of this window is a 1.5-inch focal length lens which focuses collimated light from the receiver optics onto the PMT photocathode. This unit replaces a unit which required liquid nitrogen vapors for cooling, thus alleviating the need for an reservior of liquid nitrogen. Both housings accommodate the RCA C31034A photomultiplier tube.

6.6 *Wavelength Measurement*

The feasibility of utilizing a Fizeau wavemeter to accurately monitor the wavelength of the Urbana LIDAR transmitter output beam was investigated by D. J. Burlet. This instrument is based on a Fizeau or "optical wedge" interferometer, the fringe pattern of which is digitized and stored in a small computer. This information is then processed to determine the wavelength of the interfering light.

The Fizeau wavemeter divides the collimated input beam into two overlapping beams of equal intensity, propagating not quite parallel to each other. The resulting uniformly space Fizeau fringe pattern is then sampled periodically by an array of photodiodes which digitizes the pattern and sends it into the computer memory for processing.

Processing consists of the following; the computer determines the spatial period of the pattern, and the location of a fringe intensity minimum. The interferometer wedge angle which is a known constant then allows the spatial pattern to be converted into a first approximation of the wavelength. The uncertainty here must be less than the free spectral range of the interferometer.

The computer then determines the interferometer path difference at the previously determined fringe minimum, utilizing the wedge angle and wedge spacing at a known reference position. The path difference at a fringe minimum contains an integer number of wavelengths. The computer, therefore, calculates the ratio of the path difference to the approximate wavelength determined above, which gives the interferometer order number plus a remainder. The remainder is then used to calculate the ratio of the remainder to the order number, this then being applied to the approximate wavelength, yielding a new estimate of the wavelength. This procedure is repeated until the solution converges to a "best value" of the wavelength limited only by the resolution of the measurement of the path difference at fringe minimum.

The study concluded the wavemeter is a feasible method of monitoring the output provided an enclosed and evacuated chamber for the interferometer can be easily constructed to eliminate dispersion and scattering of the interfering beams (see Figure 6.7).

REFERENCES

Gardner, C. S. and J. D. Shelton [1981], High resolution lidar measurements of the spatial and temporal variations of the mesospheric sodium layer *Optics Lett.*, *6*, 174-176.

Mihavics, M. A. [1979], Temporal filtering of lidar photocount data, M.S. thesis, Univ. of Ill., Urbana-Champaign.

Rowlett, J. R., C. S. Gardner, E. S. Richter and C. F. Sechrist, Jr. [1978], Lidar observations of wave-like structure in the atmospheric sodium layer, *Geophys. Res. Lett.*, *5*, 683-686.

Rowlett, J. R. and C. S. Gardner [1979], Signal processing of sodium lidar photocount data, *Radio Res. Lab. Rep. No. 604*, Univ. of Ill., Urbana-Champaign.

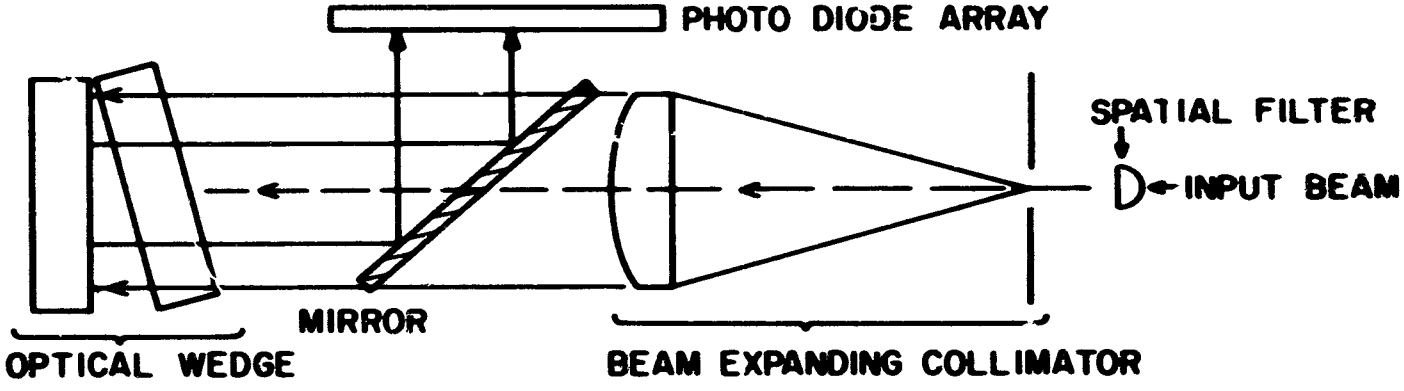

Figure 6.7 Fizeau interferometer.

PAPERS PUBLISHED AND PRESENTED AT MEETINGS
DURING THE PERIOD OCTOBER 1, 1980 - MARCH 31, 1981
The source of support is indicated in brackets

PAPERS PUBLISHED

Bowhill, S. A., Synoptic studies of the middle atmosphere using balloons, in *Advances in Space Research, Scientific Ballooning - II, 1*, No. 11, 1981, edited by W. Riedler and M. Friedrich, Pergamon

Dolas, P. M., and R. G. Roper, Prevailing wind in the meteor zone (80-100 km) over Atlanta and its association with midwinter stratospheric warming, *J. Atmos. Sci., 38*, 182-188, 1981 [NSF ATM 78-15224, in part].

Røyrvik, O., and K. L. Miller, Nonthermal scattering of radio waves near 150 km above Jicamarca, Peru, *J. Geophys. Res., 86*, 180-188, 1981 [NSF ATM 78-15224].

Shelton, J. D., C. S. Gardner, and C. F. Sechrist, Jr., Density response of the mesospheric sodium layer to gravity wave perturbations, *Geophys. Res. Lett., 7*, 1069-1072, 1980 [NSF ATM 78-12308 and ATM 79-20726, NASA NGR 14-005-181].

Smith, L. G., and K. L. Miller, Midlatitude sporadic-E layers, *AGARD Conf. Proc. No. 295, The Physical Basis of the Ionosphere in the Solar-Terrestrial System*, 25-1 -- 25-6, 1981 (available NTIS, 5285 Port Royal Road, Springfield, VA 22161), [NASA NGR 14-005-181].

Smith, L. G., and H. D. Voss, Energetic particle precipitation at middle and low latitudes, *AGARD Conf. Proc. No. 295, The Physical Basis of the Ionosphere in the Solar-Terrestrial System*, 21-1 -- 21-6, 1981 (available NTIS 5285 Port Royal Road, Springfield, VA 22161) [NASA NGR 14-005-181].

PAPERS ACCEPTED

Gardner, C. S., and J. D. Shelton, Spatial and temporal filtering technique for processing lidar photocount data, *Optics Lett.*

PAPERS PRESENTED AT MEETINGS

AGARD/NATO
Naples, Italy, October 1980

Smith, L. G., and K. L. Miller, Midlatitude sporadic-E layers [NASA NGR 14-005-181].

Smith, L. G., and H. D. Voss, Energetic precipitation at middle and low latitudes [NASA NGR 14-005-181].

AGU
San Francisco, CA, December 1980

Røyrvik, O., Sporadic-E study at Arecibo [NSF ATM 78-15224].

THIRD CONFERENCE ON METEOROLOGY OF THE UPPER ATMOSPHERE
San Diego, CA, January 1981

Jones, G. A., S. K. Avery, and C. F. Sechrist, Jr., Planetary wave transport of nitric oxide [NSF ATM 79-09982 and NASA NGR 5213].

AERONOMY LABORATORY SEMINARS

During the regular Fall and Spring semesters, a seminar series in aeronomy is offered as graduate course EE 490. The following seminars were conducted during the period covered by this report under the supervision of Prof. C. F. Sechrist, Jr. and Prof. S. K. Avery.

October 7	Mr. Carl Stehle Graduate Assistant Department of Computer Science University of Illinois	A Neutral Model of the Thermosphere in Magnetic Coordinates
October 14	Dr. Jane Fox Dept. of Electrical Engineering Aeronomy Laboratory University of Illinois	A Stratospheric Chemical Instability
October 17*	Dr. J. Bufton & Mr. J. Abshire NASA-Goddard Space Flight Center Greenbelt, MD	Laser Radar and Ranging Projects at NASA-Goddard Space Flight Center
October 21	Dr. Wayne M. Wendland Illinois State Water Survey University of Illinois	Advection Patterns Inferred from Mt. St. Helens' Volcanic Plume
November 4	Mr. Gary A. Jones Dept. of Electrical Engineering Aeronomy Laboratory University of Illinois	Planetary Waves and Nitric Oxide Transport
November 11	Dr. P. M. Dolas Dept. of Electrical Engineering Aeronomy Laboratory University of Illinois	Gravity Waves in the Equatorial Mesosphere
November 25	Prof. S. K. Avery Dept. of Electrical Engineering Aeronomy Laboratory University of Illinois	Correlative Measurements Using the Urbana Lidar and Meteor Radar
December 2	Prof. S. A. Bowhill Dept. of Electrical Engineering Aeronomy Laboratory University of Illinois	Radar Signal Processing by Microcomputer: I. The FORTH Language
December 9	Prof. S. A. Bowhill Dept. of Electrical Engineering Aeronomy Laboratory University of Illinois	Radar Signal Processing by Microcomputer: II. Implementation of a Coherent Scatter System

January 27*	Dr. H. Furumoto Candela Corporation Natick, MA	Laser Applications: The Early Days of Uranium Isotope Separation
February 3**	Albert G. Brejcha Jet Propulsion Laboratory Pasadena, CA	The Voyager Program
February 10	Dr. Ola Røyrvik Dept. of Electrical Engineering Aeronomy Laboratory University of Illinois	Mesospheric Scatter from the Urbana Radar
February 17	Prof. S. A. Bowhill Dept. of Electrical Engineering Aeronomy Laboratory University of Illinois	Geophysical Data Management in the 1980s
March 10	Prof. Gernot Metze Dept. of Electrical Engineering Aeronomy Laboratory University of Illinois	Some Current Problems in Fault Tolerant Computing
March 24	Dr. L. G. Smith Dept. of Electrical Engineering Aeronomy Laboratory University of Illinois	The Phase-Locked Loop and Some Applications

* Special Aeronomy Seminar

** Joint Electromagnetic and Aeronomy Seminar

CUMULATIVE LIST OF UNIVERSITY OF ILLINOIS AERONOMY REPORTS

Aeronomy Report No. 1 Bowhill, S. A. (Ed.) (December 1963), Direct aeronomic measurements in the lower ionosphere--an informal record.

Aeronomy Report No. 2 Balmain, K. G. (July 1964), The impedance of a short dipole antenna in a magnetoplasma.

Aeronomy Report No. 3 Hodges, R. R., Jr. (November 1964), Gyro-interaction rocket experiments in the lower ionosphere.

Aeronomy Report No. 4 Rzeszewski, T. S., and S. A. Bowhill (January 1965), The design and operation of a pulse compression system.

Aeronomy Report No. 5 Geisler, J. E., and S. A. Bowhill (January 1965), An investigation of ionosphere-protonosphere coupling.

Aeronomy Report No. 6 Rao, G. L. N. (June 1965), Horizontal drifts and anisotropy of irregularities in the lower ionosphere--a review.

Aeronomy Report No. 7 Appel, R. L., and S. A. Bowhill (September 1965), An automatic recording system for the determination of ionospheric absorption

Aeronomy Report No. 8 Kostelnicek, R. J. (September 1965), The admittance and resonance probe characteristics of a spherical plasma probe.

Aeronomy Report No. 9 Rao, G. L. N. (June 1966), Horizontal drifts and anisotropy of irregularities in the upper ionosphere--a review.

Aeronomy Report No. 10 Sechrist, C. F., Jr. and J. S. Shirke (Eds.) (December 1965), Second conference on direct aeronomic measurements in the lower ionosphere--an informal conference record.

Aeronomy Report No. 11 Balmain, K. G. (May 1966), Plasma probe studies.

Aeronomy Report No. 12 Gliddon, J. E. C. (June 1966), Theoretical investigations of the structure of the protonosphere and upper F-region.

Aeronomy Report No. 13 Henry, G. W., Jr. (August 1966), Instrumentation and preliminary results from shipboard measurements of vertical incidence ionospheric absorption.

Aeronomy Report No. 14 Saleh, J. E., and S. A. Bowhill (August 1966), Collision frequencies and electron temperatures in the lower ionosphere.

Aeronomy Report No. 15 Paramasivaiah, P., and S. A. Bowhill (August 1966), E-region ionization and thermal structure.

Aeronomy Report No. 16 Wippermann, D. R. (March 1967), The application of pulse compression techniques to ionosphere sounding.

Aeronomy Report No. 17 Evans, J. V. (April 1967), Design considerations for a Thomson scatter radar.

Aeronomy Report No. 18 Subcommittee on Aeronomy, Committee on Institutional Cooperation (May 1967), Program study for a Thomson scatter radar.

Aeronomy Report No. 19 Evans, J. V. (Ed.) (May 1967), Thomson scatter studies of the ionosphere--an informal conference record.

Aeronomy Report No. 20 Rao, M. M. (July 1967), Studies of the equatorial ionosphere using rockets.

Aeronomy Report No. 21 Cicerone, R. J., and S. A. Bowhill (June 1967), Positive ion collection by a spherical probe in a collision-dominated plasma.

Aeronomy Report No. 22 Shirke, J. S. (September 1967), Studies of ionospheric absorption measurements.

Aeronomy Report No. 23 Evans, J. V. (October 1967), Antenna design for a Thomson scatter radar.

Aeronomy Report No. 24 Evans, J. V., and S. A. Bowhill (January 1968), Plan for the implementation of a Thomson scatter radar.

Aeronomy Report No. 25 Evans, J. V. (June 1968), Antenna feasibility studies for a Thomson scatter radar.

Aeronomy Report No. 26 Fish, R. M., and S. A. Bowhill (June 1968), Instrumentation for the measurements of airglow.

Aeronomy Report No. 27 Guha, D. (August 1968), Studies of lower ionosphere drifts by the three-receiver technique.

Aeronomy Report No. 28 Mantas, G. P., J. V. Evans, and J. V. Ceferin (August 1968), F-region theory; Part 1, The thermal structure of the ionosphere; Part 2, The shape of the daytime ionospheric F2 layer.

Aeronomy Report No. 29 Pirnat, C., and S. A. Bowhill (December 1968), Electron densities in the lower ionosphere deduced from partial reflection measurements.

Aeronomy Report No. 30 Condon, R. C., K. Seino, and E. A. Mechtly (December 1968), Part 1, Design of polarization adjustment instrumentation for a rocket propagation experiment, Part 2, Analysis of a rocket experiment to measure ionospheric electron density.

Aeronomy Report No. 31 Shere, K. D., and S. A. Bowhill (January 1969), Gravity waves in a viscous atmosphere.

Aeronomy Report No. 32 Sechrist, C. F., Jr. (Ed.) (April 1969), Meteorological and chemical factors in D-region aeronomy.

Aeronomy Report No. 33 Viertel, W. A., and C. F. Sechrist, Jr. (June 1969), Full-wave calculation of reflection coefficients from D-region electron density profiles.

Aeronomy Report No. 34 Forbes, J. M. (January 1970), Production and loss of $O(^1D)$ in the nighttime F region.

Aeronomy Report No. 35 Slekys, A. G., and E. A. Mechtly (March 1970), Aeronomy Laboratory system for digital processing of rocket telemetry tapes.

Aeronomy Report No. 36 Reynolds, D. A., and C. F. Sechrist, Jr. (May 1970), Measurement of average electron density between 75 and 80 kilometers.

Aeronomy Report No. 37 Mechtly, E. A., P. E. Monro, N. Golshan, and R. S. Sastry (July 1970), FORTRAN programs for calculating lower ionosphere electron densities and collision frequencies from rocket data.

Aeronomy Report No. 38 Radicella, S. M., and D. W. Stowe (July 1970), D-region ion chemistry.

Aeronomy Report No. 39 Cicerone, R. J., and S. A. Bowhill (September 1970), Monte Carlo and Thomson-scatter plasma-line studies of ionospheric-photoelectrons.

Aeronomy Report No. 40 Forbes, J. M., and M. A. Geller (October 1970), Lunar semidiurnal component of the OI (5577Å) airglow.

Aeronomy Report No. 41 Turco, R. P., and C. F. Sechrist, Jr. (December 1970), An investigation of the ionospheric D region at sunrise.

Aeronomy Report No. 42 Birley, M. H., and C. F. Sechrist, Jr. (June 1971), Partial-reflection data collection and processing using a small computer.

Aeronomy Report No. 43 Horton, B. E., and S. A. Bowhill (August 1971), Computer simulation of supersonic rarefied gas flow in the transition region, about a spherical probe; a Monte Carlo approach with application to rocket-borne ion probe experiments.

Aeronomy Report No. 44 Carpenter, L. A., and S. A. Bowhill (September 1971), Investigation of the physics of dynamical processes in the topside F region.

Aeronomy Report No. 45 Lodato, R. F., and E. A. Mechtly (September 1971), Rocket measurements of electron collision frequency.

Aeronomy Report No. 46 Wuebbles, D. J., T. Shimazaki, and C. F. Sechrist, Jr. (January 1972), A mathematical model for the radon density distribution in the 1-20 km region.

Aeronomy Report No. 47 Wiersma, D. J., and C. F. Sechrist, Jr. (March 1972), Differential phase measurements of D-region partial reflections.

Aeronomy Report No. 48 Sechrist, C. F., Jr. and M. A. Geller (Eds.) (June 1972), COSPAR symposium on D and E-region ion chemistry--An informal symposium record.

Aeronomy Report No. 49 Damico, D. F. and S. A. Bowhill (May 1972), Monte Carlo studies of ion collection in a supersonic flowing plasma.

Aeronomy Report No. 50 Guha, D. and M. A. Geller (June 1972), Computer simulation of the three-receiver drift experiment.

Aeronomy Report No. 51 Oliver, W. L. and S. A. Bowhill (February 1973), Investigation of the ionospheric response to the solar eclipse of 7 March 1970 by the Thomson scatter radar technique at the Millstone Hill ionospheric observatory.

Aeronomy Report No. 52 Lee, W. and M. A. Geller (March 1973), Preliminary design study of a high resolution meteor radar.

Aeronomy Report No. 53 Slightam, R. J. and S. A. Bowhill (May 1973), Improved calibration of incoherent-scatter electron densities from ionograms.

Aeronomy Report No. 54 Mantas, G. P. (September 1973), Electron collision processes in the ionosphere.

Aeronomy Report No. 55 Bean, T. A. and S. A. Bowhill (October 1973), Analysis of partial-reflection data from the solar eclipse of July 10, 1972.

Aeronomy Report No. 56 Denny, B. W. and S. A. Bowhill (October 1973), Partial-reflection studies of D-region winter variability.

Aeronomy Report No. 57 Countryman, I. D. and S. A. Bowhill (October 1973), Investigation of incoherent-scatter spectral asymmetries in the topside F region.

Aeronomy Report No. 58 Gray, K. G. and S. A. Bowhill (January 1974), The transient response of stratified cold plasma electromagnetic waves by analytical and numerical methods.

Aeronomy Report No. 59 Backof, C. A. and S. A. Bowhill (April 1974), Collection and processing of data from a phase-coherent meteor radar.

Aeronomy Report No. 60 Harper, R. M. and S. A. Bowhill (July 1974), Digital ionosonde studies of F-region waves.

Aeronomy Report No. 61 Golshan, N. and C. F. Sechrist, Jr. (September 1974), An investigation of odd nitrogen in the ionospheric E region.

Aeronomy Report No. 62 Voss, H. D. and L. G. Smith (October 1974), Design and calibration of a rocket-borne electron spectrometer for investigation of particle ionization in the nighttime midlatitude E region.

Aeronomy Report No. 63 daSilva, L. C. and S. A. Bowhill (October 1974), An evaluation of the partial-reflection technique and results from the winter 1971-1972 D region.

Aeronomy Report No. 64 Ginther, J. C. and L. G. Smith (December 1974), Studies of the differential absorption experiment.

Aeronomy Report No. 65 Harrington, T. A. and M. A. Geller (March 1975), Performance of the University of Illinois meteor-radar system -- A preliminary report.

Aeronomy Report No. 66 Evans, J. C. and L. G. Smith (April 1975), Rocket measurements of ozone and molecular oxygen by absorption spectroscopy.

Aeronomy Report No. 67 Ratnasiri, P. A. J. and C. F. Sechrist, Jr. (April 1975), An investigation of the solar zenith angle variation of D-region ionization.

Aeronomy Report No. 68 Rastogi, P. K. and S. A. Bowhill (April 1975), Remote sensing of the mesosphere using the Jicamarca incoherent-scatter radar.

Aeronomy Report No. 69 Owens, W. R. and S. A. Bowhill (May 1975), Measurement of electron densities below 70 km by partial reflections.

Aeronomy Report No. 70 Schoeberl, M. R. and M. A. Geller (January 1976), The propagation of planetary-scale waves into the upper atmosphere.

Aeronomy Report No. 71 Allman, M. E. and S. A. Bowhill (February 1976), Feed system design for the Urbana incoherent-scatter radar antenna.

Aeronomy Report No. 72 Ryan, P. D. and S. A. Bowhill (April 1976), Error analysis of radial wind velocity measurements using the University of Illinois meteor radar.

Aeronomy Report No. 73 Fillinger, R. W., Jr., E. A. Mechtly and E. K. Walton (July 1976), Analysis of sounding rocket data from Punta Chilca, Peru.

Aeronomy Report No. 74 Hess, G. C. and M. A. Geller (October 1976), The Urbana meteor-radar system: Design, development, and first observations.

Aeronomy Report No. 75 Hill, R. J. and S. A. Bowhill (November 1976), Small-scale fluctuations in D-region ionization due to hydrodynamic turbulence.

Aeronomy Report No. 76 Miller, K. L. and L. G. Smith (December 1976), Midlatitude sporadic-E layers.

Aeronomy Report No. 77 Paarmann, L. D. and L. G. Smith (May 1977), A rocket-borne airglow photometer.

Aeronomy Report No. 78 Voss, H. D. and L. G. Smith (November 1977), Energetic particles and ionization in the nighttime middle and low latitude ionosphere.

Aeronomy Report No. 79 Richter, E. S. and C. F. Sechrist, Jr. (May 1978), Theoretical and experimental studies of the atmospheric sodium layer.

Aeronomy Report No. 80 Klaus, D. E. and L. G. Smith (June 1978), Rocket observations of electron-density irregularities in the equatorial ionosphere.

Aeronomy Report No. 81 Weiland, R. M. and S. A. Bowhill (September 1978), D-region differential-phase measurements and ionization variability studies.

Aeronomy Report No. 82 Pozzi, M. A., L. G. Smith, and H. D. Voss (February 1979), A rocket-borne electrostatic analyzer for measurement of energetic particle flux.

Aeronomy Report No. 83 Leung, W., L. G. Smith, and H. D. Voss (March 1979), A rocket-borne pulse-height analyzer for energetic particle measurements.

Aeronomy Report No. 84 Davis, L. L., L. G. Smith, and H. D. Voss (April 1979), A rocket-borne data-manipulation experiment using a microprocessor.

Aeronomy Report No. 85 Gilchrist, B. E. and L. G. Smith (April 1979), Rocket measurement of electron density in the nighttime ionosphere.

Aeronomy Report No. 86 Munninghoff, D. E. (April 1979), Ion and electron temperatures in the topside ionosphere.

Aeronomy Report No. 87 Enge, P. K., and S. K. Avery (May 1979), Day-to-day variations of atmospheric tides as observed by meteor radar.

Aeronomy Report No. 88 Teitelbaum, K., and C. F. Sechrist, Jr. (June 1979), A microcomputer control system for the Urbana sodium lidar.

Aeronomy Report No. 89 Countryman, I. D., and S. A. Bowhill (October 1979), Wind and wave observations in the mesosphere using coherent-scatter radar.

Aeronomy Report No. 90 Gibbs, K. P., and S. A. Bowhill (December 1979), The Urbana coherent-scatter radar: Synthesis and first results.

Aeronomy Report No. 91 Fries, K. L., L. G. Smith, and H. D. Voss (December 1979), A rocket-borne energy spectrometer using multiple solid-state detectors for particle identification.

Aeronomy Report No. 92 Zimmerman, R. K., Jr., and L. G. Smith (April 1980), Rocket measurements of electron temperature in the E region.

Aeronomy Report No. 93 Bliss, H. M., and L. G. Smith (May 1980), Rocket observations of solar radiation during the eclipse of 26 February 1979.

Aeronomy Report No. 94 Cerny, T., and C. F. Sechrist, Jr. (August 1980), Calibration of the Urbana lidar system.